



“New mechanisms and concepts for exploiting electroactive
Polymers for Wave Energy Conversion”

FP7-ENERGY-2012-1-2STAGE
FUTURE EMERGING TECHNOLOGIES

Grant Agreement N. 309139

Wave-tank tests of first generation PolyWEC units				
Deliverable No.		4.1		
WP No.	4	WP Title	Wave-tank testing	
Task	T4.2	Task Title	Tank testing of PolyWECS in operational conditions	
Nature (R: Report, P: Prototype, O: Other)		R		
Dissemination level (PU, PP, RE, CO)		PU		
Lead beneficiary:		UEDIN		
Authors List:		Authors and contributors David Forehand (UEDIN) Jean-Baptiste Richon (UEDIN) Marco Fontana (SSSA) Giacomo Moretti (SSSA) Gastone Pierro Papini Rosati (SSSA) Rocco Vertechy (UNIBO)		
Status (F: final; D: draft; RD: revised draft):		F		
File Name:		D41_Tank_Tests_1st_Gen.pdf		
Due Delivery Date:		M36		
Actual Delivery Date:		M40		

Version History table

Version no.	Dates and comments
1	June 2015 Partial draft with contribution from 1 st set of tests
2	Nov 2015 First draft reviewed and second partial draft including 2 nd set of tests
3	Jan 2016 Full draft
4	March 2016 Final document
5	

INDEX

INDEX.....	3
1 Executive summary	4
1 INTRODUCTION	6
2 PolyWEC prototypes scaling	9
2.1 Linear/Rotary DEGs coupled with a moving primary interface (floater-driven)	9
2.1.1 WEC displacement perpendicular to the DEG electrodes	12
2.1.2 WEC displacement coplanar with the DEG electrodes	13
2.2 Inflated DEGs (or direct-contact)	15
2.2.1 DE membrane scaling	16
2.2.2 Air volume scaling	17
2.3 Concluding remarks.....	18
3 Dry-run tests on circular diaphragm deg.....	19
3.1 Setup	19
3.2 CD-DEG electro-mechanical model	20
3.3 Material characterization	21
3.4 Generation tests.....	24
3.5 Hardware-in-Loop tests	28
4 Wave-tank TESTING: FACILITIES AT EDINBURGH UNIVERSITY	32
4.1 Wave-flume	32
4.2 FloWave.....	32
5 FIXED STRUCTURE OWC – PRELIMINARY DESIGN	34
5.1 Experimental setup	34
5.2 Procedure and Data Processing	35
5.3 Results.....	39
5.4 Model validation	43
5.4.1 CD-DEG electro-hyperelastic model validation	43
6 FIXED STRUCTURE OWC – ADVANCED DESIGN	45
6.1 Experimental setup	45
6.2 Procedure and Data Processing	47
6.3 Results.....	49
6.4 Model validation	53
6.4.1 CD-DEG electro-hyperelastic model validation	53
6.4.2 Poly-OWC elasto-hydrodynamic model validation.....	54
7 FLOATING MOORED OWC	59
7.1 Experimental setup	59
7.2 Procedure and Data Processing	60
7.2.1 Identification of the CD-DEG tip height.....	60
7.2.2 Energy harvested estimate	62
7.3 Results.....	63
7.3.1 Regular waves tests	63
7.3.2 Irregular waves tests	65
7.4 Model validation	66
7.4.1 CD-DEG electro-hyperelastic model validation	66
7.4.2 Poly-OWC elasto-hydrodynamic model validation.....	68
8 CONCLUSIONS AND FUTURE WORKS	70
9 References	72

1 EXECUTIVE SUMMARY

This deliverable describes the methodologies and the obtained results of the first sets of dry-run and wave-tank experimental campaigns carried out within the PolyWEC project. Specifically, beside a series of dry-run tests performed to validate theoretical models and to study possible control strategies, three sets of tank-test experiments have been carried out considering 1st Generation PolyWEC systems, i.e. Wave Energy Converters (WEC) based on Dielectric Generators (DEGs) in which the contact between DEG and water waves is mediated by a collector or mechanism.

Among the different devices that were initially conceived, the focus was set on a specific class of WEC named Poly-OWC, i.e., Oscillating Water Column (OWC) with Dielectric Elastomer (DE) inflating diaphragm as Power Take-Off (PTO). This architecture has been considered the most promising among 1st generation devices.

Different implementations of Poly-OWC have been studied in the tank experiments:

- A first fixed-structure OWC with non-optimized collector hydrodynamics. This prototype was the first to be tested in an early stage of the project. The aim of these first experiments was to assess the response of the DE PTO and its control in a dynamic framework and in presence of waves excitation, so as to demonstrate that DEs can effectively harness wave energy. Attention was thus focused on the PTO and its control, whereas the device dynamic response was not optimized, i.e., the response of the device was not appropriately tuned with the frequency content of the incoming waves.
- Fixed-structure OWC with resonant collector. In a second test campaign, an optimized geometry for the bottom-fixed collector was designed, which included a water duct to increase the added mass of the system. Due to this larger added mass, a clear improvement in the performances was detected. An optimized architecture for the control electronic layout was also employed.
- Moored tubular OWC. This system is a small-scale model of a much more feasible solution, from the point of view of scalability, and consists of a floating type OWC device, which is moored to the sea bottom by means of tension legs. The collector is based on a design proposed by a Spanish company (Sendekia).

The first two models were tested in a Wave Flume available at the University of Edinburgh, while experiments on the floating Poly-OWC were executed in the FloWave facility in Edinburgh. All of the tested prototypes had a scale between 1:50 and 1:40. Models have been created through a scaling methodology based on the well recognized techniques in the Wave Energy sector and extended in order to include an appropriate method for the scaling of the DEG (a formal description of scaling rules is presented in the second section of this document).

In all the three test sessions, fully functional devices have been employed that are able to convert mechanical energy from incident waves into DC electrical energy stored in high voltage capacitors. Different control strategies have been tested in monochromatic and panchromatic seas demonstrating the possibility of controlling the system activation through very simple yet effective strategies.

Results of these experiments have been employed to validate and evaluate the accuracy of the theoretical models developed in WP1. Specifically, theoretical models showed a good matching especially for the second set of experiments (i.e. fixed OWC with resonant collector) where the experimental conditions were the most controlled.

Beside the validation of models, it was also possible to evaluate global performance indexes such as the amount of converted energy, average power and other figures of merit. In particular, a maximum power output of more than 0.9W (in the 1:40 scaled model) has been achieved for the second set of tests, with almost 20% of the incident wave power converted into electricity. A maximum power in the order of 0.15W (in a 1:50 scaled model) has been achieved the third set of tests, using a point absorber collector.

These results are definitely very promising considering that: (1) non-optimized acrylic elastomers materials have been employed for the DEG, since the combination of scaling rules and intrinsic stiffness, made it impossible to test materials that are more adequate for the real-scale devices, such as Natural Rubber, Synthetic Rubber and Silicone. These latter materials, that were tested in dry-run tests on a setup that was specifically developed for the project, showed greatly improved performances in terms of efficiency and energy conversion capacity which make them very promising for full-scale applications.

List of acronyms:

BEM: Boundary Element Method
C-DEG: Conical Dielectric Elastomer Generator;
CD-DEG: Circular Diaphragm Dielectric Elastomer Generator;
DE: Dielectric Elastomers;
DEG: Dielectric Elastomer Generator;
DoF: Degree of Freedom
HIL: Hardware-in-Loop;
HV: High Voltage;
I-DEG: Inflated Dielectric Elastomer Generator;
MWL: Mean Water Level;
OWC: Oscillating Water Column;
P-DEG: Planar Dielectric Elastomer Generator;
PS-DEG: Parallelogram-Shaped Dielectric Elastomer Generator;
PTO: Power Take Off;
S-DEG: Stacked Dielectric Elastomer Generator;
SS: Sea State;
WEC: Wave Energy Converter.

1 INTRODUCTION

In previous deliverables of the PolyWEC project [1-2], several implementations of Dielectric Elastomers (DEs) for wave energy conversion have been analysed from the theoretical point of view showing interesting performances. A broad variety of concepts of 1st Generation PolyWECs, i.e. systems that feature a mediated contact between the DE generator (DEG) and the water, have been described through hydro-electro-mechanical models. Their preliminary design and optimization has been presented and, for the most promising concepts, the calculation of theoretical power matrices has been performed [1], [2]. Moreover, preliminary techno-economic analyses have been carried out, based on theoretical predictions, which showed a very great potential for PolyWECs [3].

However, in order to have a validation/confirmation of theoretical predictions, an in depth experimental investigation of the proposed concepts is required. Indeed, experiments are essential to validate mathematical models, prove the practical operating principle of PolyWECs, test control strategies, identify practical and engineering issues involved in the operation of the devices.

For these reasons, within the Project a campaign of tank-tests has been initiated since quite an early stage. This deliverable provides an overview of all the experiments that have been conducted in the different phases of the project, by particular describing the adopted methodologies and setups as well as the attained results.

Specifically, DEG based PTO systems have been tested following two different approaches [4]: 1) dry-run tests on the PTO unit itself, which is tested in laboratory conditions, with the dynamics of the coupled WEC emulated by actuators and hardware-in-loop logics; 2) wet-run tests, in which the PTO is mounted on a functional prototype of WEC and tested in a wave-tank.

In the framework of the PolyWEC project, several dry-run tests have been performed on dedicated setups, results have been collected in a previous deliverable [5] and partially extended in this report.

As regards the tank tests, this is a commonly accepted practice in the development of new WEC concepts, for which wet tests are sequentially conducted on a series of prototypes with increasing scale. Such devices are first tested in tank conditions, and, in a second stage, they are brought to sea, first with a reduced scale with respect to the real prototype, and, lastly, in full-scale conditions [6], [7].

According to [7], a new WEC concept requires a preliminary analysis and numerical simulation phase, oriented to the construction of a small-scale prototype (e.g., 1:50) to be tested in a wave tank, in conditions of hydrodynamic scaling. These preliminary tests allow the validation and update of previously established numerical models, the computation of some highly uncertain physical parameters (e.g., drag coefficients, vortex induced vibration effects, etc.) and the identification of maximal wave-breaking loads for preliminary structural design (eventually including the mooring system). Medium-scale (e.g., 1:20 or 1:30) tank tests should be performed in order to further improve the design, test the control laws, assess the stability/survivability in extreme sea states and to have a better estimate of the real-scale device potential performance. Final scale-up steps may include sea-tests, monitoring and grid connection of a nearly-full-scale (e.g., 1:5) prototype at first, and of the full-scale device lastly. In most of the cases described in literature of WECs, small-scale prototypes are often tested without any real functional PTO and energy extraction by the PTO is simply emulated using passive elements such as brakes and dampers.

In this deliverable, we describe tank-tests on three different implementations of the Poly-OWC concept, equipped with fully-functional Circular Diaphragm DE Generators (CD-DEGs) as PTOs. According to previous indications [7], the tested prototypes have a scale in the range of 1:50 and 1:40. It is worth remarking that, since the aim of PolyWEC is assessing new PTO concepts, yet at this scale fully-functional (i.e., electrically activated) DEGs have been tested; that is, electricity has been produced in all of the considered sets of tests.

The Poly-OWC system has been selected among other 1st generation concepts for experimental tests because:

- it is one of the most promising architectures that features an extremely reduced number of moving parts (eventually, only the DE unit) and a simple and potentially cheap architecture;

- positive feedbacks on the techno-economic feasibility of this concept have already been obtained [3];
- its architecture can be adapted to different types of installations such as on-shore, along the shoreline and off-shore;
- it is the most promising in terms of full-scale industrial development since it enables an incremental approach that is envisaged as follows: (1) first up-scaled installations should be on-shore fixed structure OWC concepts that make it possible to further develop the large scale DEG technologies without facing typical drawbacks related to off-shore maintenance and electric energy transportation; (2) a further development envisages off-shore installations with large OWC collectors that are fixed to platforms or other off-shore constructions; (3) the final goal will be the development of off-shore bottom-moored arrays of OWCs, which are the most challenging to be realized.

Following the incremental approach described in the last point, experimental tests were first addressed to investigate the concept of on-shore fixed OWCs, then, in the last set of tests, a floating tubular OWC collector has been tested. Collected data were then post-processed and extensively employed to validate previously established mathematical models.

In all the three test sessions, fully functional devices have been employed that are able to convert mechanical energy from incident waves into DC electric energy stored in high voltage capacitors. Different control strategies have been tested in monochromatic and panchromatic seas demonstrating the possibility of controlling the system activation through very simple yet effective strategies.

Results of these experiments have been compared with theoretical models developed in WP1. Beside the validation of models, it was also possible to evaluate global performance indexes such as amount of converted energy, average power and other figures of merit.

The contents of this report are organized as follows. Sect. 2 presents a theoretical dissertation on the problem of scaling DE-PTOs in order to carry out consistently Froude-scaled tank-tests. Testing a WEC in conditions of hydrodynamic similarity is a requisite to reproduce the full-scale dynamics in the experiments. The well-known criterion of Froude scaling [6] is recognized to be the most suitable to scale floaters dynamics, and it establishes a series of practical rules to determine how the different physical variables must scale if the WEC size is scaled by a given factor. Unfortunately, the electro-mechanical response (namely, provided force/torque/pressure/power) of DEGs does not scale according to Froude's rules. Therefore, in order to properly set-up small-scale experiments on DE-based WECs, the different dimensions of a hypothetic full-scale DEG have to be scaled with different coefficients. These coefficients have been deduced for a wide variety of DE-PTO configurations, and are discussed here for the first time.

Sect. 3 illustrates results from dry-run laboratory tests on the Poly-OWC PTO, discussing the choice of suitable materials for small-scale wet-run tests and presenting an assessment of the PTO performance in conditions of prescribed operational deformations.

Sect. 4 presents a brief description of experimental facilities available at UEDIN, which have been employed for the described tests. In particular, the first two campaigns were carried out in the wave flume facility, while the last experiment (on the floating Poly-OWC) were carried out in the FloWave facility.

Sect. 5-7 describe experimental setups, results and model validations for the three test campaigns, as detailed in the following.

Sect. 5 reports experimental results from the first experimental campaign (Dec. 2013), that was carried out on a fixed-structure OWC prototype (see Figure 1.a). This was the first functional in-tank test on a PolyWEC device, so the aim was to assess controllers and define testing procedures. For this reason, the hydrodynamics of the collector was not optimized, and the device was found not to resonate with typical incoming sea-states. However, useful insights were obtained for successive tests and power was actively generated by the polymeric PTO.

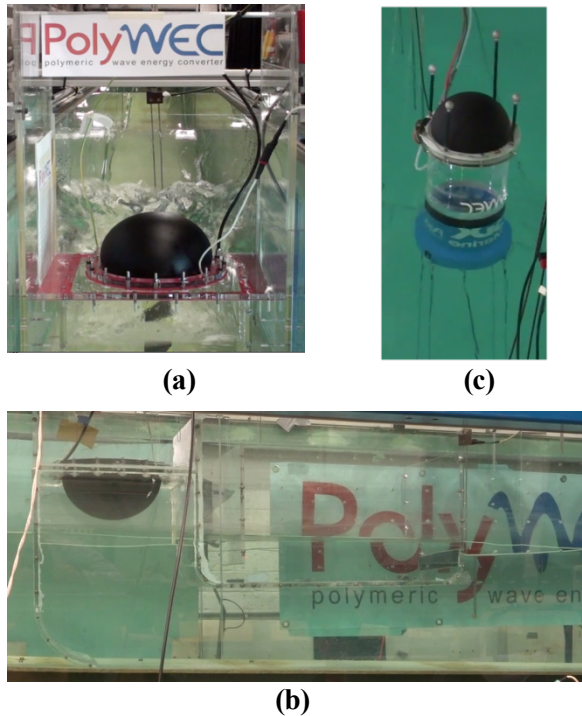


Figure 1 – Photographs from wave-tank tests of three Poly-OWC prototypes: (a) Fixed-structure OWC – base design; (b) Fixed-structure OWC – optimized design; (c) Bottom-moored floating OWC.

Sect. 6 shows results from a second campaign of tests (Aug. 2014), carried out on a fixed-structure Poly-OWC with optimized collector shape (an added mass duct was placed at the inlet of the chamber to lower the device natural frequency), shown in Figure 1.b. This prototype was equipped with a functional CD-DEG whose controller was implemented through an optimized electric circuit (an in-parallel capacitance was connected to the DEG, to enable the application of larger voltages, without inducing membrane breakdown). The enhanced hydrodynamic and control capabilities of this device resulted in a larger power output of the device.

Sect. 7 describes results from a floating Tubular Poly-OWC (T-Poly-OWC) prototype, that was tested in February 2015 (see Figure 1.c). The T-Poly-OWC had a collector based on a design proposed by the Spanish company Sendekia, i.e., the collector was equipped with a submerged convergent-divergent aperture, aimed at increasing the added mass of the device. The T-Poly-OWC was tested both in regular and irregular waves. Results were encouraging, but the power output was limited by hydrodynamic viscous losses and motions of the collector. An important outcome was represented by the effective operation of the PTO controller in irregular waves. Future work on this concept is foreseen, aimed at improving measured performance: a larger-scale fixed-collector T-Poly-OWC may be tested in the future.

All of the experimental results were used to perform validations of the hydro-electro-mechanical models proposed so far. In particular, separate validations were provided for the CD-DEG model and for the collectors hydrodynamic models. In general, a good agreement between models and tests has been observed, especially for what concerns the CD-DEG electro-mechanical model.

Sect. 8 draws some conclusions and introduces possible future experiments on improved architectures of the Poly-OWC concept and different PolyWEC concepts (e.g., direct-contact PolyWECs).

2 POLYWEC PROTOTYPES SCALING

In this section, Froude scaling laws for PolyWECs are derived, with the aim of providing rules to scale PolyWECs concepts for the design of representative small-scale prototypes. Froude scaling is a well-established and agreed methodology used to define dimensions and procedures to perform small-scale tank tests on WECs in similarity conditions [6]. Froude scaling is based on the basic observation that acceleration of gravity is constant with respect to the scale. Thus, in order to produce consistent scaled dynamic time-series, all accelerations must be the same at any scale.

Assuming a given scale factor, f_s , for the geometry of the WEC (with respect to a benchmark full-scale case), kinematic and dynamic parameters scale according to the rules reported in Table 1, and wave periods and heights employed in the experiments must be scaled accordingly.

If DE PTO sizes are scaled by a factor f_s , the force/torque response varies in a way which is generally non-consistent with Froude scaling and the factors of Table 1. This happens, since the electro-mechanical response of elastomers does not scale proportionally to the scale factor. Therefore, in order to perform consistent small-scale tests on PolyWEC prototypes, case-related rules for DE PTOs have to be employed. A general set of rules is here presented, with reference to two macro-classes of DE PTOs: 1) floater-driven PTOs, whose displacement is driven by the motion of a primary mechanical interface (e.g., buoy, flap, etc.), 2) direct-contact PTO, in which the DE is in contact with a fluid (air and/or water), without any further mechanical moving part. In both cases, scaling is set by applying different scaling factors to the different dimensions of the DEG.

Table 1 - Froude scaling coefficients for the main physical quantities

Quantity		Scale Fact.
Kinematic	Length (geometric dimensions; wave heights, H_s and H)	f_s
	Time (time intervals; wave periods, T_e and T)	$f_s^{1/2}$
	Velocity	$f_s^{1/2}$
	Frequency, angular velocity	$f_s^{-1/2}$
	Acceleration	1
Dynamic	Mass	f_s^3
	Moment of inertia	f_s^5
	Force	f_s^3
	Torque	f_s^4
	Pressure	f_s
	Energy	f_s^4
	Power	$f_s^{7/2}$
Hydrodin. Parameters	Added mass, M_{add} and M_∞	f_s^3
	Added moment of inertia, I_{add} and I_∞	f_s^5
	Linear radiation damping	$f_s^{5/2}$
	Angular radiation damping	$f_s^{9/2}$
	Linear hydrostatic stiffness	f_s^2
	Angular hydrostatic stiffness	f_s^3

2.1 Linear/Rotary DEGs coupled with a moving primary interface (floater-driven)

In this section we analyze DEGs (either rotary or linear) which are coupled with a floating body (primary mechanical interface), like those schematically represented in Figure 2.

For simplicity, we consider a single-DoF floating WEC that deforms a single-DoF DEG. Due to direct coupling, the generalized displacement of the WEC, s (corresponding to a rotation or a linear displacement), equals the displacement of the DEG along its generalized deformation direction.

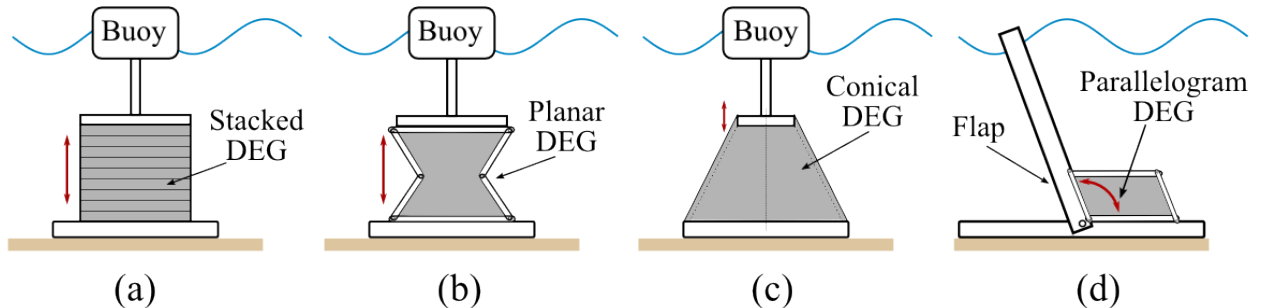


Figure 2 – Some concepts of DE PTOs directly coupled with a floating primary interface: (a)-(c) heaving buoy with linear generators (stacked, planar and conical DEG respectively); (d) pitching flap with rotary parallelogram-shaped DEG.

The load, L_{DEG} , exerted by the DEG on the WEC interface (representing a force if s is a linear displacement, or a torque if s is an angle) is found from the following energy balance (see also [10]):

$$L_{DEG} = -\frac{d(U_{el} + U_{es} + U_g + E_k)}{ds} + V \frac{dQ}{ds} \quad (1)$$

where U_{el} , U_{es} , U_g are elastic, electrostatic and gravitational potential energy respectively, E_k is the kinetic energy of the elastomer, Q and V are the instantaneous charge and electric potential difference (voltage) acting on the DEG.

The energy contributions in between parentheses are given by:

$$U_{el} = \int_{\Omega} \Psi(\lambda_i) d\Omega; \quad U_{es} = \frac{\epsilon}{2} \int_{\Omega} E^2 d\Omega; \quad U_g = \int_{\Omega} \rho g h \cdot d\Omega; \quad E_k = \frac{1}{2} \int_{\Omega} \dot{s}^2 dI. \quad (2)$$

In equation (2), Ω stands for the elastomer volume, ϵ is the elastomer permittivity, E is the local electric field and g is gravity acceleration. Ψ represents the strain energy function describing the material hyperelastic behavior [11] and λ_i ($i=1, 2, 3$) are the principal stretches. In the expression of U_g , h represents the vertical elevation of an infinitesimal polymer portion above a reference position and ρ the polymer density. In the expression of E_k , \dot{s} is the time derivative of s and dI is the inertia of an infinitesimal polymer portion, reported to generalized coordinate s (notice that I is a mass if s is a linear coordinate and a moment of inertia if s is an angle). In energy balance (1), losses due to mechanical hysteresis and leakage currents through the dielectric have been neglected.

Provided that, in the undeformed configuration, the DEG has uniform thickness, t_0 , and electrode pairs with equal surface, A_0 , it is convenient to introduce dimensionless charge and voltage (see also [1]), Q^* and V^* , as follows:

$$Q^* = \frac{Q}{\epsilon A_0 E_{ref}}; \quad V^* = \frac{V}{t_0 E_{ref}}, \quad (3)$$

where E_{ref} is a reference value of the electric field (e.g., in [1] the break-down electric field of the material, E_{BD} , is used). Notice that Q^* and V^* are independent of the absolute dimensions of the DEG and the applied voltage: they only depend on the material stretch and the ratio between the applied electric field and the reference electric field, E_{ref} .

With the definitions introduced in (3), the last addendum of equation (1) takes the following form:

$$V \frac{dQ}{ds} = \varepsilon \Omega E_{ref}^2 V^* \frac{dQ^*}{ds}. \quad (4)$$

For future convenience, the following components of L_{DEG} are introduced:

$$\begin{aligned} L_{DEG} &= L_{DEG,el} + L_{DEG,es} + L_{DEG,g} + L_{DEG,k}, \\ L_{DEG,el} &= -\frac{d}{ds} \int_{\Omega} \Psi(\lambda_i) d\Omega; \quad L_{DEG,es} = \varepsilon \Omega E_{ref}^2 V^* \frac{dQ^*}{ds} - \frac{\varepsilon}{2} \frac{d}{ds} \int_{\Omega} E^2 d\Omega; \\ L_{DEG,g} &= -\frac{d}{ds} \int_{\Omega} \rho g h \cdot d\Omega; \quad L_{DEG,k} = -\frac{1}{2} \frac{d}{ds} \int_{\Omega} \dot{s}^2 dI. \end{aligned} \quad (5)$$

The energy generated by the DEG in a cycle is given by

$$W = \int Q dV = \varepsilon \Omega E_{ref}^2 \int Q^* dV^* = \varepsilon \Omega E_{ref}^2 \int \gamma(\lambda_s) d\lambda_s, \quad (6)$$

where the dependence of the circulation integral on the DEG size has been cancelled and replaced with a function of the cyclic strain history (here λ_s , i.e. the stretch in the direction of s , is used to univocally identify the strain state, and $\gamma(\lambda_s)$ is a function that depends on the stretch and on the control pattern).

Let us now compare a full-scale PolyWEC device and small-scale prototype scaled by a factor f_s . As s corresponds to a displacement of the WEC, it must scale with f_s if it represents a linear displacement, or must remain the same if it represents an angular displacement. Let us first assume that each of the sizes of the DEG is scaled by f_s , and the electric variables (Q and V) are scaled in a way that the instant electric field, E , remains the same in full-scale and small-case. With these hypotheses, the addenda of L_{DEG} and the energy generated in a cycle, W , scale according to Table 2.

Table 2 - Scaling factor for energy and load components for a fully scaled DEG (geometry scaled by f_s) in two cases: a) s is a linear displacement, b) s is an angular displacement

Quantity	Scale Fact.	
	s linear displ.	s angular displ.
s	f_s	1
$L_{DEG,el}$	f_s^2	f_s^3
$L_{DEG,es}$	f_s^2	f_s^3
$L_{DEG,g}$	f_s^3	f_s^4
$L_{DEG,k}$	f_s^3	f_s^4
W	f_s^3	f_s^3

Table 2 shows that:

- The different addenda of the DEG load do not scale with the same coefficient; as a consequence, it is not possible to design a scaled DEG which is in a condition of “ideal similarity” with respect to the original one. Attention should be then addressed only on the components of the load which are numerically more relevant or functional to energy conversion.
- It has been assessed [2] that, for the architectures and sizes of interest in wave energy applications, inertial and gravitational loads are much smaller with respect to electro-elastic contributions. Therefore, attention will be hereafter addressed to $L_{DEG,el}$ and $L_{DEG,es}$ only.
- If all of the DEG dimensions are scaled by f_s , the quantities $L_{DEG,el}$, $L_{DEG,es}$ and W do not scale as required by Froude scaling and Table 1. As a consequence, in order to obtain a Froude-scaled

PolyWEC device, the DE PTO geometry cannot be uniformly scaled. As shown in the following, different scale factors have to be applied to the different dimensions.

In the following, a practical set of scaling laws for different PolyWEC architectures are presented. In all of the reported cases, it is assumed that the type of DE material employed in full-scale and in small-scale experiments is the same, and it is activated using the same cyclic values of the electric field (as the electric failure of the material, as well as its maximum convertible energy density, directly depend on E). The different sizes of the DEG are scaled with different factors, in a way that the polymer volume scales with a factor f_s^4 (instead of f_s^3). This provides a PTO whose electro-elastic response and converted energy scale as required by Froude law. On the other hand, the PTO kinetic and gravitational energy contributions will have different weights at different scales.

Two categories of floater-driven PolyWECs are identified: one in which DEG electrodes are perpendicular to the WEC interface motion, and the other in which the displacement is parallel to the plane of the electrodes.

2.1.1 WEC displacement perpendicular to the DEG electrodes

In this section, we consider DE PTOs featuring electrodes perpendicular to the WEC interface displacement, s . Reference is made to the Stacked-DEG (S-DEG, i.e., a stack of DE layers, each with a couple of electrodes), which is shown in Figure 3.a and described in [2]-[12]. The S-DEG can be employed as PTO for heaving buoy, as shown in Figure 2.a.

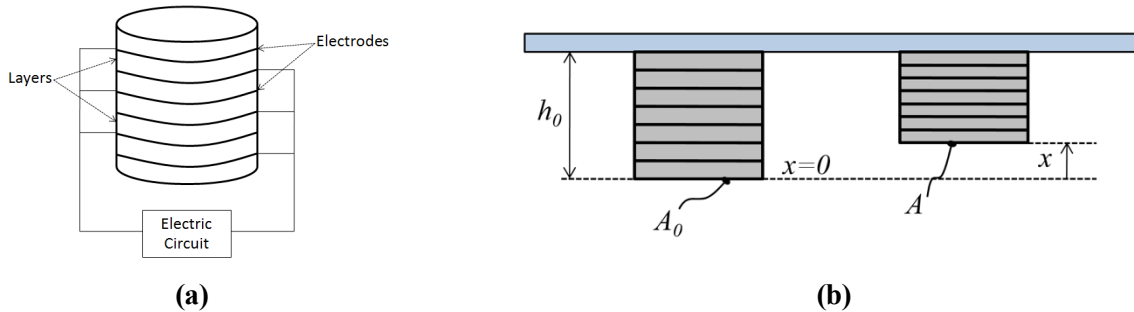


Figure 3 – (a) S-DEG scheme; (b) S-DEG in the undeformed (left) and deformed (right) configuration.

The displacement of S-DEG in longitudinal direction is here referred to as x ($s=x$). Indicating with t_0 and A_0 the undeformed height and surface respectively, the DEG deformation is assumed to be homogeneous and uniaxial, the stretch in x direction reads as

$$\lambda_1 = 1 - \frac{x}{t_0}. \quad (7)$$

and the electrodes surface (regardless their shape) varies as

$$A = \lambda_1^{-1} A_0.$$

Rearranging equation (5), neglecting inertial and gravitational contributions, and considering that the electric field within the material is homogeneous, the force L_{DEG} (here referred to as F_{S-DEG}) has the following expression:

$$F_{S-DEG} = F_{S-DEG,el} + F_{S-DEG,es} \\ F_{S-DEG,el} = -A_0 \frac{d\Psi(\lambda_1)}{d\lambda_1}; \quad F_{S-DEG,es} = \frac{\epsilon A_0 E^2}{\lambda_1} \quad (8)$$

where Ψ has been univocally expressed as a function of λ_1 only.

Both of the force contributions in equation (8) only depend on the size scale through factor A_0 (as the instant electric field, E , is kept constant at different scales). As observed before, in order to set up a scaled PTO, coordinate x must scale with f_s . In order to preserve strain variations, height t_0 (parallel to x) must scale with f_s . Since F_{S-DEG} is required to scale with f_s^3 , the electrodes surface, A_0 , should scale with f_s^3 . As a

consequence, the overall polymer volume scales with f_s^4 and the energy converted in a cycle (see equation (6)) scales with f_s^4 , as required by Table 1.

Although the DEG force and converted energy scale according to Froude law, the DEG has a different geometric aspect ratio (i.e., the ratio $h_0/A_0^{1/2}$) at different scales. This “non-ideal” scaling needs to be considered with care since it provides different secondary responses of the S-DEG (for instance, compression buckling [12]) at different scales.

2.1.2 WEC displacement coplanar with the DEG electrodes

In this subsection, we consider Planar DEGs (P-DEGs) used as PTOs for a WEC interface whose displacement vector lies on the plane of the electrodes. This kind of DEGs usually operate in plane-stress conditions (i.e., they are free to expand in the direction of the DE layers thickness).

Two examples of linear P-DEGs are shown in Figure 4.a (see also [13]) and Figure 4.b. These DEGs undergo 1-DoF deformations whose principal stretches λ_1 and λ_2 lie on the plane of the (undeformed) electrodes and the third principal stretch (in the direction of the DE layers thickness) is given by incompressibility condition:

$$\lambda_3 = (\lambda_1 \lambda_2)^{-1}. \quad (9)$$

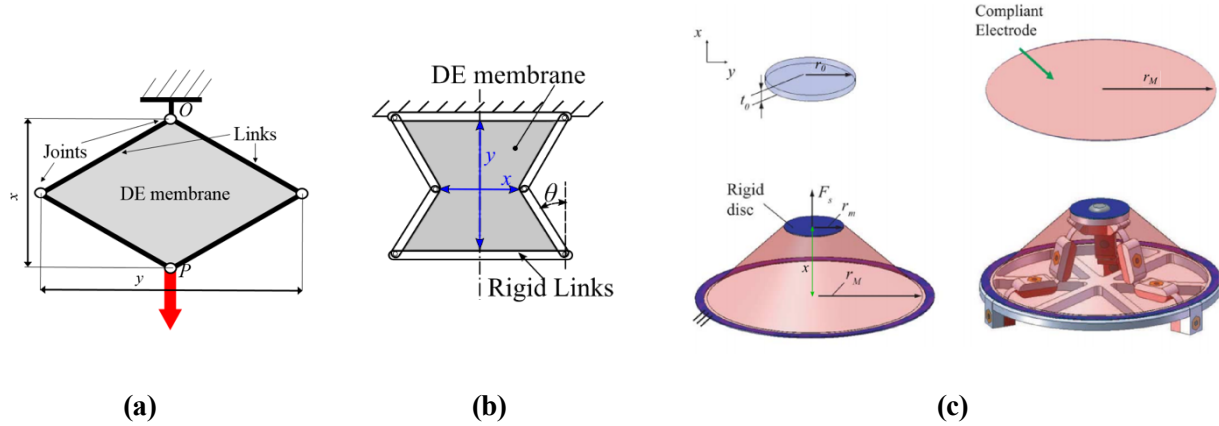


Figure 4 – (a) Lozenge-Shaped DEG [13], (b) Six-link planar DEG, (c) Conical DEG [14].

In the concept in Figure 4.a (Lozenge-Shaped DEG), stretches are uniform within the DE volume, while in the concept of Figure 4.b (Six-link planar DEG) they vary within the DE sheets surface.

For these DEGs, the strain energy function, Ψ , can be expressed as a function of λ_1 and λ_2 only without any loss of generality.

Indicating with x and y two in-plane dimensions of the DEG (with x parallel to the WEC displacement, s), λ_1 and λ_2 can be expressed as a function of the ratio between x and y actual values and their unstretched values (x_0, y_0):

$$\lambda_1 = \lambda_1(x/x_0, y/y_0); \quad \lambda_2 = \lambda_2(x/x_0, y/y_0). \quad (10)$$

Basing on equation (9), the infinitesimal element volume, $d\Omega$, can be expressed as a surface differential:

$$d\Omega = \frac{\Omega}{\lambda_1 \lambda_2} \frac{dA}{A_0} \quad (11)$$

where A and A_0 represent the deformed and unstretched electrodes surfaces respectively.

Rearranging equations (5), the DEG force components can be written as

$$\begin{aligned}
 F_{P-DEG} &= F_{P-DEG,el} + F_{P-DEG,es} \\
 F_{P-DEG,el} &= -\frac{\Omega}{x_0} \frac{d}{d(x/x_0)} \int_A \frac{\Psi(\lambda_1, \lambda_2)}{\lambda_1 \lambda_2} \frac{dA}{A_0} \\
 F_{P-DEG,es} &= \frac{\varepsilon \Omega E_{ref}^2}{x_0} V^* \frac{dQ^*}{d(x/x_0)} - \frac{\varepsilon \Omega}{2 x_0} \frac{d}{d(x/x_0)} \int_A \frac{E^2}{\lambda_1 \lambda_2} \frac{dA}{A_0}.
 \end{aligned} \tag{12}$$

In order to obtain a P-DEG response which scales with Froude laws, the following has to be considered:

- x (and x_0) must scale with factor f_s , as it is directly related to the WEC displacement, s .
- If all of the other in-plane dimensions (e.g., y, y_0) also scale with f_s , DEGs with different scales undergo the same deformations (λ_1 and λ_2). Moreover, the different derivative factors in equation (12) result scale-independent. Thus, the P-DEG force scales proportionally to Ω/x_0 .
- In order to provide a DEG force scaling with f_s^3 , the DE material thickness (designed as t_0 in the unstretched configuration) must scale with f_s^2 . This results in DEG thickness to decrease dramatically as the scale decreases.

A similar scaling law applies for a different class of linear DEGs, namely Conical DEGs (C-DEGs, see Figure 4.c) [14]. Such DEGs do not have planar electrodes, but still they are based on a DE membrane (or stack of layers) which is free to expand in thickness direction. C-DEGs consists of two frames (an outer ring with radius r_M , and an inner ring with radius r_m) to which an active DE membrane is clamped. In the undeformed configuration, the membrane has radius r_0 and thickness t_0 . The linear displacement between the two frames (which coincides with the displacement of the coupled WEC interface and is designed as x) is responsible for the DEG electrodes to assume a deformed shape which is approximated by a truncated cone. Provided that the membrane thickness is small with respect to the other dimensions, the surfaces of the two electrodes are approximately equal.

As shown in [14], the stretches within the material are uniform and given by equation (13):

$$\lambda_1 = \frac{r_M}{r_0} \sqrt{1 + \frac{x^2}{(r_M - r_m)^2}}; \quad \lambda_2 = \frac{r_M}{r_0}, \tag{13}$$

and, basing on (5), the C-DEG force has the following form:

$$\begin{aligned}
 F_{C-DEG} &= F_{C-DEG,el} + F_{C-DEG,es} \\
 F_{C-DEG,el} &= -\frac{\Omega}{r_M - r_m} \left(\lambda_2^2 - \frac{\lambda_2^4}{\lambda_1^2} \right)^{1/2} \frac{\partial \Psi(\lambda_1, \lambda_2)}{\partial \lambda_1} \\
 F_{C-DEG,es} &= \frac{\varepsilon \Omega E^2}{r_M - r_m} \left(\frac{\lambda_2^2}{\lambda_1^2} - \frac{\lambda_2^4}{\lambda_1^4} \right)^{1/2}
 \end{aligned} \tag{14}$$

Displacement x scales with f_s . If also r_0, r_m, r_M scale with f_s , the state of deformation is scale-invariant. Therefore, to make the force components scale in the proper way, the DE membrane thickness should scale with f_s^2 , as in the previous example.

Last example of P-DEG are rotary planar DEGs, which undergo a deformation induced by a rotation, $s = \theta$, above an axis perpendicular to the electrodes plane. An example is represented by Parallelogram-Shaped DEG (PS-DEG), which is the rotary version of abovementioned Lozenge-Shaped DEG, and can be employed as PTO on pitching WECs, as shown in Figure 2.d (see also [15]).

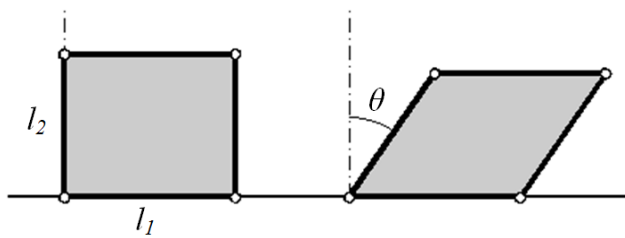


Figure 5 – Sketch of Parallelogram-Shaped DEG, with links of length l_1 and l_2 .

For PS-DEG [10], in-plane principal stretches are uniform, directed along the parallelogram bisectors, and given by:

$$\lambda_1 = \lambda_{1p} \sqrt{1 - \sin \theta}; \quad \lambda_2 = \lambda_{2p} \sqrt{1 + \sin \theta}, \quad (15)$$

where λ_{1p} and λ_{2p} are the principal stretches in reference configuration, $\theta = 0$. Notice that stretches do not depend on the scale or on the aspect ratio of the parallelogram-mechanism. Therefore, using equation (5), neglecting kinetic and gravitational terms and replacing s with θ , it is found out that the DEG torque is proportional to Ω . To properly scale the DEG, it is sufficient that Ω scales with f_s^4 regardless how the different dimensions are scaled.

2.2 Inflated (or direct-contact) DEGs

In this section, attention is focused on DEGs, referred to as Inflated DEGs (I-DEGs), which are deformed by a pressure difference acting between opposite faces. In this kind of PTOs, motion is not imposed by a rigid body displacement, but it is the result of a direct fluid-membrane interaction.

Two types of architectures are envisaged for I-DEG PTOs: 1) air-to-air operation, in which both the faces of the DEG are in contact with air at different pressure, like in the PolyOWC application (see Figure 6.a) [1], [16], [17]; 2) water-to-air application, in which one side of the DEG is in direct contact with sea water, while the other faces an air chamber, like in PolySubMe application (see Figure 6.b) [2]. In both cases, DEG displacements are driven by direct contact with a fluid (water and/or air), without any further floating body as interface.

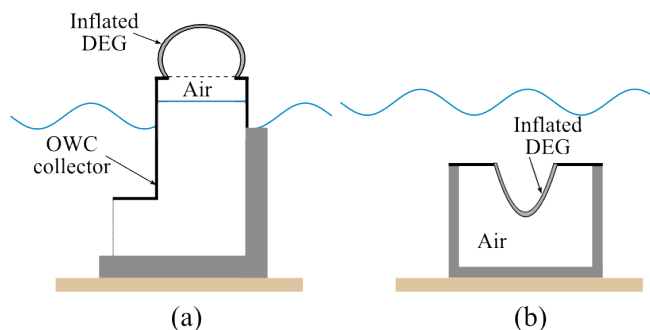


Figure 6 – PolyWECs based on Inflated DEG: (a) PolyOWC; (b) PolySubMe

In both cases, it is assumed that 1) pressure difference acts on a surface (generally not planar) which is parallel to the DEG electrodes; 2) the overall DEG thickness (perpendicular to the electrodes) is sufficiently small, thus opposite faces have approximately the same surface and the theory of elastic thin shells holds. Scaling of direct-contact PolyWECs, like those shown in Figure 6, is a more complicated task than the previously examined scaling of floater-driven PolyWECs. Indeed, while in the previous cases the PTO was constituted only by the DE membrane, here the PTO is the sum of DEG and air volume (present in both the concepts of Figure 6). Therefore, scaling must take into account both of these subsystems.

Some preliminary definitions are introduced here for convenience:

- p_a is the relative air pressure (i.e., absolute pressure minus atmospheric pressure, p_{atm}) in a generic configuration;
- p_{eq} is the relative air pressure in the equilibrium configuration (i.e., in absence of waves and water displacements). In particular, p_{eq} expresses the initial pressurization of the air chamber and is a setting parameter of the experiment.
- p_{DEG} is the pressure difference between opposite membrane faces, and it is a local variable (in general, it changes at any point of the surface).

To set up a properly scaled experiment, it is necessary that $p_a - p_{eq}$ scales with f_s (as required by Froude scaling), as this pressure difference is involved in the momentum balance of the moving water volume. Here, we propose a scaling methodology in which both p_a and p_{eq} scale with f_s .

As regards p_{DEG} , it has the following expression for the two WECs in exam:

$$\begin{aligned} p_{DEG} &= p_a, \quad \text{for PolyOWC} \\ p_{DEG} &= p_a - p_w, \quad \text{for PolySubMe} \end{aligned} \tag{16}$$

where p_w is a pressure due to local hydrodynamic contributions, and it intrinsically scales with f_s as provided by Froude scaling. Basing on (16) and on the previous assumptions, also p_{DEG} is required to scale with factor f_s .

In the following, two sub-problems are tackled: 1) scaling of the DE membrane (aimed at guaranteeing a proper scaling of p_{DEG}); 2) scaling of the air volume (i.e., proper scaling of p_a).

2.2.1 DE membrane scaling

In the mathematical formulation presented in this section, we consider for simplicity I-DEGs that, in the undeformed configuration, are flat circular membranes, and undergo axisymmetric deformations.

With reference to Figure 7, the infinitesimal ring-shaped element that, in the undeformed configuration, has inner and outer radius equal to R and $R+dR$ respectively (with R between 0 and e_0), in the deformed configuration is identified by polar coordinates r and z (with r between 0 and e).

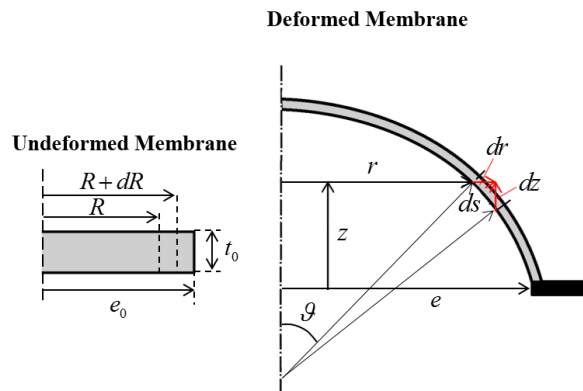


Figure 7 - Circular I-DEG in undeformed (left) and deformed (right) configuration

For an axisymmetric deformed membrane, principal stretches (in longitudinal, latitudinal and thickness direction respectively) read as

$$\lambda_1 = \sqrt{\left(\frac{dr}{dR}\right)^2 + \left(\frac{dz}{dR}\right)^2}; \quad \lambda_2 = \frac{r}{R}; \quad \lambda_3 = (\lambda_1 \lambda_2)^{-1}, \tag{17}$$

and according to [18], continuum equations of motion are

$$\begin{aligned}\rho R \frac{\partial^2 r}{\partial t^2} &= \frac{\partial}{\partial R} \left(\frac{\sigma_1 R}{\lambda_1^2} \frac{\partial r}{\partial R} \right) - \frac{p_{DEG} R \lambda_2}{t_0} \frac{\partial z}{\partial R} - \frac{\sigma_2}{\lambda_2} \\ \rho R \frac{\partial^2 z}{\partial t^2} &= \frac{\partial}{\partial R} \left(\frac{\sigma_1 R}{\lambda_1^2} \frac{\partial z}{\partial R} \right) + \frac{p_{DEG} R \lambda_2}{t_0} \frac{\partial r}{\partial R} - \rho g R\end{aligned}\quad (18)$$

where ρ is the membrane density, t_0 is the undeformed membrane thickness (see Figure 7), σ_1 and σ_2 are the local stresses in longitudinal and tangential direction respectively:

$$\sigma_1 = \lambda_1 \frac{\partial \Psi(\lambda_1, \lambda_2)}{\partial \lambda_1} - \varepsilon E^2; \quad \sigma_2 = \lambda_2 \frac{\partial \Psi(\lambda_1, \lambda_2)}{\partial \lambda_2} - \varepsilon E^2, \quad (19)$$

where strain-energy function, Ψ , has been expressed as a function of λ_1 and λ_2 only without losing generality, and E is the local value of the electric field. If the same material is used at full and small scale and the voltage is properly scaled to keep the electric field equal regardless the DEG size, σ_1 and σ_2 are the same at different scales (provided that deformation is the same).

As done for floater-driven DE PTOs, inertial and gravitational contributions are neglected, thus p_{DEG} can be written in the following alternative manners:

$$\begin{aligned}p_{DEG} &= \frac{t_0}{R \lambda_2 \frac{\partial z}{\partial R}} \left[\frac{\partial}{\partial R} \left(\frac{\sigma_1 R}{\lambda_1^2} \frac{\partial r}{\partial R} \right) - \frac{\sigma_2}{\lambda_2} \right] \\ p_{DEG} &= - \frac{t_0}{R \lambda_2 \frac{\partial r}{\partial R}} \frac{\partial}{\partial R} \left(\frac{\sigma_1 R}{\lambda_1^2} \frac{\partial z}{\partial R} \right)\end{aligned}\quad (20)$$

As discussed above, p_{DEG} is required to scale with a factor f_s . If the DEG radial size (e, e_0) and its displacements (r and z) scale with f_s , deformations are the same at any scale, and the DEG equilibrium pressure depends on the scale through a factor t_0/R (where R varies with f_s). Similarly to P-DEGs, if t_0 is scaled by f_s^2 , pressure p_{DEG} gets properly scaled. Again, this scaling does not produce scaled inertial and gravitational potential energy contributions.

As regards cyclic converted energy, considerations outlined in Sect. 2.1 and equation (6) still apply: in presence of same stretches, generated energy is proportional to DE volume, and, with the mentioned assumptions, it scales with f_s^4 , as required by Table 1.

2.2.2 Air volume scaling

In this subsection, scaling of the air volume is discussed. The focus is providing the relative air pressure, p_a , to scale with f_s . An alternative approach with respect to that presented here is treated in [19].

It is assumed that, in the mentioned applications, air compression/expansion is described by polytropic processes:

$$(p_a + p_{atm}) V_a^n = (p_{eq} + p_{atm}) V_{eq}^n, \quad (21)$$

where V_a is the instant air volume in a generic configuration and V_{eq} the reference equilibrium volume, and n is a polytropic exponent; p_{atm} and n are scale-independent.

The instant air volume can be written as the sum of the equilibrium volume and volume variation, ΔV , i.e., $V_a = V_{eq} + \Delta V$. Equation (21) can be linearized (with respect to $\Delta V = 0$), leading to the following expression:

$$p_a \approx p_{eq} - n(p_{eq} + p_{atm}) \frac{\Delta V}{V_{eq}} \quad (22)$$

It has been already observed that p_{eq} scales as f_s ; moreover, provided that the membrane thickness is small compared to the other dimensions, ΔV results from water surface and/or membrane displacements (r and z), thus it varies as f_s^3 . To make p_a scale with f_s , it is only possible to properly set the initial volume, V_{eq} . In particular, indicating with V_{eq}^s the scaled value of the equilibrium volume (in correspondence of full-scale reference pressure and volume p_{eq} and V_{eq}), it is found that:

$$V_{eq}^s = \frac{f_s p_{eq} + p_{atm}}{p_{eq} + p_{atm}} f_s^2 V_{eq}. \quad (23)$$

E.g., if in the equilibrium configuration the membrane is flat (i.e., $p_{eq} = 0$), the initial air volume should scale as f_s^2 instead of f_s^3 . Scaling by f_s all of the air chamber dimensions would indeed provide a very stiff small-scale air volume, which would not represent the actual full-scale behavior.

Notice that, since equation (23) comes from a linearization, it provides a rigorously correct scaling only if air volume variations (ΔV) are small compared to V_{eq} .

According to previous considerations, air volumes needed for small-scale experiments are big compared to the overall setup volume, and they can be enabled by providing the setup with an external additional air tank, as proposed also by [19].

However, implementation of this solution might be complicated and technically onerous, e.g., the external air reservoir should be connected to the device by means of a piping system, which has to be driven along the tank perimeter. Moreover, connecting two air volumes by means of a pipe (with small diameter with respect to the reservoir dimensions) may lead to other undesired dynamic effects, which are not representative of the full-scale framework.

2.3 Concluding remarks

Scaling laws for DE PTOs have been studied with the aim of providing DEGs whose response scales according to Froude's laws. Two classes of PolyWECS have been considered: floater-driven PTOs, whose deformation is imposed by the displacement of a floating interface; direct-contact DE PTOs, which consist in an inflatable DE membrane and an air volume.

A schematic resume of scaling factors for a variety of DEGs is reported in Table 3.

The proposed scaling methodology relies on the application of different scale factors to the different DEG dimensions.

Other scaling approaches would be possible, e.g., employing different polymers, with different mechanical properties, at different scales, or scaling the electric control variables (i.e., electric field) in order to generate a scaled PTO response. However, these approaches would produce a properly scaled behavior only in a restricted neighborhood of the equilibrium configuration (with reference to which scaling is performed), and would not have the general validity of the approach proposed here.

Table 3 - Engineering scaling factors for the examined DE PTO categories. Superscript s indicates scaled quantities (in comparison with full-scale quantities).

DEG type	Scaling factors
Stacked DEG (electrodes \perp to WEC displacement)	$t_0^s = f_s t_0; A_0^s = f_s^3 A_0$
Linear planar DEG (WEC displacement coplanar with electrodes)	$x_0^s = f_s x_0; y_0^s = f_s y_0;$ $A_0^s = f_s^3 A_0; t_0^s = f_s^2 t_0$
Conical DEG	$r_0^s = f_s r_0; r_m^s = f_s r_m;$ $r_M^s = f_s r_M; t_0^s = f_s^2 t_0$
Rotary planar DEG (rotation axis \perp to electrodes)	$\Omega^s = f_s^4 \Omega$
Inflated DEG (pressure \perp to electrodes)	$e_0^s = f_s e_0; e^s = f_s e; t_0^s = f_s^2 t_0$ $p_{eq}^s = f_s p_{eq}; V_{eq}^s = \frac{p_{eq}^s + p_{atm}}{p_{eq} + p_{atm}} f_s^2 V_{eq}$

3 DRY-RUN TESTS ON CIRCULAR DIAPHRAGM DEG

In this section, we present experimental setup, techniques and results for dry-run testing of Circular Diaphragm DEGs (CD-DEGs). These tests have been briefly presented in [5], and are here reported in detail. It is worth remembering that dry-run tests on a stand-alone PTO system are useful to 1) assess the potential performance of the DE-PTO (energy convertible in a cycle); 2) characterize/verify the response of the membranes against predictive models; 3) develop and test control algorithms through Hardware-in-the-Loop tests.

In the following, an experimental setup available at SSSA laboratories to test CD-DEGs under dynamic conditions is briefly described (a more detailed description has been reported in D3.1). Additionally, mechanical inflating tests on different materials are presented together with experimental generation tests.

3.1 Setup

The test-bench, developed within the PolyWEC project, available at SSSA laboratories to perform dry-run simulations of CD-DEG systems is schematized in Figure 8 [21]. Such test-bench comprises: a pneumatic piston; a small-scale CD-DEG prototype; a high-voltage (HV) electronics for CD-DEG charge and discharge; a real-time unit for overall system control and data acquisition. Specific details of each sub-system are provided below.

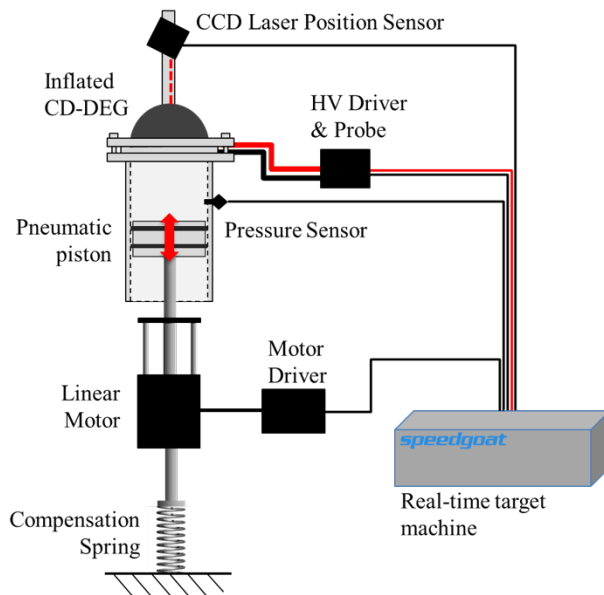


Figure 8 - Schematic of the experimental test-rig for dry-run laboratory tests.

Mechanical Sub-system. To simulate the Poly-OWC air chamber, a custom made pneumatic cylinder has been constructed that features: a polycarbonate cylinder tube (with internal diameter $e = 130\text{mm}$); a movable piston; the CD-DEG specimen as upper end-cap. Air leakages are minimized by using a planar annular gasket with a tight screwed fixture on the CD-DEG side and appropriate pneumatic circular seals on the piston side. The piston is actuated via a brushless linear motor (P01-37x120F/200x280-HP by LinMot), with embedded encoder that is used to measure piston position, x . A pressure sensor (MPX12 by Freescale Semiconductor) installed on the cylinder tube is used to measure the differential pressure, p , between cylinder chamber and ambient air. A high-speed high-accuracy CCD laser displacement sensor (LK-G152 by Keyence), which is mounted on top of the cylinder head, is used in order to measure CD-DEG tip displacement, h . The pneumatic cylinder is mounted vertically and an elastic spring is introduced in order to compensate for the weight of both piston and motor slider.

HV Electronics. A custom made HV driving electronics has been developed to control CD-DEG charge and discharge. The considered driving electronics has a HV power supply (10C24-P125 by UltraVolt).

The electronic conditioning circuit is adjusted in each specific experiment, and it is equipped, e.g., with

- Constant capacitors, which are used, e.g., to charge/discharge the CD-DEG and enable the measurement of the transferred charge through the measurement of the voltage at their terminals.
- HV reed relays that alternatively connect the CD-DEG electrodes to the power supply, to the ground, or to other electrical components (capacitors, resistances).
- Resistances used to limit the peak current that occurs during CD-DEG discharge at relays closure, or to discharge the DEG.

To measure electric potential differences on the CD-DEG or other capacitors, custom-made HV probes have been implemented that features very high input resistance (e.g., $50\text{G}\Omega$), which drastically limits the drain of charge from the capacitors electrodes, and large bandwidth, which is obtained thanks to a capacitor compensation network.

CD-DEG. The setup can house CD-DEG with radius (in the flat pre-stretched configuration) $e=65\text{mm}$. CD-DEGs are obtained by pre-stretching one or more overlapping layers of DE material over a polycarbonate ring. Upper and lower face of the DEG are covered by compliant electrodes, which on a laboratory scale are realized using a conductive carbon grease or by directly using conductive elastomer layers. To prevent charge leakage through air, the HV electrode can be eventually encapsulated via an additional layer of DE material (in this case, of course, the additional layer will affect the mechanical pressure-deformation response of the system). Figure 9 shows a picture of an acrylic CD-DEG (made of VHB-4905) in the flat horizontal and inflated configuration respectively.

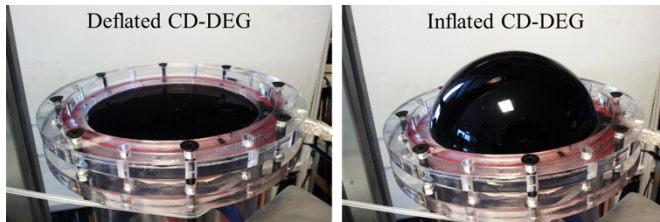


Figure 9 – CD-DEG made by acrylic VHB-4905 in the flat and expanded configuration. Electrodes are made of MG-Chemicals 846 conductive grease. The upper HV electrode is equipped with a guard acrylic layer against charge leakage through air.

3.2 CD-DEG electro-mechanical model

In this section, the CD-DEG simplified model equations are reported and specialized to the case of a small-scale CD-DEG, for which inertial and volume forces are negligible with respect to electro-elastic forces. The presented equations are employed in the rest of the deliverable to 1) fit hyperelastic parameters from dry-run CD-DEG mechanical inflation tests, 2) compute the CD-DEG capacitance from its tip height (h) measurements (which is fundamental in the post-processing of experimental data), 3) validate hydro-electro-elastic models against experimental data.

Assuming that the CD-DEG response is quasi-static, the equations describing the DEG response are the following [22]:

$$\begin{aligned}
 p &= \frac{4h}{h^2 + e^2} \frac{t_0}{\lambda^2} \sigma \\
 \lambda &= \lambda_1 = \lambda_2 = \lambda_3^{-2} = \frac{h^2 + e^2}{ee_0} \\
 \sigma &= 2a \frac{\lambda^2 - \lambda^{-4}}{I_m - 2\lambda^2 - \lambda^{-4}} - \varepsilon \lambda^4 \left(\frac{V}{t_0} \right)^2
 \end{aligned} \tag{24}$$

Where p is the air gauge pressure, h is the membrane tip displacement (positive upward), t_0 and e_0 are the undeformed membrane thickness and radius respectively, λ and σ are equibiaxial stretch and stress at the membrane tip, V is the applied voltage.

A hyperelastic Gent model [11] has been assumed here, whose constitutive parameters are respectively a and I_m . According to Gent model, the hyperelastic strain energy function, is related to the principal stretches (λ_1, λ_2 and λ_3) as follows:

$$\Psi(\lambda_1, \lambda_2, \lambda_3) = -a \log \frac{I_m - \lambda_1^2 - \lambda_2^2 - \lambda_3^2}{I_m - 3}. \quad (25)$$

As regards the capacitance of the CD-DEG, in [22] it is shown that its expression is

$$C(h) = \frac{\pi \varepsilon e^2}{3t} \left[\left(\frac{h^2 + e^2}{e^2} \right)^3 + \left(\frac{h^2 + e^2}{e^2} \right)^2 + \left(\frac{h^2 + e^2}{e^2} \right) \right], \quad (26)$$

where $t = t_0 \lambda_p^{-2}$ is the membrane thickness in the flat configuration, and $\lambda_p = e/e_0$ is the pre-stretch.

It is worth remembering that equations (24)-(26) hold under the assumption that the CD-DEG deformation is prevalently equibiaxial and the deformed shape is a spherical shell [22], i.e., the air volume subtended by the membrane is function of h as follows:

$$\Omega_a = \frac{\pi}{6} h (h^2 + 3e^2). \quad (27)$$

3.3 Materials characterization

In this section we compare the mechanical (pressure-tip elevation) response of three CD-DEGs made by different DE materials using the setup that has been previously described. In particular, three different elastomers have been considered: acrylic VHB-4905 (by 3M), TheraBand synthetic rubber [23], and Elastosil Silicone (by Wacker). The first two materials are a pressure-sensitive tape and a physiotherapy elastic band respectively, while the third material is specifically conceived and produced for DEGs application.

Three different CD-DEG samples were built using the reference materials. Their features (pre-stretch, λ_p , and thicknesses t_0 and t in the undeformed and flat pre-stretched configurations respectively) are described in Table 4. During tests, the samples were subjected to cyclic inflation tests by compressing/decompressing air through prescribed piston motion. Pressure was measured via a pressure sensor (MPX12 by Freescale Semiconductor) and the displacement of the membrane tip was measured with the laser sensor (LK-G152 by Keyence).

The plots of the stabilized tip displacement-pressure curves are represented in black in Figure 10.

The plots show that:

- although the second and third samples are less-stretched and have a smaller volume ($\Omega = \pi e^2 t$), they require larger pressures to be deformed, as they are based on stiffer materials;
- the acrylic elastomer is visibly more hysteretic than the other two materials, which present relatively low hysteresis.

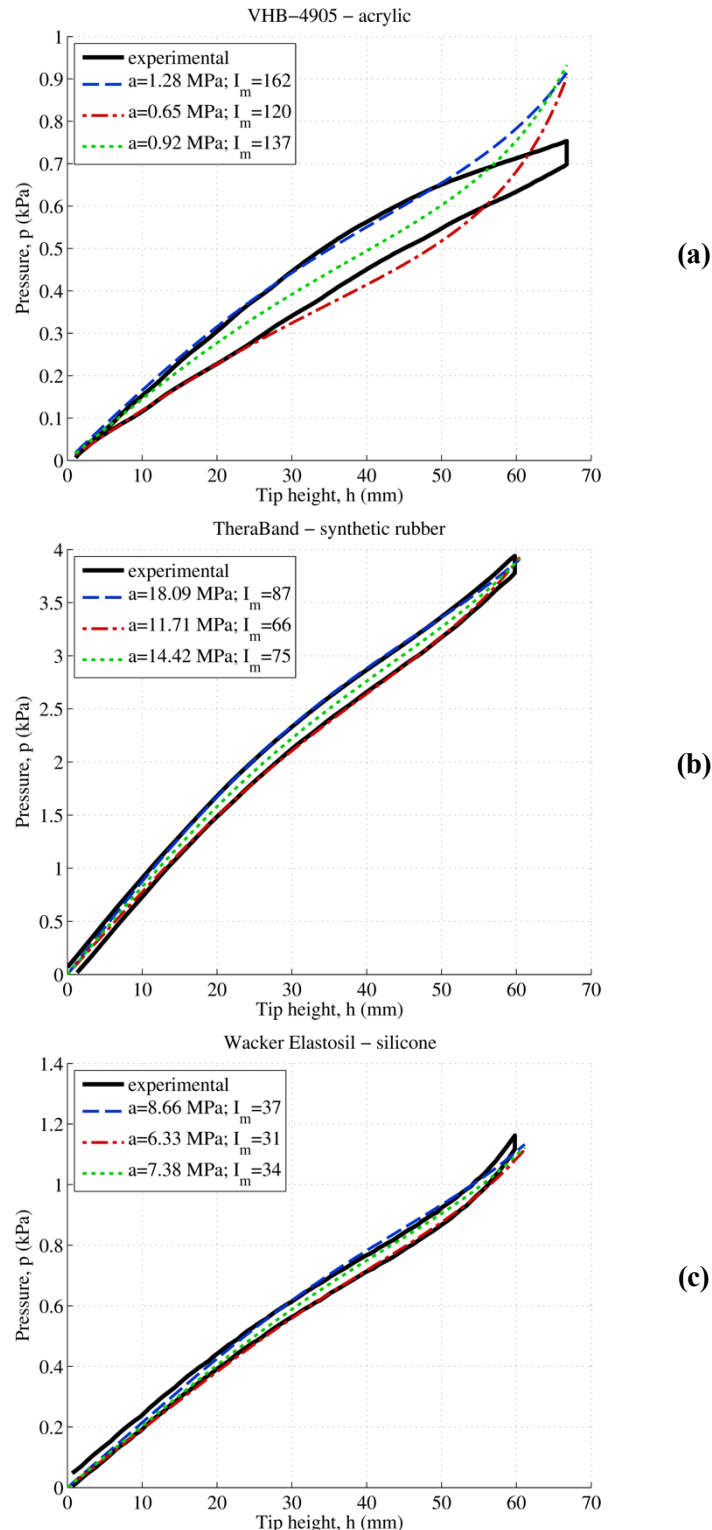


Figure 10 - Dry-run experimental pressure-tip displacement curves (black) for three CD-DEG samples, made of (a) VHB-4905 acrylic, (b) TheraBand rubber, and (c) Wacker Elastosil silicone respectively. Fitting curves of the inflation, deflation and mean response (in blue, red and green respectively) using a Gent hyperelastic model.

Experimental data have been fitted using the mechanical model of CD-DEG described in Sect. 3.2, and considering the constitutive parameters a and I_m as unknowns in the fitting procedure.

For each material, three different fittings have been performed, using the expansion, deflation and mean curves respectively. Moreover, as the CD-DEG model detailed in [22] is valid only for relatively small values of h , only the data relative to $h < 55\text{mm}$ have been used for the fitting. Results from fittings and the corresponding values of the hyperelastic parameters are represented by dashed lines in Figure 10.

Table 4 – Features of the three CD-DEG samples.

# ID	Material	<i>e</i> (mm)	λ_p	<i>t₀</i> (mm)	<i>t</i> (mm)
1	VHB-4905 acrylic	65	3	1.0	0.11
2	TheraBand rubber	65	2	0.21	0.053
3	Elastosil silicone	65	1.4	0.05	0.026

A way to compare the stiffness of the three materials is by introducing the so-called shear modulus, μ , which, assuming the hyperelastic form of equation (25), is defined as

$$\mu = \frac{2a}{I_m - 3}. \quad (28)$$

Using the parameters fitted from the mean mechanical response (green dotted lines in Figure 10) of the three materials, the shear moduli of Table 5.a are obtained, from which we can see that synthetic rubber and Elastosil silicone are approximately 20 times stiffer than VHB acrylic.

The material mechanical stiffness has an important role as it sets the DE-PTO stiffness affecting the Poly-OWC dynamics. In the following, we propose a procedure that makes it possible to determine the CD-DEG thickness required to reach a target stiffness with a given material and given pre-stretch.

Table 5 – (a) Shear moduli of the reference materials. (b) Comparative estimate of required thickness (*t₀*) and material volume (Ω) required to provide a CD-DEG whose mechanical stiffness is almost equal to the hydrostatic stiffness of a reference small-scale OWC prototype with collector radius $e=0.1m$.

Material	μ (kPa)	Material	<i>t₀</i> (mm)	Ω (cm ³)
VHB-4905 acrylic	16	VHB-4905 acrylic	1.2	4.2
TheraBand rubber	371	TheraBand rubber	0.08	2.0
Elastosil silicone	452	Elastosil silicone	0.06	1.4

(a)

(b)

Let us consider a Poly-OWC equipped with a CD-DEG with radius e (in the flat pre-stretched configuration). Let us also suppose, for simplicity, that the OWC collector has cylindrical shape with equal inner radius, e . From the OWC free surface dynamic equation (see [2] or [24]), it is known that the membrane average stiffness (considering its mechanical response only, in absence of electric charge) is given by

$$k_m = \pi e^2 \left\langle \frac{dp}{dz} \right\rangle, \quad (29)$$

where z is the free surface displacement from the equilibrium position, and the symbol $\langle \bullet \rangle$ indicates an average over the DEG working range. This stiffness compares with the hydrostatic stiffness, i.e.:

$$k_h = \pi e^2 \rho_w g, \quad (30)$$

with ρ_w being the sea water density.

The membrane stiffness sums to the hydrostatic stiffness, thus setting the overall equivalent stiffness of the Poly-OWC.

If we consider a retro-fit of an existing OWC architecture with a DEG PTO, we should require that the membrane stiffness is small with respect to k_h , or, at least it has the same order of magnitude (otherwise the system would be excessively stiff and would undergo water column motions with excessively small amplitude).

In the following, we consider a CD-DEG which is flat ($h=0$) in the reference equilibrium configuration (i.e., when $z=0$), and we consider a deformation from $h=0$ to $h=e$. We approximate the mean membrane stiffness

as $k_m \approx \pi e^2 (\Delta p / \Delta z)$, where Δp and Δz are the gauge pressure and free surface position variation in correspondence of the considered membrane deformation.

Since we want to compute the CD-DEG mechanical stiffness without including the effect of the interposed air volume stiffness, we assume that air is incompressible, and from equation (27) we find that $\Delta z = 2e/3$. Furthermore, by algebraic rearrangement of equations (24), Δp can be obtained. It can be easily shown that

$$\frac{\Delta p}{\Delta z} = \frac{3at_0}{2\lambda_p^2 e^2} \frac{4\lambda_p^2 - (2\lambda_p)^{-4}}{I_m - 8\lambda_p^2 - (2\lambda_p)^{-4}} \quad (31)$$

In the tests described in this deliverable, we consider prototypes with scale in the range of 1:50 and 1:40. Making reference to existing OWC architectures (e.g., Pico [3] or Sendekia [26] OWCs), which have cross-section collector dimensions in the order of 10m, a reasonable estimate for the small-scale collector radius is $e=0.1\text{m}$. Using this value and the mean hyperelastic parameters obtained so far, by imposing that $k_m \approx k_p$, it is possible to obtain an estimate of the required CD-DEG undeformed thickness for the three considered materials. Results in Table 5.b show the required small-scale CD-DEG PTO thickness and the resulting DE volume. In the calculation, it was assumed that VHB membrane had a pre-stretch $\lambda_p=3$, because it is quite soft and viscoelastic and it would buckle/wrinkle if not sufficiently pre-stretched; for the other two elastomers, which are much stiffer, $\lambda_p=1.1$ was assumed.

Required undeformed thickness is in the order of 1mm for VHB (which is technically implementable, as VHB is commercially sold in layers of 0.5mm thickness), and of some tens of μm for TheraBand and Elastosil. TheraBand rubber is produced in sheets with minimum thickness of $200\div250\mu\text{m}$, so it is not suitable for 1:50 scale prototypes. As regards Elastosil silicone, a target thickness of $60\mu\text{m}$ can be set up, as commercial films have thickness down to $20\mu\text{m}$, however:

- manual handling of very thin (micrometric) layers is very complicated, and may lead to non-repeatable samples manufacturing;
- the resulting DE volume would be quite small compared to that of the VHB sample (see Table 5.b), therefore the DEG would be able to convert a lower amount of energy per cycle (mechanical-to-electrical cyclic converted energy is proportional to Ω , see e.g. equation (6)).

VHB acrylic, on the other hand, is easy to handle, pre-stretch and stack in layers (thanks to its adhesiveness), and it results by far the best option for small scale experiments.

Notice that:

- it was assumed here that the OWC collector has the same radius of the CD-DEG. If a smaller CD-DEG radius was taken, resulting thickness would have been even smaller, thus employment of TheraBand/Wacker would have been even more critic.
- If a larger pre-stretch was assumed for natural rubber and silicone, the required thickness would have been lower as well.

In conclusion, it appears that, among commercial materials, VHB acrylic tape is the most suitable to be employed as DE in small-scale (1:50) tank tests of Poly-OWC systems. This material (which is not optimized for DE applications) is however quite dissipative: it exhibits significant mechanical hysteresis and non negligible electrical conductivity. Owing to its limited electro-mechanical conversion efficiency, the use of acrylic VHB is thus envisaged only for small scale prototypes implementation.

Since the stiffness of CD-DEGs with increasing radius e decreases by a factor e^{-2} (see equation (31)), the use of stiffer materials (like the considered natural rubber by Theraband and silicone elastomers by Wacker) are likely to be a preferred choice for larger scale prototypes since they would provide higher electromechanical conversion efficiency.

3.4 Generation tests

In this subsection, we report dry-run generation results obtained by testing DEG samples made of different materials (namely, VHB-4905 and synthetic rubber). Tests were run on the machine described in Sect. 3.1. The polymeric samples were painted only on a small circular area above the membrane center in order to obtain nearly-equibiaxial DEG expansion/contraction (indeed, the deformation at the tip of inflating

membranes is equibiaxial). Equibiaxial deformation of a DE membrane in the plane of the electrodes provides the largest capacitance variations, thus allowing to measure the largest values for the converted energy per cycle per unit volume of DE material.

Samples are prepared by pre-stretching polymeric membranes (with pre-stretch λ_p) on a circular frame and fastening them to the setup of Figure 8. Electrodes are painted on both sides of the membrane using a conductive carbon grease (MG-Chemicals 846). The membrane overall radius in the pre-stretched flat configuration is $e=65\text{mm}$, while the electrodes diameter (in the flat configuration) is indicated as e_{el} and is different for each sample.

The electronic circuit employed in the tests is depicted in Figure 11. With reference to the figure, C_{DEG} indicates the DE sample variable capacitance, C_c is an in-parallel capacitance with the dual scope of measuring the amount of charge supplied to the DEG during the charging phase and limiting the voltage raise on the DEG during the generation phase (in order to prevent electrical breakdown); S_1 , S_2 and S_3 are HV switches.

Generation cycles are performed following these steps:

- While S_1 is closed and the other two switches are open, capacitor C_c is charged up to a voltage V_c by the power supply. Meanwhile, the DEG is inflated up to a known and prescribed configuration, and its capacitance rises.
- As the DEG reaches its maximum capacitance, S_1 is opened, S_2 is closed and the two capacitances reach an equilibrium at a voltage V_A such that

$$(C_{DEG,A} + C_c)V_A = C_cV_c, \quad (32)$$

where $C_{DEG,A}$ is the DEG capacitance in an equilibrium condition at voltage V_A .

- While the DEG capacitance decreases, C_c and the DEG are kept connected in parallel, and the overall charge on their electrodes is constant, as both S_1 and S_3 are open.
- When the DEG returns to the flat configuration, its capacitance reaches a minimum (there, the corresponding voltage on the DEG and on C_c is indicated by V_B), S_3 is closed, the DEG is discharged over the power supply and the cycle is restarted.

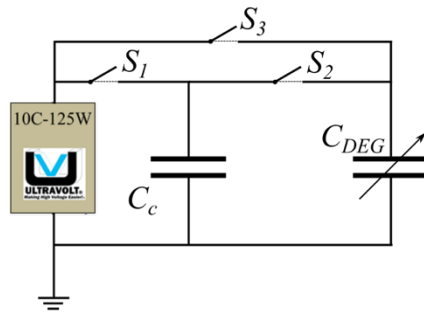


Figure 11 – Electric circuit for dry-run generation tests

During the whole generation phase, the voltage over both C_c and the DEG is measured by means of a HV probe with high impedance, and the membrane tip displacement is measured with a CCD laser sensor. Based on the measured variables, the electric energy harvested in a cycle is computed as follows:

$$E_{hc} = \int_0^{V_B} V d(C_{DEG}V) - \int_0^{V_A} V d(C_{DEG}V) + \frac{1}{2} C_c (V_B^2 - V_A^2) \quad (33)$$

where V is the instant voltage on the CD-DEG. In equation (33), the first and second integrals represent the amount of energy respectively generated and spent during the discharging and charging phase of the DEG, while the third addendum is the amount of energy which is generated during the activation phase, in which the DEG capacitance decreases and the overall charge on the parallel of the two capacitances is constant.

Notice that C_{DEG} varies both during the DEG charging and discharging phase. Charging and discharging of the DEG can be approximated by nearly instantaneous processes, which take place while the DE membrane is in known configurations, respectively inflated by a prescribed amount, and flat on the horizontal plane.

During these phases, a sudden (nearly instantaneous) variation in the partially painted electrodes surface occurs, due to the variations in Maxwell stress induced by the varying electric field within the dielectric material. That is, when the DEG is instantly charged, its electrodes undergo a sudden expansion, due to the instant arise of an electric field within the DE layer. Vice versa, when the DEG is discharged, the sudden drop of the electric field provokes the electrodes surface to reduce. These effects are schematically depicted in Figure 12.a and Figure 12.b respectively.

Although charging and discharging are instantaneous, it can be assumed that the above mentioned deformations (also described in Figure 12.a and b) are constituted by a succession of equilibrium states, i.e., in any intermediate configuration, the active portion of the membrane is in a condition of force equilibrium with the surrounding (non active) polymeric volume. On a charge-voltage plane, the equilibrium states during charging/discharging phases can be represented by two curves (one for each phase), as in Figure 12.c.

For any intermediate voltage applied on the DEG in correspondence of the two extreme configurations (inflated and flat), the corresponding equilibrium state (and the corresponding shape of the DEG electrodes) can be found using the following assumptions.

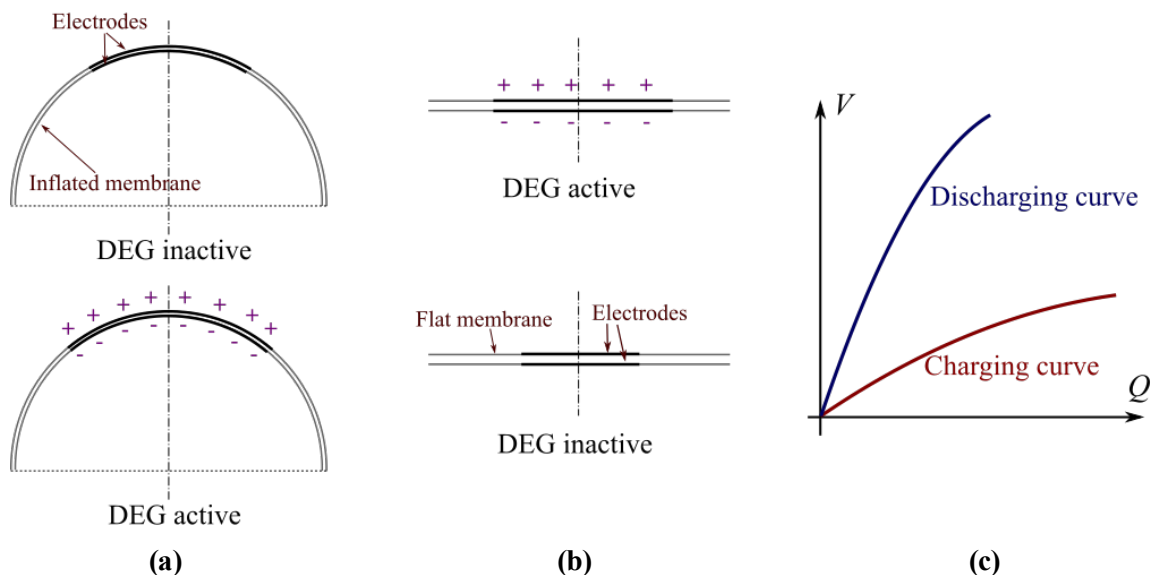


Figure 12 – (a) When the membrane is in a known inflated configuration, the DEG is activated and electrodes expand; **(b)** When the membrane is flat, DEG is discharged, and electrodes surface diminishes; **(c)** Charge-Voltage curves representing the intermediate equilibrium states of the DEG during charging/discharging phases.

The active portion of the membrane (i.e., the DEG) can be assumed to be uniformly subjected to an equibiaxial deformation, which depends on the stress applied on its perimeter. On the other hand, the remaining (inactive) portion of membrane, having much larger volume than the active part, is barely affected by the electrodes deformation, so the stress applied on the DEG electrodes perimeter can be assumed to be constant during charging/discharging. Therefore, indicating with λ_i the stretch on the electrodes in absence of electrical activation, and λ_a the electrodes stretch at a generic voltage, V , the relationship between the two stretches is given by

$$\sigma(\lambda_i) = \sigma(\lambda_a) - \frac{\varepsilon \lambda_a^4 V^2}{t_0^2} \quad (34)$$

where the stress-stretch relation, $\sigma(\lambda)$, in the hypothesis of a Gent hyperelastic model (see equation (25)) and uniform equibiaxial deformation, is given by

$$\sigma = 2a \frac{\lambda^2 - \lambda^{-4}}{I_m - 2\lambda^2 - \lambda^{-4}}. \quad (35)$$

Notice that

- λ_i is different for the case in which the membrane is flat and that in which it is inflated to the activation configuration. In particular, when the membrane is flat (discharging phase), $\lambda_i = \lambda_p$, where the second term is the membrane pre-stretch. When the membrane is inflated to the maximum configuration (and its tip height is h), λ_i is given by equation (24).
- λ_a is a function of voltage.
- By solving equation (34), it is possible to find $\lambda_a(V)$, from which the curves of Figure 12.c can be constructed.

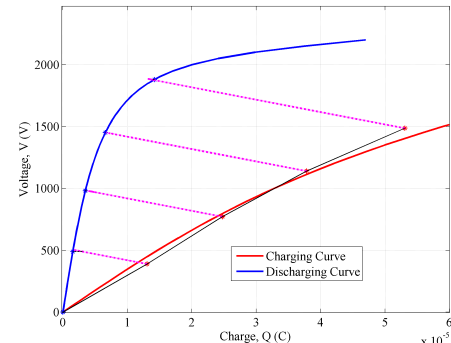
In the following, we report generation tests results on two different materials samples. In each case, activation and discharging curves are computed according to the mentioned procedure. The voltage over the DEG is measured during the whole duration of the test. The charge on the DEG at the end of the charging cycle and during the activation phase is computed, for a cross-check, by measuring the voltage drop on the charging capacitor, C_c and using equation (32). Generated energy is calculated accordingly using equation (33).

3.4.1 Generation tests with VHB-4905

The features of the tested samples are reported in Figure 13.a. Different generation cycles were performed, with different feeding voltage V_{in} . Energy conversion cycles for the reference sample are depicted in Figure 13.b, while the net generated electric energy density, E_{hc}/Ω for the different cycles, is Figure 13.a.

Thickness, t_0	0.5 mm
Polymer volume, Ω	182 mm ³
Pre-stretch, λ_p	3.25
Electrodes diameter (flat config.), e_{el}	35 mm
In-parallel capacitance, C_c	100 nF
Cyclic generated energy density, E_{hc}/Ω (kJ/kg)	
Cycle 1	0.01
Cycle 2	0.05
Cycle 3	0.10
Cycle 4	0.13

(a)



(b)

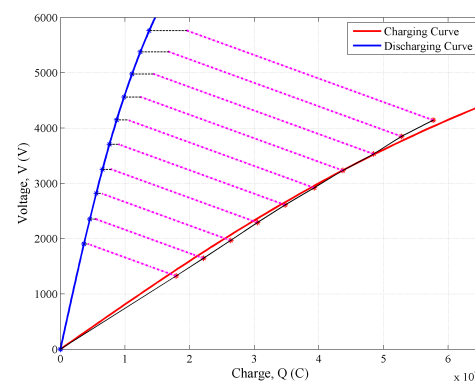
Figure 13 – (a) VHB-4905 sample features and generated energy density; (b) Energy conversion cycles on a charge-voltage plane

3.4.2 Generation tests with Theraband synthetic rubber

The features of the tested samples are reported in Figure 14.a. Different generation cycles were performed, with different feeding voltage V_{in} . Energy conversion cycles for the reference sample are depicted in Figure 14.b, while the net generated electric energy density, E_{hc}/Ω for the different cycles, is Figure 14.a.

Thickness, t_0	0.26 mm
Polymer volume, Ω	189 mm ³
Pre-stretch, λ_p	2.3
Electrodes diameter (flat config.), e_{el}	35 mm
In-parallel capacitance, C_c	23.5 nF
Cyclic generated energy density, E_{hc}/Ω (kJ/kg)	
Cycle 1	0.07
Cycle 2	0.11
Cycle 3	0.16
Cycle 4	0.20
Cycle 5	0.27
Cycle 6	0.33
Cycle 7	0.39
Cycle 8	0.46
Cycle 9	0.52
Cycle 10	0.58

(a)



(b)

Figure 14 – (a) Theraband rubber sample features and generated energy density; (b) Energy conversion cycles on a charge-voltage plane

Although in the described experiments the maximum voltage on the DEG electrodes has been kept well below physically admitted value (i.e., breakdown limit), in order to prevent charge leakage through air (no

protection layer was indeed present on the HV electrode), it has been shown that good energy densities (up to 0.6 kJ/kg) can be obtained by properly selecting the DE material for the application. Even larger values of the converted energy can be obtained using larger activation voltages. Roughly, the amount of energy converted in a cycle has a quadratic dependence on V_{in} .

Larger energy densities have been measured on the Theraband rubber with respect to the VHB acrylic. This is mainly due to the largest applied voltages. Being VHB-4905 very viscoelastic and compliant, applied voltage has to be limited in order to prevent loss of tension and buckling. That is, although VHB-4905 is an easy-to-handle material, and it is particularly suitable for experiments on small-scale PolyWECs (as shown in Sect. 3.3), in a future perspective of large-scale employment, other materials should be considered, in order to obtain larger efficiency, better repeatability and enhanced performance.

3.5 Hardware-in-Loop tests

In this section, we report results of Hardware-in-Loop (HIL) experiments, aimed at performing a preliminary assessment of the control capability of the CD-DEG PTO, even in presence of irregular waves. In this kind of tests, the physical setup described in Sect. 3.1 and shown in Figure 8 is coupled with a software model of a small-scale OWC hydrodynamics.

The experimental setup relies on 1) a hardware custom-made pneumatic cylinder housing a rigid piston and a small scale fully functional CD-DEG prototype; 2) software controls which emulate (in simulation) the free surface dynamics of a scaled OWC with given geometry; 3) drivers, electronics, sensors and a linear motor which enable the connection of the hardware and software sub-systems.

In the experiments, the software hydrodynamics model solves in real time the OWC dynamics equation of motion, thus providing an output that is used to command the motion of the hardware piston. The control loop is closed feeding back the actual value of the pressure in the cylinder to the hydrodynamic model, as shown in the scheme of Figure 15.

In principle, the test-bench can be used to test different Poly-OWC concepts and to study different control algorithms for their PTO.

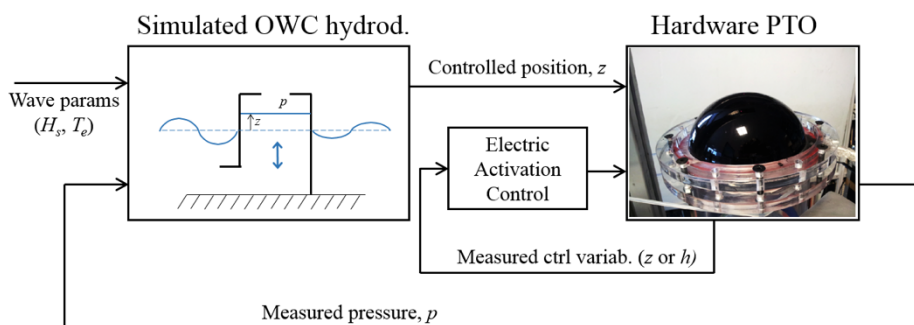


Figure 15 – Block diagram of HIL simulations

In the following, we report results of preliminary experiments that aim at simulating an offshore OWC tubular collector with a patented shape proposed by the Spanish company Sendekia. The hydrodynamic model of the collector has been modelled using the hydrodynamic data employed in paper [24], properly scale by a scale factor $f_s=1/75$. The modelled hydrodynamic has been coupled with a physical prototype of CD-DEG made of acrylic VHB-4905 elastomer.

3.5.1 CD-DEG sample

In order to match the diameter of the OWC collector with that of the hardware cylinder tube, a small-scale OWC prototype (with geometric scale factor of 1:75) has been considered for the computation of the hydrodynamic parameters.

The employed CD-DEG specimen is made by an active dielectric elastomer membrane, which is obtained by gluing together two layers of a VHB-4905, that is stretched onto a polycarbonate ring and coated on both sides with compliant carbon conductive grease electrodes (MG-Chemicals 846). The dimension of the internal diameter of the polycarbonate ring is $e = 130\text{mm}$; acrylic film pre-stretch is equi-biaxial with value

$\lambda_p = 3$; the initial thickness (in the undeformed condition) of the active dielectric elastomer membrane is $t_0 = 1.0\text{mm}$, which excludes the thickness of the compliant electrodes. A picture of the CD-DEG prototype that has been employed for this study is reported in Figure 16.a.

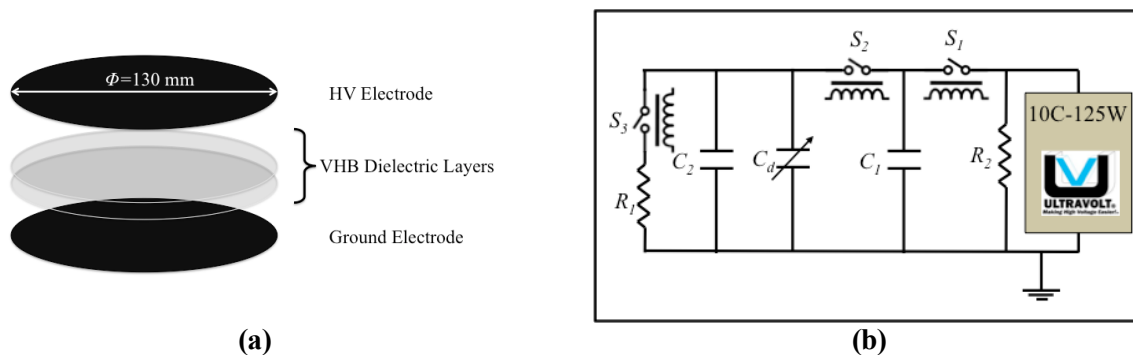


Figure 16 – (a) Schematic of the CD-DEG assembly; (b) Simplified schematic of the HV Driving circuit.

3.5.2 HV circuit

A custom made HV driving electronics has been developed to control CD-DEG charge and discharge. As depicted in Figure 16.b, the considered driving electronics comprises a HV power supply (10C24-P125 by UltraVolt), three HV reed relays (HM12-1A69-150 by MEDER electronic) and two supplementary HV capacitors.

In Figure 16.b, C_2 is a capacitor that is permanently connected in parallel with the CD-DEG (whose variable capacitance is indicated in the figure as C_d). The capacitor C_2 is introduced to absorb and store part of the charge, i.e. limiting the rise of voltage, during the generation phase of the harvesting cycles. The capacitor C_1 is large in value and is employed to deliver the charge to the CD-DEG (and to C_2). Specifically, the charging of the CD-DEG (and of C_2) takes place when the relay S_2 is closed (with S_1 being opened at the same time).

In the circuit, resistor R_2 ($R_2 = 20\text{M}\Omega$) is used to provide a resistive component to the load of the power supply, whereas resistor R_1 ($R_1 = 1\text{M}\Omega$) is used to limit the peak current that occurs during CD-DEG discharge as the relay S_3 is closed.

To measure the electric potential difference, V_d , between CD-DEG electrodes, a custom made HV probe (not depicted in Figure 16.b) has been implemented that features very high input resistance (nearly $50\text{G}\Omega$), which drastically limits the drain of charge from the CD-DEG electrodes, and large bandwidth, which is obtained thanks to a capacitor compensation network. In order to minimize the current leakage of the power electronics, all the HV wirings and components have been encapsulated via thick layers of silicone gel (Magic gel by Raytech) and acrylic tape (VHB 4905 by 3M®). A second identical HV probe is employed to measure the voltage V_1 across the capacitor C_1 . This voltage reading during the charging phase of the CD-DEG (and of C_2) makes it possible to precisely evaluate the initial value of C_d .

3.5.3 Controller implementation

A MatLab® xPC Target® real-time machine (Performance real-time target machine by SpeedGoat®) is employed to run the real-time hydrodynamic model of the OWC plant, which governs the motion of the piston, and to control the charging status (charging voltage and status of relays) of the CD-DEG.

The developed test-bench, with its sensing equipment, makes it possible to implement different algorithms for controlling the harvesting cycles of the CD-DEG. A first simple regulation strategy consists in imposing a state of electrical activation to the CD-DEG that is only a function of the actual value of its capacitance. Such a value can be directly measured or can be estimated through at least one of the following sensor readings: air-chamber pressure, position of the piston, displacement of the tip of the CD-DEG. In more advanced versions of the CD-DEG control, the acquired measures can also be employed to build suitable estimators that can further improve the energy harvesting performance of the generator.

Results described here have been collected implementing a control law that triggers the activation status of the CD-DEG on the basis of the knowledge of the water column level z inside the chamber. Specifically, the CD-DEG is charged when z reaches a maximum (or minimum) and it is discharged when z crosses the zero.

3.5.4 Results

This section reports preliminary tests that have been conducted considering the hydrodynamic model of a floating Poly-OWC based on the OWC collector developed by the company Sendekia. Details of the hydrodynamic model and on the dimensioning of this WEC are reported in [24].

Figure 17 reports the experimental results acquired during three tests of the same CD-DEG subjected to different activation voltages and excited by the same emulated set of polychromatic incident waves, generated using a Bretschneider spectrum with the following parameters: $H_s = 4.55\text{cm}$ and $T_e = 0.91\text{s}$ that, at full scale, correspond to $H_s = 3.4\text{m}$ and $T_e = 7.9\text{s}$ according to the rules of Froude scaling. The plots reported in figure are for the different variables that are measured with the set-up: the voltage (V_1) across capacitor C_1 ; the voltage (V_d) across the CD-DEG (and C_2); the differential pressure (p) with respect to atmosphere inside the cylinder (that emulates the pressure inside the OWC air-chamber); the position (z) of the piston (that emulates the free surface of the column of water inside the OWC). In each plot, the results of the three tests performed with different activation voltages are represented by red and blue solid lines.

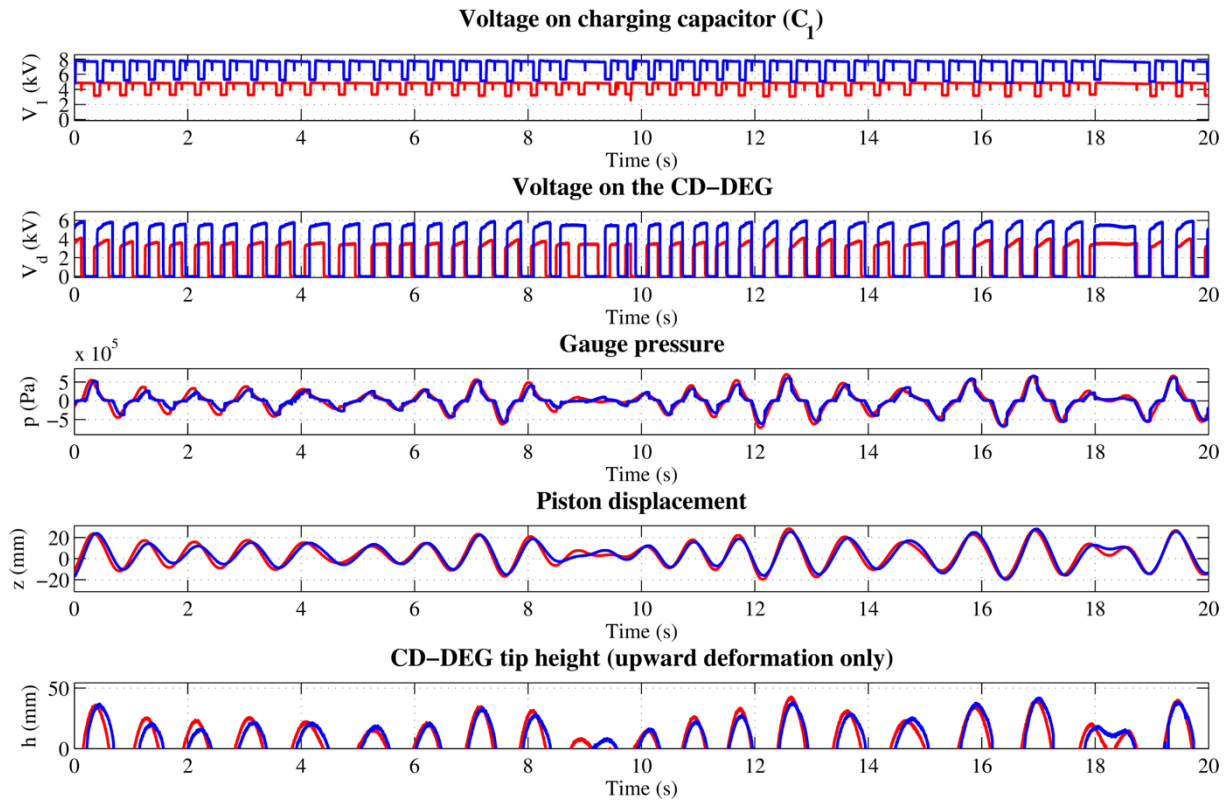


Figure 17 - Example of the measured variables time-series during experiments with simulated polychromatic waves ($H_s = 4.5\text{cm}$, $T_e = 0.91\text{s}$). Data are plotted for the same incident wave and two different values of the supply voltage on the charging capacitor.

The reported results highlight the following:

- In all wave periods and for all the two test cases, upon electrical activation, voltage V_d increases as the CD-DEG deflates. That is, irrespective of wave height and period and of the value chosen for the activation voltage, the considered control law based on the measurement of the water level inside the OWC structure is effective and makes it possible to convert pneumatic energy into electricity via the CD-DEG.
- Activation of the CD-DEG determines a drop in pressure inside the cylinder chamber, with the drop being larger as the activation voltage is higher. This pressure drop indicates that the mechanical work absorbed by the piston to deflate the CD-DEG is lower than that provided during

the inflation phase, with the difference being the electrical energy that is extracted by the CD-DEG (plus the losses that are due to material viscoelasticity). As a consequence, the energy that can be harvested by the CD-DEG is larger as the activation voltage is higher.

- The motion amplitude of the piston diminishes as the activation voltage of the CD-DEG is increased. This indicates that the energy extraction performed by the CD-DEG can significantly affect the dynamics of the water inside the OWC structure. This demonstrates that the CD-DEG can extract a significant portion of the energy that is available in the incident water waves.

4 WAVE-TANK TESTING: FACILITIES AT EDINBURGH UNIVERSITY

In this section, the testing facilities available at UEDIN are described, which have been exploited to perform the wet-run tests detailed in this report.

To date, two facilities have been involved in PolyWEC tests: 1) the Wave Flume, which has been employed to perform tests on the first two prototypes of fixed-structure OWC; 2) the FloWave, which has been employed for the tests on a floating OWC.

4.1 Wave-flume

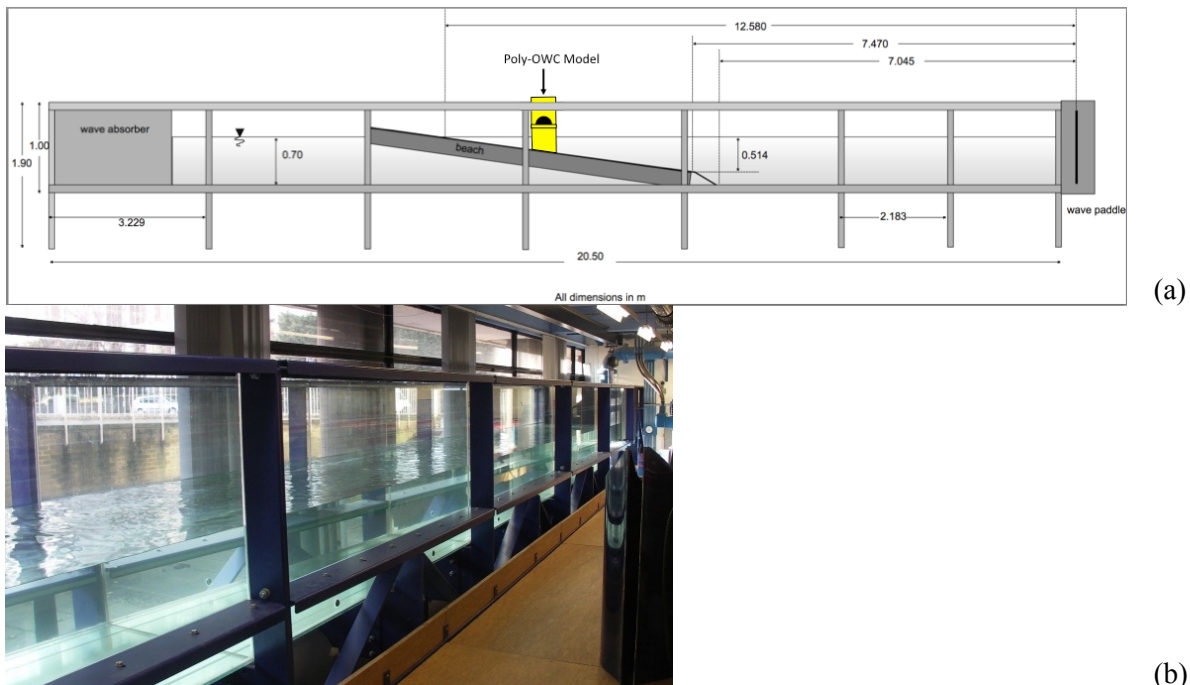


Figure 18 – (a) Schematic drawing of the wave-flume setup, with a Poly-OWC prototype installed as in the experiments described in Sect. 5 and 6.; **(b)** Photograph of the wave-flume facility.

The wave-flume (or wave-channel) is a particular kind of wave-tank, having its length much larger than its width (see Figure 18) and being specifically designed to carry out two-dimensional hydrodynamic tests on small-scale physical models. The considered flume is 20m in length, 0.4m in width, and features a water depth of 0.7m. A computer-controlled, active-absorption, oscillating paddle wave-maker is located at one end of the tank. This wave-maker can accurately generate both regular and irregular waves. For regular waves, wave heights H of up to 0.1m can be generated for wave frequencies f between 0.6Hz and 1.2Hz, and up to $H = 0.07\text{m}$ for f between 1.2Hz and 1.6Hz. A passive wave absorbing beach, which is made up of two upright triangular pieces of foam, is located at the other end of the tank. Two sets of experiments on fixed structure Poly-OWCs were carried out in the wave-flume (see Sect. 5 and 6). In both cases, a 1:20 sloping beach, made of plastic material and supported by steel beams, was placed in the central sections of the flume in order to simulate shallow water waves (see Figure 18.a). The Poly-OWC models were securely fixed into the flume with the bottom resting on the beach.

4.2 FloWave

FloWave is a circular 5m-deep tank with a diameter of 25m, with a capacity of 2.4 Ml, and it is circumferentially ringed by 168 absorbing wave makers. A photograph of FloWave is shown in Figure 19. This facility is conceived to reproduce sea waves and currents with a scale factor up to 1:20. In particular, the tank is optimized for 700mm-high two-second waves.

Thanks to circular symmetry, waves and currents in the FloWave can act in any combination and in any relative direction across the large central volume (which is 17m in diameter and 2m deep). Therefore, the facility allows to generate full-spectrum multi-directional waves as well as monochromatic waves. Details on design and construction of FloWave are resumed in [25].

In the framework of PolyWEC, one experimental campaign has been conducted in the FloWave, on a floating OWC prototype moored to the tank bottom by means of tension legs.



Figure 19 – Picture of UEDIN circular FloWave tank

5 FIXED STRUCTURE OWC – PRELIMINARY DESIGN

This section reports experimental results on a preliminary campaign of tests carried out on a fixed-structure OWC, tested in the Wave-flume facility at UEDIN. Experiments were carried out in December 2013.

As these tests were the first to be done within PolyWEC project, their aim was to assess the in-field operation of DE PTOs, define methodologies and tools to build and set-up small-scale tank models, and validate sensing and measurement devices and procedures for future tests. For this reason, attention was not addressed to the hydrodynamic optimization of the tested device; that is, the tested OWC is not resonant with incoming test waves, thus it is not fully representative of a full-scale functional device. Nonetheless, these experiments provided important feedbacks on the control capability of DE-based PTOs and on their effective ability of influencing WECs dynamics.

5.1 Experimental setup

Taking as reference full-scale Poly-OWC dimensions comparable to those of [22], the developed prototype has a scale of approximately 1:50.

The OWC model has been manufactured by assembling laser cut polycarbonate plates. The model has been designed to be tested in shallow water waves conditions with an inclined sea-bed featuring beach slopes between 1:10 and 1:20. As depicted in Figure 20, the Poly-OWC chamber has a rectangular (260mm by 285mm) cross-section and is open to the incoming wave field via a submerged rectangular (110mm by 285mm) aperture that is located at the bottom of the front-wall. The upper and lower parts of the Poly-OWC chamber are filled with air and water, respectively. The water depth measured at the Poly-OWC front-wall is 200mm; the upper air-chamber extends by 90mm from the Mean Water Level (MWL); the upper horizontal lip of the submerged rectangular aperture lies 90mm below the MWL.

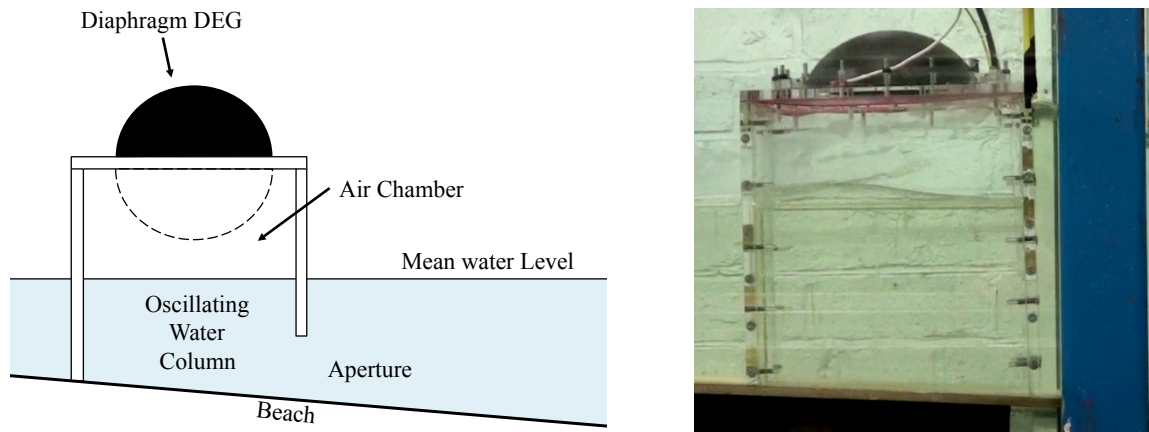


Figure 20 - Schematic of the small-scale Poly-OWC (left) and picture of the prototype during the tests (right).

Although not very efficient from a hydrodynamic point of view [26], the chosen chamber architecture and dimensions have been considered sufficient for a preliminary experimental evaluation of the Poly-OWC concept.

The top plate of the Poly-OWC features a circular hole, with radius $e = 90\text{mm}$, that houses a Circular Diaphragm DEG (CD-DEG) made with an acrylic elastomer DE membrane (VHB 4905 by 3M[®]) coated on both sides with compliant carbon conductive grease electrodes (MG-Chemicals 846). VHB has been chosen, instead of other more performant materials, because of its low stiffness. As already described in previous sections, commercial natural/synthetic rubber or silicone elastomers would have been preferable choices but they are too stiff to be employed at this small scale.

The CD-DEG is fastened to the top plate along its perimeter via a polycarbonate ring that is pressed with studs (this guarantees the air tightness of the Poly-OWC chamber). In the mounting condition, the CD-DEG is flat, with uniform thickness $t = 77\mu\text{m}$ and equi-biaxial pre-stretches $\lambda = 3.6$. Projected in full-scale accordingly to the coefficients of Table 3, the CD-DEG dimensions are $e=4.5\text{m}$ and $t=0.19\text{m}$. The power electronics, which is used to regulate the charge residing on the top of the CD-DEG electrodes, comprise a high voltage power supply (10C-125W by Ultravolt) and two high voltage reed

relays (HM12-1A69-150 by MEDER electronic) that alternatively connect the CD-DEG electrodes to either the power supply or to the ground.

With regard to measurements, a pressure sensor (MPX12 by Freescale Semiconductor) is used to monitor the pressure within the air chamber of the Poly-OWC. A custom-made high voltage probe, with 1000:1 dividing ratio and 10G Ω resistance, is used to measure the actual charging status of the CD-DEG. A high-speed camera is used to measure CD-DEG deformation and tip displacement.

With regard to energy harvesting control, wave power is extracted by the CD-DEG via cycles at constant charge [27]. Specifically, the employed energy harvesting cycle consists in the following steps: 1) instantaneously charge the CD-DEG, with a power supply voltage equaling V_{in} , when the diaphragm gets maximally expanded (that is, when the CD-DEG capacitance reaches a maximum value, C_{in}); 2) keep the charge constant as the CD-DEG returns to its flat configuration; 3) discharge the CD-DEG to ground when the CD-DEG returns to its flat configuration (that is, when the CD-DEG capacitance reaches its minimum value, C_{out} , and the electric potential difference between the CD-DEG electrodes reaches a maximum value, V_{out}); 4) keep the charge zero as the CD-DEG expands. Triggering between states 4 and 1 is obtained by monitoring the inversion of the time derivative of the pressure signal; triggering between states 2 and 3 is obtained by monitoring the inversion of the pressure signal; triggering between states 1 and 2 as well as between states 3 and 4 is obtained after a fixed time interval equaling 0.01s.

The described energy conversion cycle is graphically represented in Figure 21 using charge, Q , and voltage, V , as variables. Charging phase (1) corresponds to transformation OA' in the graph; constant charge phase (2) is represented by vertical line A'B'; discharging (3) is transformation B'O. Phase (4) is a purely mechanical transformation and is thus not visible on the Q - V plot.

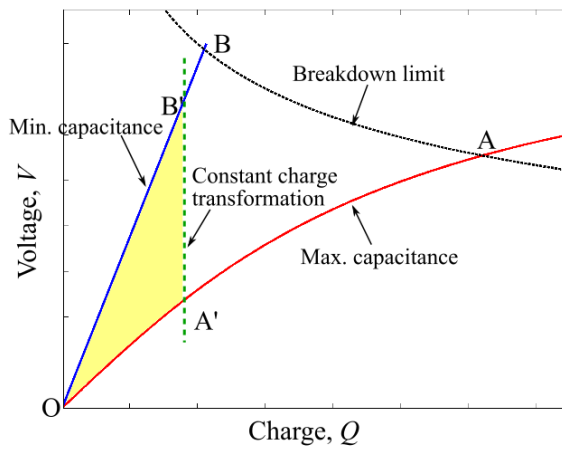


Figure 21 – Constant charge energy conversion cycle (OA'B'O) on the charge-voltage plane.

The energy harvesting controller of the Poly-OWC is implemented on a real-time machine (Performance real-time target machine by SpeedGoat) via the Matlab® xPC Target software environment.

5.2 Procedure and Data Processing

An extensive experimental campaign has been conducted in the wave-flume. During the experiments, the small-scale Poly-OWC model has been tested according to different monochromatic sea-state conditions (namely, for different f and H) and for different values of the charging voltage (V_{in}). Seven values of charging voltages have been considered: $V_{in} = [450V, 710V, 950V, 1080V, 1580V, 1770V, 2000V]$. Three values for the wave height have been considered: $H = [40mm, 60mm, 80mm]$. For each wave height, four different values of wave frequency have been considered: $f = [0.6Hz, 0.8Hz, 0.95Hz, 1.3Hz]$ for $H = 20mm$; $f = [0.6Hz, 0.8Hz, 0.95Hz, 1.2Hz]$ for $H = 60mm$; $f = [0.6Hz, 0.8Hz, 0.95Hz, 1.1Hz]$ for $H = 80mm$. The latter frequency in the sets has been reduced for increasing wave height in order to guarantee correct wave flume operation. Overall, 84 tests have been conducted on the small-scale Poly-OWC model equipped with the same CD-DEG.

For each test, the wave flume was started from a calm (fully flat) condition. To guarantee the achievement of the considered monochromatic sea-state condition, a waiting time by about two minutes

was respected prior to begin data acquisition and CD-DEG activation (i.e., energy harvesting). For simplicity, CD-DEG activation was performed only one time in a wave period; in particular during the cycle where the CD-DEG was expanding outward. For each acquisition, two-to-three wave periods with the CD-DEG inactive and eight-to-ten wave periods with the CD-DEG active were recorded. Pressure, p (namely, the relative pressure measured with respect to the atmospheric pressure, p_{atm}), and voltage, V , measurements were acquired at 1kHz; CD-DEG inflation/deflation (expansion/contraction) was captured at 100fps.

After the completion of the test campaign, all the acquired data were post-processed to obtain: the evolution of the CD-DEG tip height, h , and capacitance, C ; the energy harvested per cycle, E_{hc} , and the voltage amplification ratio, ϕ ; the conversion efficiency, η , from water column energy to electricity and the viscous loss, ζ , that is mainly due to DE material inelasticity.

The evolution in time of the CD-DEG tip height, h , is obtained from the processing, via a custom-developed software, of the images captured by the high-speed camera (further details on this procedure are in Sect. 7.2.1).

The CD-DEG capacitance is found from tip height measurements using equation (26). The dielectric constant, here is assumed equal to $\epsilon = 4.1 \times 8.81 \text{e-12 F/m}$. The validity of equation (26) has been verified (in the range of interest $|h| \leq e$) via experimental measurements performed on the inflated CD-DEG with a LCR meter (Hameg Instruments HM 8118).

Given equation (26) and the described control logic, the energy harvested per cycle is computed as

$$E_{hc} = \int_0^{V_{out}} V d(C_{out} V) - \int_0^{V_{in}} V d(C_{in} V). \quad (36)$$

where V_{in} and V_{out} are the voltages (between the electrodes of the DEG and C_a) measured at the end of the charging phase and at the beginning of the discharging phase respectively, V is the instant voltage on the DEG, C_{out} and C_{in} are CD-DEG capacitances during the discharging and charging phases respectively. Notice that, in the formulation of equation (36), it is assumed that, in general, the DEG capacitance can vary during the phases of electric charging/discharging. With reference to Figure 21, it is shown that in these experiments the DEG capacitance varies during the charging phase only. If the capacitance was constant during the charging phase, transformation OA' would be represented by a straight line through the origin of the Q - V plane. As a matter of fact, while the DEG is charged (which happens when it approaches the flat configuration) it tends to slightly further expand (because of Maxwell's stress induced softening). When the DEG is discharged, on the contrary, it does not vary its shape as it already is in its flat configuration. However, this phenomenon is numerically negligible in the range of employed cycles for the purpose of the performance estimation, thus a constant capacitance has been assumed for the estimation of the figures of merit.

The voltage ratio is computed as

$$\phi = V_{out} / V_{in}. \quad (37)$$

Given equation (36), the conversion efficiency from (water column) piston mechanical energy to electricity is calculated as

$$\eta = E_{hc} / E_m, \text{ with } E_m = \int_{T_1}^{T_2} W dt, \quad (38)$$

where T_1 and T_2 are two consecutive time instants during the CD-DEG outward expansion, where the piston power, W , turns from negative to positive and from positive to negative, respectively. The water free surface mechanical power reads as

$$W = p \dot{v}, \quad (39)$$

where, v is the volume of the parallelepiped portion of the Poly-OWC air-chamber (and \dot{v} its time derivative); namely,

$$v = v_0 \left(\frac{p_{atm}}{p_{atm} + p} \right)^{1/k} - \frac{\pi h}{6} (3e^2 + h^2), \quad k = 1.4, \quad (40)$$

where the initial air volume is $v_0 = 6.67 \text{ dm}^3$.

It is worth to be remarked that, as regards the definition of the efficiency, η , it only expresses the percentage of mechanical work made by the water column on the surrounding air (during the CD-DEG expansion phase only) which is effectively turned into electrical energy. The complementary percentage is partly dissipated by visco-elasticity (see the definition of ζ) and partly returns to water during the deflation phase of the CD-DEG.

Therefore, this efficiency 1) neglects both the hydrodynamic losses that occur in passing the energy from the outer wave field to the inner oscillating water column and the electric losses that occur in passing the harvested energy from the CD-DEG electrodes to the external energy storage, 2) does not have the meaning of a capture factor.

Viscous losses are calculated making reference to the initial cycles in which the CD-DEG is not electrically activated. That is, it is assumed that the energy dissipated by viscoelasticity is the same in the cycles with and without electric activation. This is a rough approximation that holds only if the oscillation amplitude of the two sets of cycles (with and without activation) is approximately the same, and it does not keep into account the variation in hysteresis induced by Maxwell stresses. With this assumption, the viscous loss is given by

$$\zeta = 0.5 E_d / E_m, \text{ with } E_d = \int_{T_{out}}^{T_{out}+1/f} W dt, \quad (41)$$

where T_{out} is a time instant before the first activation of the CD-DEG.

Worth to be remarked: 1) the calculation of v assumes that the inflation/deflation of the CD-DEG is an adiabatic process; 2) the calculation of conversion efficiency is performed by considering only the half cycle (in a wave period) in which the CD-DEG is expanded outward.

This bring to an underestimation of the power out since the CD-DEG could be activated also in the half cycle in which it is expanded inward.

Data processing

In order to estimate the above mentioned indices (equations 36-41), it was necessary to estimate the capacitance C of the DEG. This has been done by introducing in equation (26) the instantaneous value of $h(t)$ (note the relation of equation (26) has been preliminarily validated at the beginning of the tests against the measurements of an LCR meter in an appropriate range of tip heights).

To this aim, acquired data from the camera were post-processed to obtain tip height, $h(t)$, via a custom-developed software.

The elaboration of images is achieved through a calibration procedure to determine: the video scaling factor to transform the measured height in pixel to height in mm and the horizontal baseline of the membrane (the position of the membrane in the flat configuration).

Figure 22.b shows the two images necessary to the calibration procedure. For the calibration, two images were used: the first one shows a chessboard far from the camera and the second one shows a chessboard close to the camera. The distance between the chessboard in the two images is known and equal to R . Using the width dimensions in pixel (W_1 and W_2) of the two green rectangles on the chessboard and the real dimension of the green rectangle d in mm, the following equation

$$S = \frac{Rd}{(W_1 R / 2 + W_2 R / 2)} \quad (42)$$

has been used to get the scaling factor S , $S = 0.593$ mm/pixel.

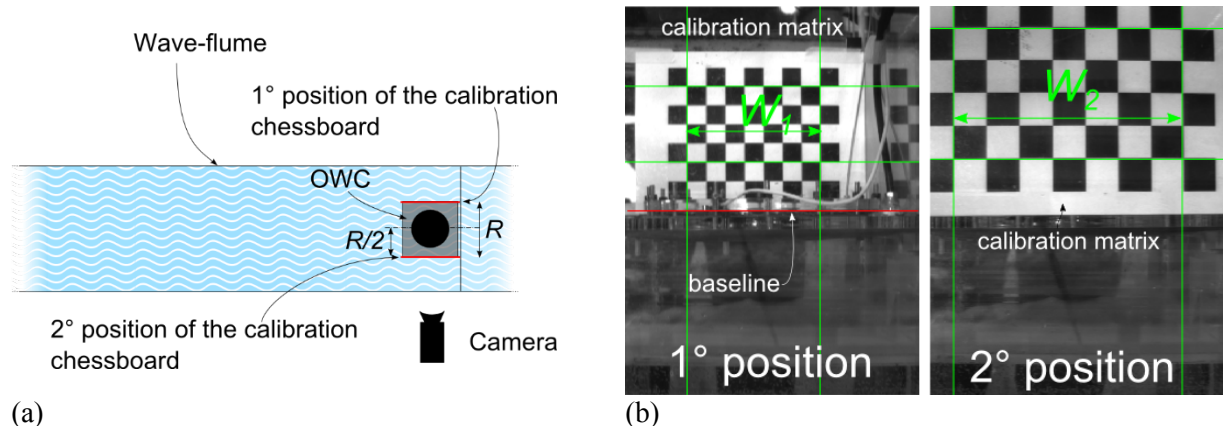


Figure 22 – (a) Position of OWC inside the wave-flume, (b) The images for camera calibration.

Thanks to a calibration phase, an estimation of uncertainty was performed. Based on camera pixel dimensions and the employed video resolution, the uncertainty in the estimation of the CD-DEG tip height resulted as being less than 0.6 mm.

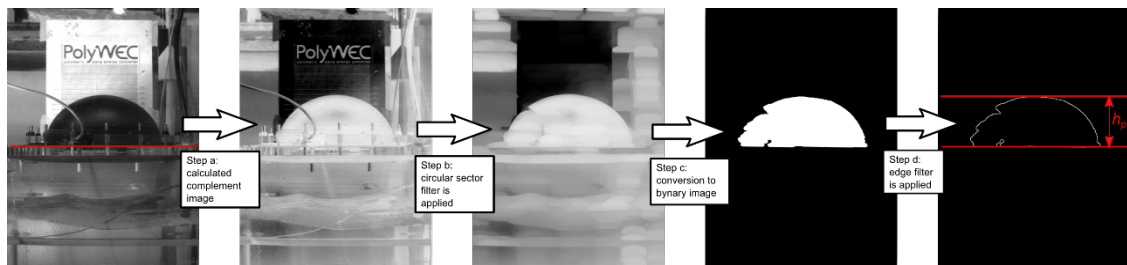


Figure 23 – The main steps for image filtering.

After the calibration, the video is filtered by a Matlab® script to identify the exact tip height. The filtering procedure is divided in the following main steps (shows in Figure 23):

a . Calculated complement image with the Matlab® command:

`I = imcomplement(I);`

b . A circular sector filter is applied. This function highlights the shape chosen, in this case is a circular sector, indicated with (F).

`I = imopen(I,F);`

c . The gray scale image is converted to binary image, based on threshold indicated with alpha, the alpha is chosen heuristically.

`I = im2bw(I, alpha);`

d . An edge finder filter is applied to binary image. The method chosen is “Canny”, that finds edges by looking for local maxima of the gradient of I.

`I = edge(I, method);`

The value of h_p is obtained introducing the scaling factor S and from the tip height in pixel of the membrane, analyzed in the video frames, using the formula: $h_p = S \cdot h_{\text{tip}}$.

5.3 Results

In this section, the experimental results acquired during the wave-flume tests on the small-scale Poly-OWC prototype are summarized and discussed.

Figure 24 reports one of the frame sequences acquired with the high-speed camera. Images are for the test conducted at $f = 0.6\text{Hz}$, $H = 80\text{mm}$ and $V_{in} = 2000\text{V}$. The related CD-DEG tip height, h , which has been obtained by video post-processing, along with the recordings of Poly-OWC gauge air chamber pressure, p , and CD-DEG electric potential difference, V , are shown in Figure 25. Since the response of the system is very repeatable, the reported plots span a single wave period only. For the sake of comparison, the tip-height and pressure plots consider both the response of the Poly-OWC with CD-DEG inactive (dashed line) and with CD-DEG active (solid line). The voltage plot only refers to the case where the CD-DEG is active (namely, when it harvests energy from the waves) and highlights the effective increase in electric potential difference (from $V_{in} = 2000\text{V}$ to $V_{out} = 4800\text{V}$) that is experienced by the charges residing on the CD-DEG electrodes as the CD-DEG contracts.

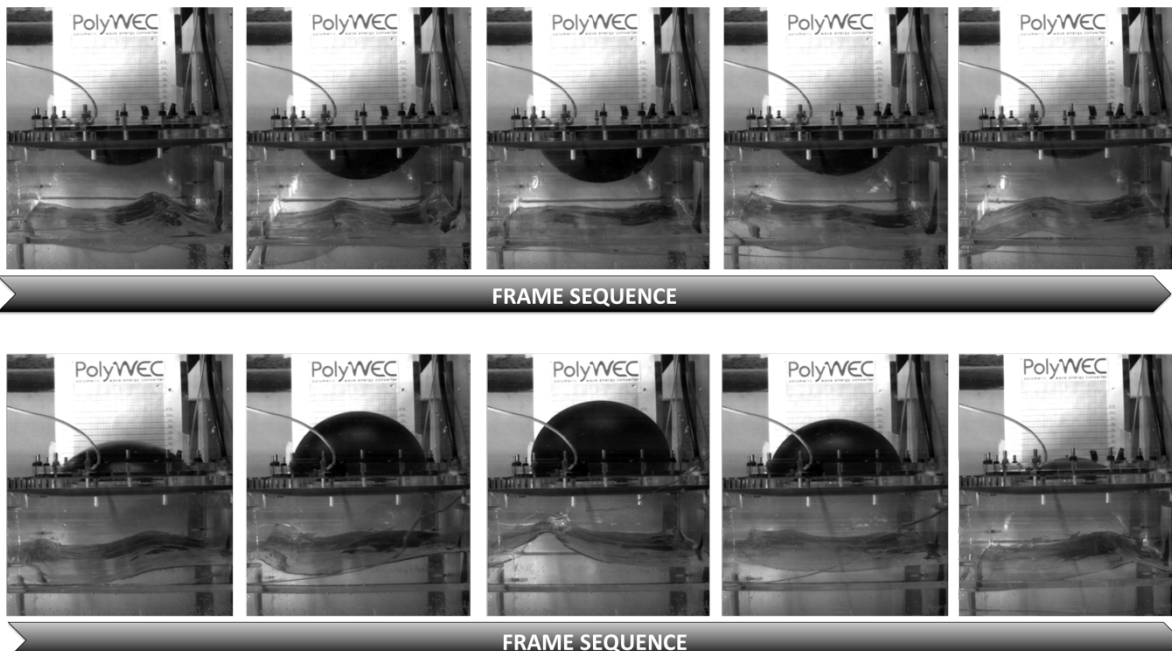


Figure 24 - Full-cycle frame sequence of the small-scale Poly-OWC prototype taken by the high-speed camera during the wave-flume tests (water wave frequency $f = 0.6\text{Hz}$ and height of $H = 80\text{mm}$).

As shown, CD-DEG activation makes it possible to harvest energy from waves (in this case the energy harvested in a cycle is $E_{hc} = 64\text{mJ}$), and this induces a noticeable modification of the dynamic response of the overall system.

The summary of the performances of the Poly-OWC device for different sea states and for different charging voltages is reported in Figure 26-Figure 33. Overall, the following can be stated for the considered small scale Poly-OWC prototype: 1) the energy harvested in a cycle, E_{hc} , increases monotonically as the charging voltage and the wave height, V_{in} and H , increase; 2) the voltage ratio, Φ increases monotonically as the wave height, H , increases; 3) the voltage ratio, Φ decreases monotonically as the charging voltage, V_{in} , increases; 4) viscous loss, ζ increases monotonically as the wave height, H , increases and is rather unaffected by the charging voltage, V_{in} ; 5) as a general trend, E_{hc} , Φ and ζ increase (although not monotonically) with decreasing wave frequency, f ; 6) conversion efficiency, η increases with charging voltage, V_{in} ; 7) the dependency of η on wave height, H , and frequency, f , is difficult to ascertain.

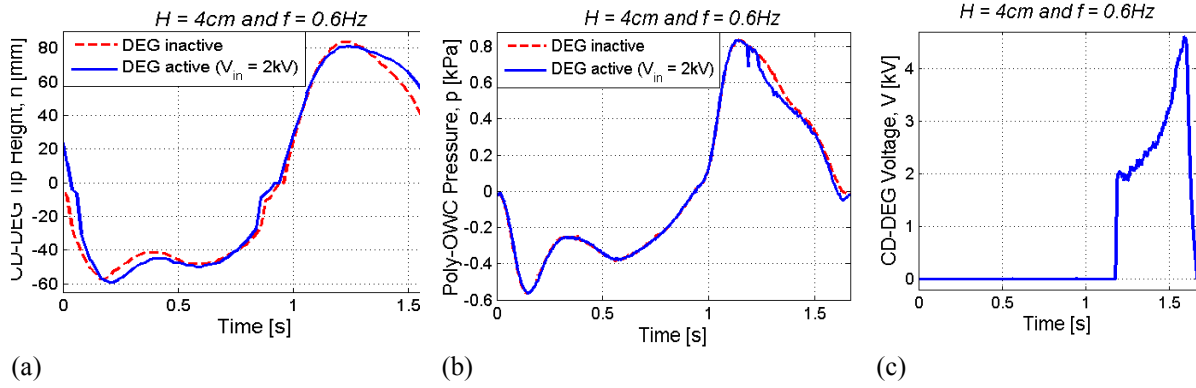


Figure 25 - Experimental assessment of the small-scale Poly-OWC prototype: CD-DEG tip displacement (on the left), air chamber pressure (center) and electric potential difference between CD-DEG electrodes (on the right) as function of the elapsed time in a wave period. Results are for wave frequency and height equaling $f = 0.6\text{Hz}$ and $H = 4\text{cm}$, and for a charging voltage equaling $V_{in} = 2000\text{V}$. Solid line is for active CD-DEG control (energy is harvested); dashed line is for inactive CD-DEG control (energy is not harvested).

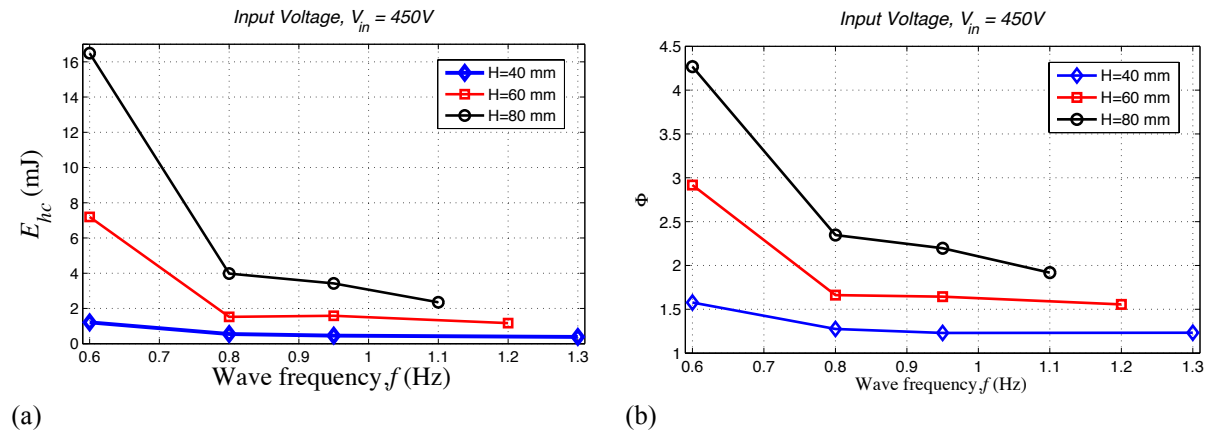
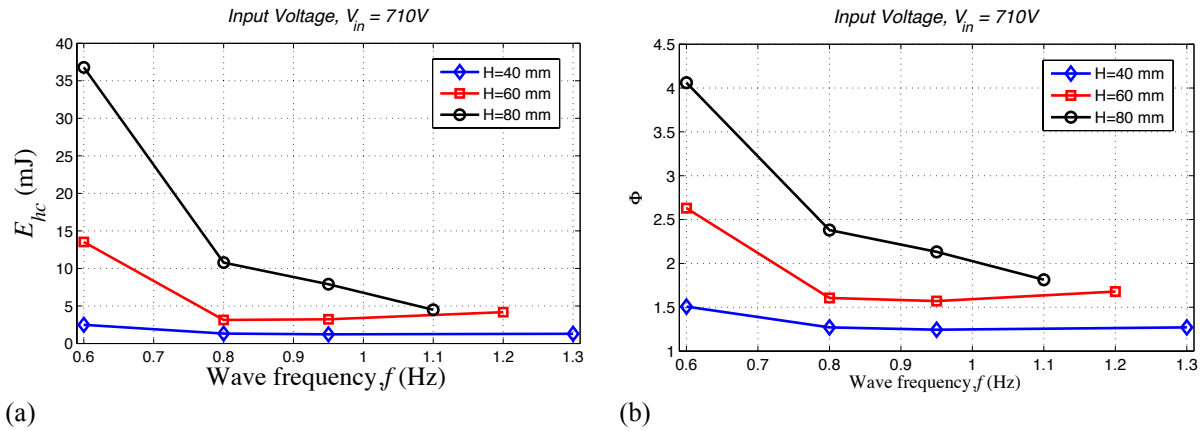


Figure 26 - Experimental assessment of the small-scale Poly-OWC prototype: energy harvested per cycle (a) and voltage amplification ratio (b) as function of water wave frequency, f , and height, H . Results are for a charging voltage equaling $V_{in} = 450\text{V}$.

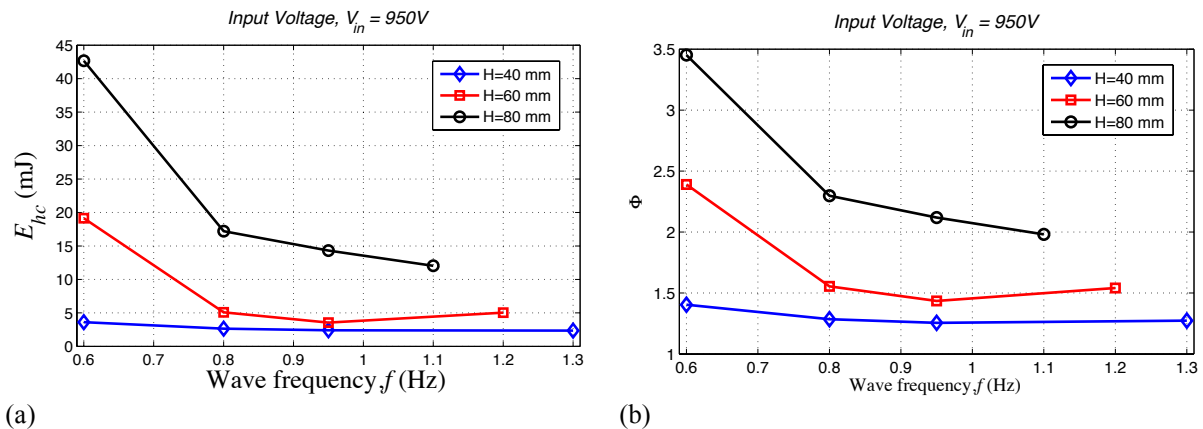
Statement (1), (5) and (6) are coherent both with the increase in the available energy content of the incoming waves with increasing H and decreasing f , and with the increasing energy extraction ability by the CD-DEG with increasing V_{in} . Statement (2) is coherent with the increase of the maximum capacitance value, C_{in} , that occurs as H increases. Statement (3) was not expected, but is motivated by the increasing electrical losses due to current leakage (through the DE material and air) that occur as the electric potential difference between the CD-DEG electrodes increases. This phenomenon has been verified via subsequent test-bench experiments, which also highlighted that most of the current leakage losses are due to charge dispersions in air. In particular, by properly insulating the high voltage CD-DEG electrode, the decrease of Φ with increasing V_{in} can be reduced considerably, which, in turn, is likely to have a significant positive effect on the energy harvested, E_{hc} [21]. Statement (4) is justified since the dynamic response of the considered Poly-OWC is only slightly affected by CD-DEG activation, and since larger H induce both larger deformation ratios of the CD-DEG and larger flow velocities of the water column (this increases the magnitude of dissipative effects such as DE material stress-strain hysteresis and water vortices). Statement (7) is motivated by the highly coupled and non-linear behavior of wave-structure hydrodynamics and CD-DEG electro-visco-elasticity.



(a)

(b)

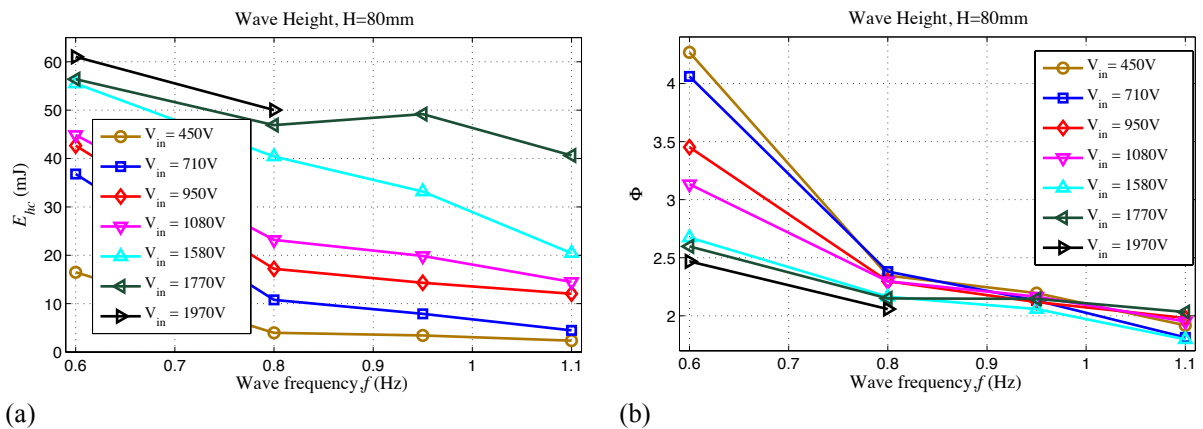
Figure 27 - Experimental assessment of the small-scale Poly-OWC prototype: energy harvested per cycle (a) and voltage amplification ratio (b) as function of water wave frequency and height. Results are for a charging voltage equaling $V_{in} = 710V$.



(a)

(b)

Figure 28 - Experimental assessment of the small-scale Poly-OWC prototype: energy harvested per cycle (a) and voltage amplification ratio (b) as function of water wave frequency, f , and height, H . Results are for a charging voltage equaling $V_{in} = 950V$.



(a)

(b)

Figure 29 - Experimental assessment of the small-scale Poly-OWC prototype: energy harvested per cycle (a) and voltage amplification ratio (b) as function of water wave frequency, f , and charging voltage, V_{in} . Results are for a wave height equaling $H = 80\text{mm}$.

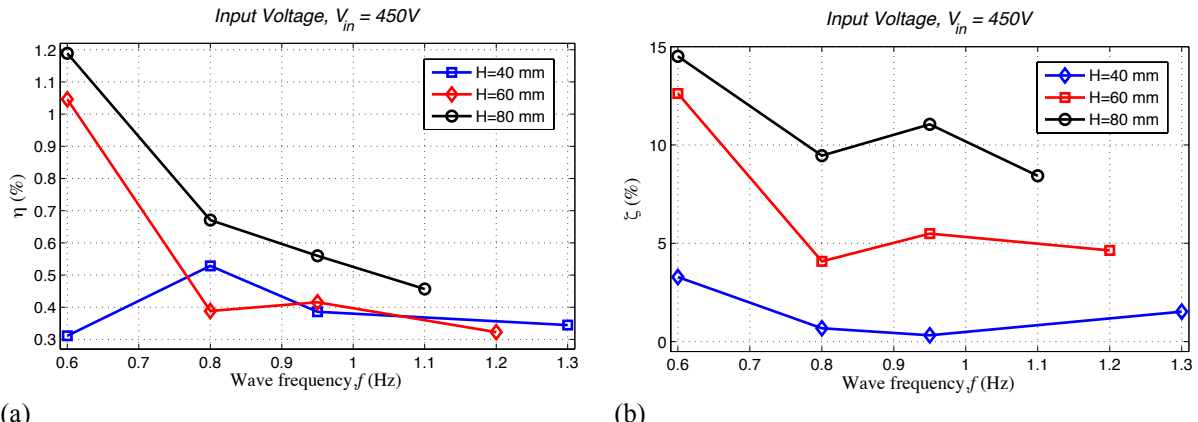


Figure 30 - Experimental assessment of the small-scale Poly-OWC prototype: energy conversion efficiency (a) and viscous loss (b) as function of water wave frequency, f , and height, H . Results are for a charging voltage equaling $V_{in} = 450V$.

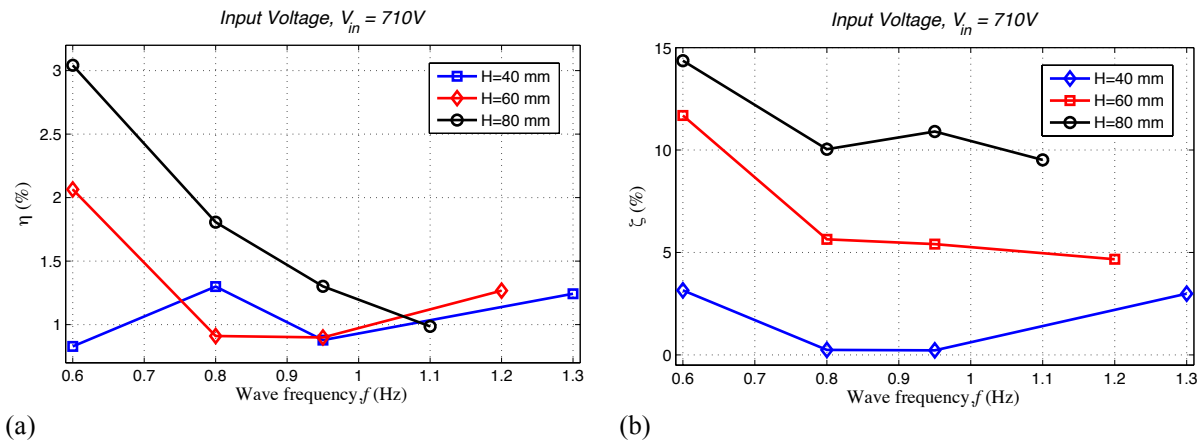


Figure 31 - Experimental assessment of the small-scale Poly-OWC prototype: energy conversion efficiency (a) and viscous loss (b) as function of water wave frequency, f , and height, H . Results are for a charging voltage equaling $V_{in} = 710V$.

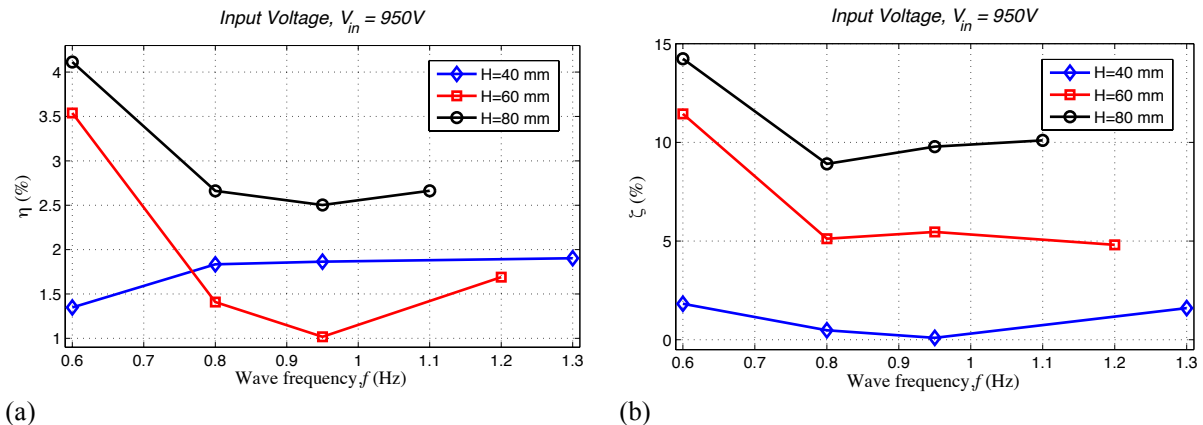
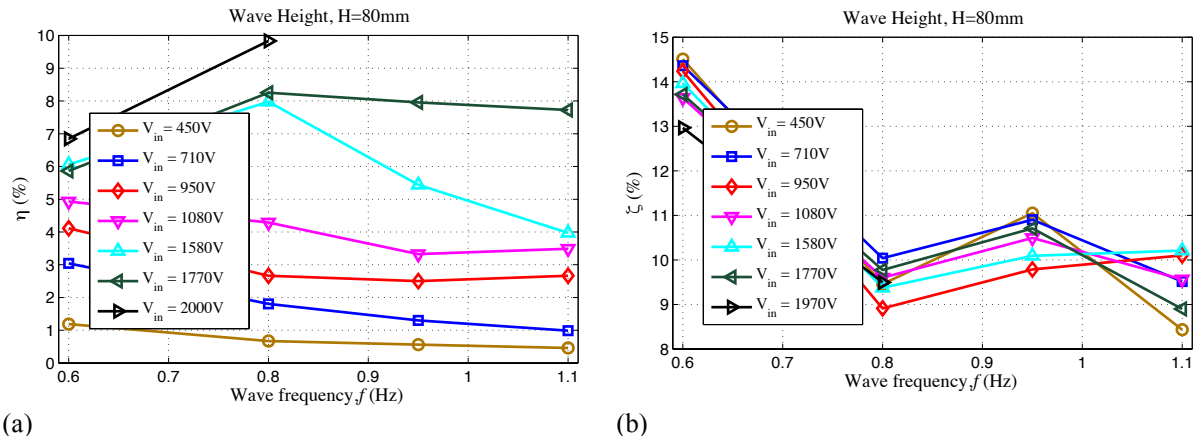


Figure 32 - Experimental assessment of the small-scale Poly-OWC prototype: energy conversion efficiency (a) and viscous loss (b) as function of water wave frequency, f , and height, H . Results are for a charging voltage equaling $V_{in} = 950V$.



(a)

(b)

Figure 33 - Experimental assessment of the small-scale Poly-OWC prototype: energy conversion efficiency (a) and viscous loss (b) as function of water wave frequency, f , and charging voltage, V_{in} . Results are for a wave height equaling $H = 80\text{mm}$.

As aforementioned, the reported results refer to a Poly-OWC prototype with dynamic response not optimized for the considered sea states and employing a CD-DEG with significant dissipative losses (due to significant DE material visco-elasticity and electrical conductivity).

Nonetheless, these results made it possible to validate the Poly-OWC concept as a promising system for wave energy conversion. In fact, although the rather dissipative and non-optimized DEG PTO and the non-optimized hydrodynamics, a power output up to 77mW was obtained that corresponds, in full-scale, to almost 70kW.

5.4 Model validation

In this paragraph, we propose a validation of the electro-hyperelastic model of CD-DEG described in [22]. The CD-DEG reduced model is validated against the time-series measured in the set of tests described in section 5.3.

5.4.1 CD-DEG electro-hyperelastic model validation

In this section, the CD-DEG electro-hyperelastic model is validated against the time-series shown in Figure 25, relative to the case with 80mm wave height, 0.6 Hz wave frequency, and activation voltage $V_{in}=2\text{kV}$. In order to validate the CD-DEG electro-mechanical model presented in Sect. 3.2, gauge pressure time-series (see Figure 25.b) are supplied as input to the CD-DEG model and the resulting membrane tip displacements are checked against experimental measurements.

The following hyperelastic parameters are assumed: $a=0.65 \text{ MPa}$, $I_m=120$ (see also Figure 10.a).

Figure 34 shows the model generated time-series in comparison to experimental time-series. Dashed magenta line refers to the inactive membrane, while dashed cyan line is for the activated membrane and it differs from the previous one only during the electric activation phase. Membrane tip displacements are computed by feeding the measured pressure into equations (24) and solving with respect to h . As regards model validation against electric activation results: the activation voltage is 2000 kV; in the model, the overall charge on the electrodes is considered constant during the electric activation phase; the DEG capacitance is estimated using equation (26).

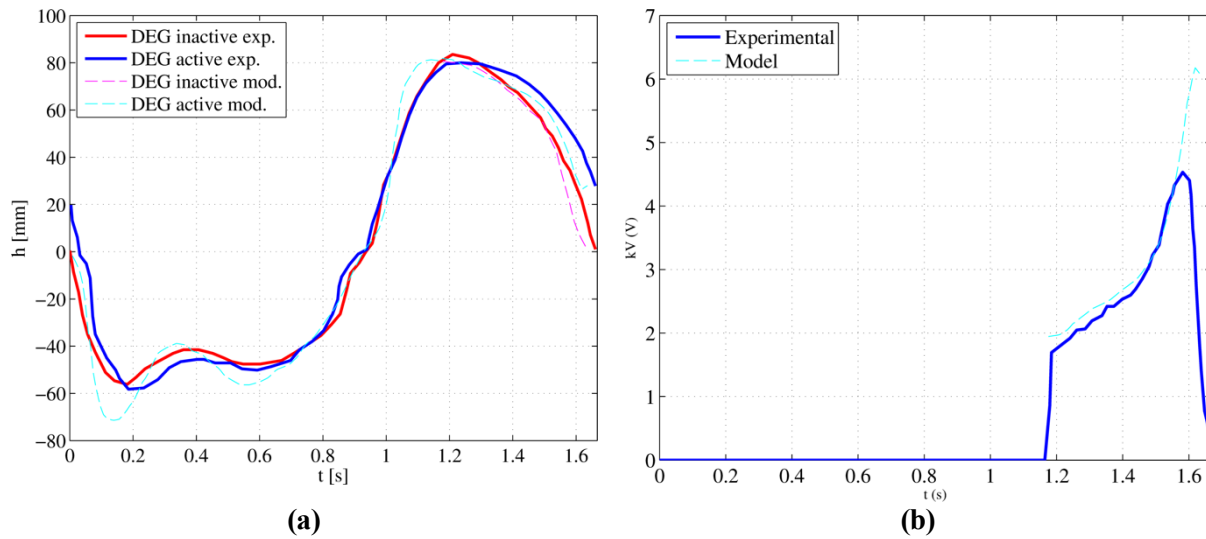


Figure 34 – Experimental and simulated timeseries for the CD-DEG tip height (a) and activation voltage (b). Model data refer to hyperelastic parameters $\alpha=0.65$ MPa and $I_m=120$. Theoretical voltage profile is computed assuming that the charge residing on the electrodes is constant.

The following is observed:

- In general, the model presents a good agreement with experimental data for what concerns the tip displacement estimate. Differences occur mainly because viscous losses have not been included in the model.
- The model is capable to catch the difference in membrane tip elevation in presence of electric activation.
- As regards the voltage timeseries, a discrepancy is evident as the voltage rises. In particular, the theoretical voltage peak is higher than the real one. This is due to loss of charge that, as discussed before, originates from dispersions in the material and through air.

6 FIXED STRUCTURE OWC – ADVANCED DESIGN

This section presents the results of a second campaign of tests on a fixed-structure Poly-OWC, whose collector has been optimized in order to set the resonance frequency of the system to a desired value that is representative of sea waves in a small scale.

The prototype has been tested in August 2014 at UEDIN wave-flume in conditions of Froude hydrodynamic similarity assuming a scale factor of approximately 1:40 with respect to a hypothetic full-scale target device. With respect to previous preliminary tests on a fixed-structure OWC concept (see Sect. 5), the following fundamentals improvements were introduced:

- From a hydrodynamic point of view, the introduction of a horizontal added mass duct at the bottom of the OWC chamber allowed to effectively set the device natural frequency within the testing frequency range. This provided a good evidence for the possibility of compensating the large mechanical stiffness introduced by the polymeric PTO by means of an increased added mass.
- From a control standpoint, energy conversion cycles were optimized by introducing an in-parallel constant capacitor (connected to the DEG), which allows to increase the maximum energy density that the DEG can convert in a cycle, as demonstrated in sect. 3.3.5 of [2] and [24].
- Models validation has been performed based on the collected experimental data. In order to separately check the validity of DEG electro-elastic model and collector hydrodynamic model, validation has been carried out in two steps. First, CD-DEG membrane tip elevation time-series have been checked against experimental acquisitions feeding the measured pressure (both in presence or absence of electric activation) into the DEG model. Successively, the collector hydrodynamic model has been coupled with the passive membrane elastic model and membrane tip elevation has been compared with experiments, feeding the tank generated waves parameters into the model.

6.1 Experimental setup

The OWC model consists on a set of polycarbonate plates, with a thickness of 10mm, that are assembled to form a hollow parallelepiped chamber open to the water through a horizontal duct (namely, added mass duct). The added mass duct has the aim of providing the system with increased inertia and tuning it with incoming waves within the range of interest. This design for the collector has been chosen because it allows to easily set the ratio between hydrostatic stiffness and inertia (approximately coinciding with the water mass within the collector), so as to achieve resonance within the desired range of testing frequencies. In fact, the prototype is designed in a way so that the length of the added mass duct can be adjusted by mounting the front panel in a set of different positions (see Figure 35.a). A picture of the setup during tests is shown in Figure 35.b.

The dimensions of the prototype are as in Figure 35.c. The OWC chamber has a square section with 0.37m edges. In flat-water conditions, water depth within the chamber is 0.335, and the height of the air column is 0.15m. Three possible lengths are allowed for the added mass duct: 0.3m, 0.6m and 1m. The chosen setting for the experiments was 0.6m, as this choice was found to provide resonance with the desired sea states. The model is positioned on an inclined sea-bed with a slope which reproduces shallow water conditions.

The top plate of the OWC structure has a hole where the CD-DEG is fastened through polycarbonate rings. Such aperture has a radius $e = 0.125\text{m}$. In the tests, acrylic elastomer VHB 4905 has been used as DE material, and electrodes have been painted using MG-Chemicals 846 conductive grease. The CD-DEG sample has been made by superimposing 3 layers, each with a thickness of 0.5mm (i.e., the unstretched membrane has a thickness $t_0 = 1.5\text{mm}$), that have been pre-stretched to $\lambda_p = 4$. Projected in full-scale according to the coefficients of Table 3, the full-scale CD-DEG pre-stretched dimensions are $e=5\text{m}$ and $t=0.15\text{m}$.

The employed power electronics and sensing equipment is the same to that described for the previous set of experiments (see sect. 5.1).

As regards energy harvesting control, a constant capacitance $C_a = 78\text{nF}$ has been connected in parallel to the DEG. The control logic is such that the overall charge on the DEG plus C_a is constant during the electric activation phases (apart from loss of charges due to leakage currents across the material and

dispersions in air). The value of C_a has been properly chosen to optimize the maximum energy that the DEG can convert in a cycle (in its widest allowed deformation range). That is, the introduction of the in-parallel capacitance allows to increase the maximum voltage on the DEG while protecting it from electric break-down [24]-[28].

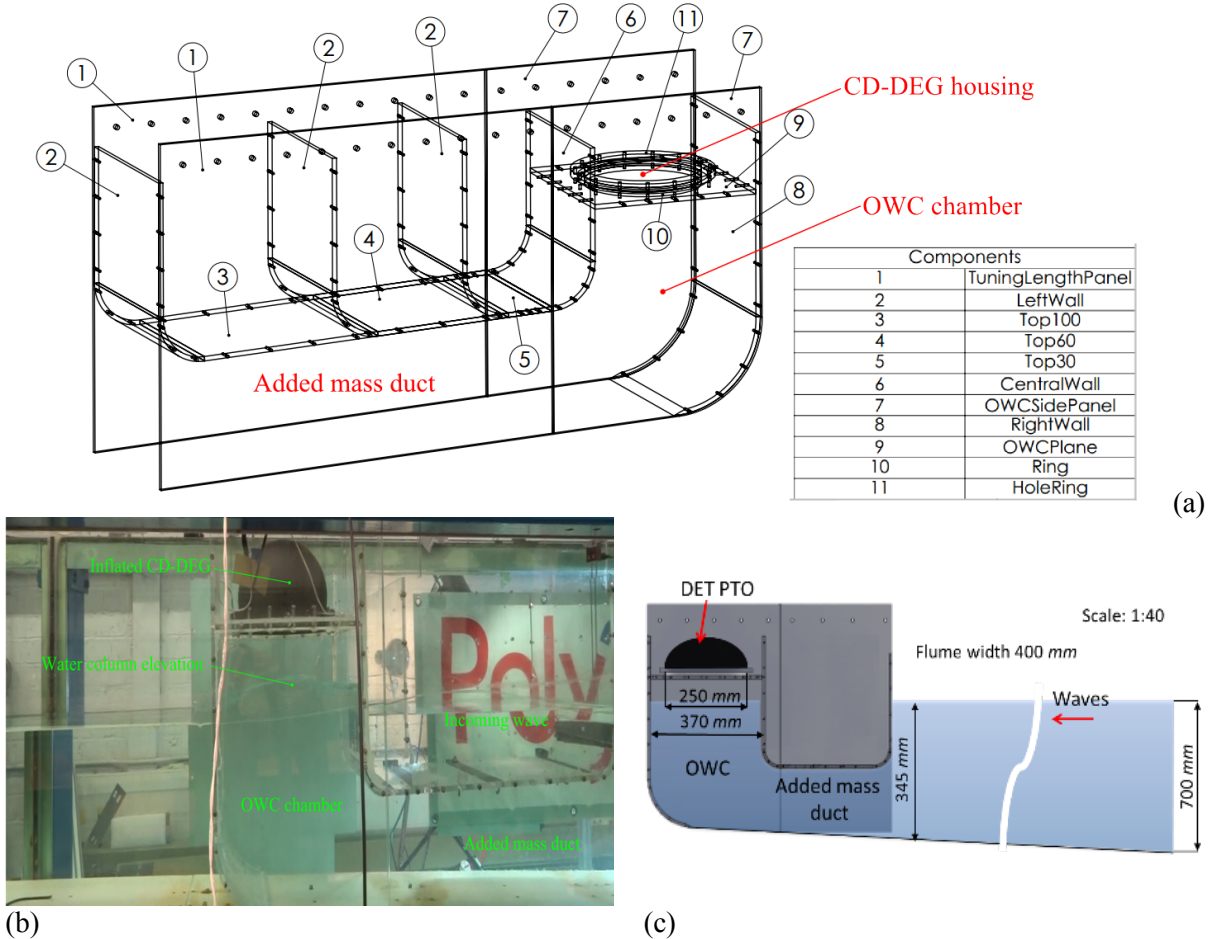


Figure 35 – (a) Drawing of the OWC structure prototype assembly; (b) Picture of Poly-OWC prototype during operation; (c) Dimensions of the prototype.

A schematic of the CD-DEG control circuit is shown in Figure 36.a. Given such an architecture, the energy conversion cycle consists of the following operations: 1) fast charging of the parallel CD-DEG - C_a , with a power supply at voltage V_{in} , when the diaphragm gets maximally expanded (that is, when the CD-DEG capacitance reaches a maximum value, C_m); 2) constant charge is kept on the capacitances parallel as the CD-DEG returns to its flat configuration; 3) discharge the two capacitors when the DEG is flat (i.e., its capacitance, C_{out} , is minimum and the electric potential difference between its electrodes, V_{out} , is maximum); 4) CD-DEG and C_a are not active as the DEG expands. Triggering between states 4 and 1 is enabled using the time derivative of the pressure signal; triggering between states 2 and 3 is obtained by monitoring the inversion of the pressure sign; triggering between states 1 and 2 as well as between states 3 and 4 is obtained after a fixed time interval. The energy harvesting controller of the Poly-OWC is implemented on a real-time machine (Performance real-time target machine by SpeedGoat) via the Matlab® xPC Target software environment.

In terms of electric variables (charge, Q , and voltage, V), the control cycle described above is graphically represented in Figure 36.b. Transformation 1 (instant charging) coincides with transformation OA' in the picture; constant charge phase 2 is A'B', discharging 3 is B'O. Phase 4, which is a purely mechanical transformation, is not visible in the plot. The slope of curve A'B' in the plot is given by $-C_a^{-1}$. Notice that,

for a proper choice of C_a , cycle OA'B'O well approximates cycle OABO, which is the maximum-energy conversion cycle, and depends on the physical limitations of the material (e.g., electric break-down).

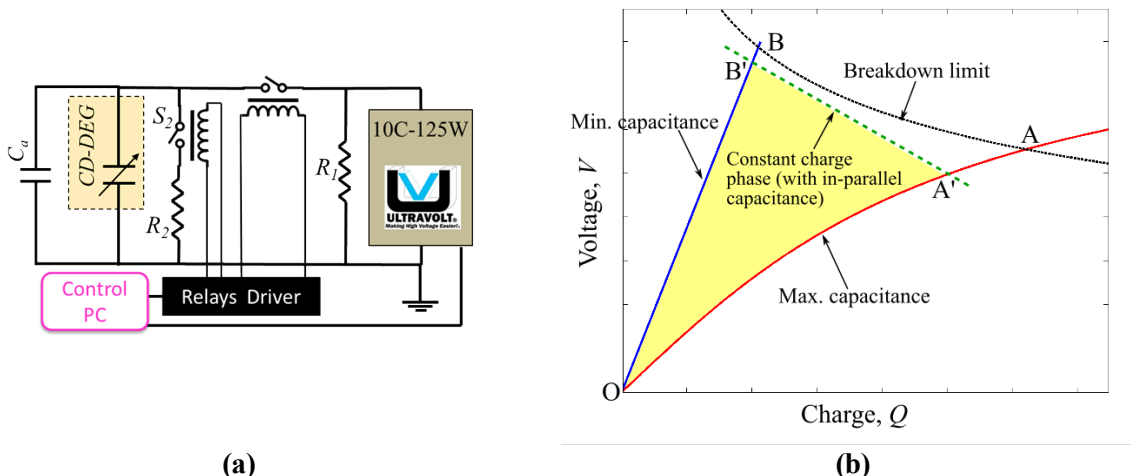


Figure 36 – (a) Electronic circuit controlling the CD-DEG. Here C_a is the in-parallel capacitance needed to optimize the DEG conversion cycles. (b) Comparison of maximum-energy harvesting cycle (due to material physical limitations) and sub-optimal conversion cycle, with in parallel capacitance.

6.2 Procedure, Processing and Elaboration of data

Experiments have been performed using a wide set of wave parameters (frequency and height) and activation voltages. Regular (monochromatic) sea states have been generated during the experiments. Three values of charging voltage have been considered: $V_{in} = [3500V, 4000V, 4300V]$. The following wave frequencies, f , and heights, H , were employed: $f = [0.5Hz, 0.7Hz, 0.9Hz, 1.1Hz]$, $H = [30mm, 60mm, 90mm]$.

As for the previous set of experiments, the wave flume was started from a fully flat condition, and a few minutes (before the CD-DEG activation) were waited in order to guarantee the achievement of the settled sea state. Differently from previous experiments, the CD-DEG was activated twice per period, both when it expanded upward and downward with respect to the reference flat configuration, $h=0$.

Pressure, p , and voltage, V , measurements were acquired at 1kHz together with the commands of opening and closing of the different relays; CD-DEG inflation/deflation (expansion/contraction) was captured with a high-speed camera at a frame rate of 100fps arranged on the side of the wave-flume as depicted in Figure 35.a. All the signals recorded, video frame, pressure, voltage, etc. were synchronize with the same trigger activated from the real-time target machine.

Data processing

In order to estimate the above mentioned figures (equations 36-41), it was necessary to estimate the capacitance C of the DEG. This has been done by introducing in equation (26) the instantaneous value of $h(t)$ (note the relation of equation (26) has been preliminarily validated at the beginning of the tests against the measurements of an LCR meter in an appropriate range of tip height).

To this aim, acquired data from the camera were post-processed to obtain tip height, $h(t)$ via the custom-developed software described in section 5.2.

Data elaboration

With the available processed data it has been possible to calculate several figures of merit of the system. For every wave period, energy generation cycles occur twice: both for inward and outward expansions of the CD-DEG. The electrical energy generated in the i -th cycle is denoted by E_{hc_i} , and is given by:

$$E_{hc,i} = \int_0^{V_{out,i}} Vd(C_{out,i}V) - \int_0^{V_{in,i}} Vd(C_{in,i}V) + \frac{1}{2} C_a (V_{out,i}^2 - V_{in,i}^2) \quad (43)$$

where $V_{in,i}$ and $V_{out,i}$ are the voltages on the CD-DEG (and on C_a) respectively at the end of the DEG charging and discharging phases of the i -th cycle.

As in (36), this equation keeps into account the amount of electric energy provided to and recovered from the CD-DEG and the in-parallel capacitance, C_a , during the charging and discharging phases. The CD-DEG capacitance is assumed to be, in general, variable during charging ($C_{in,i}$) and discharging ($C_{out,i}$) phases, even though, in these experiments, a constant value can be assumed when the DEG is discharging, which takes place when $h \approx 0$ (see the cycle in Figure 36.b).

The average power is calculated from $E_{hc,i}$ values as follows:

$$P_{hc} = \frac{\sum_{i=1}^N E_{hc,i}}{t_{TOT}} \quad (44)$$

where N is the total number of successful generation cycles in a test-run, which take place over a time span $t_{TOT} = N/(2f)$. We have removed from the computation some failed and scarcely synchronized cycles that were mainly due to failure in opening or closing of one of the relays.

The average energy harvested for each half wave period can then be defined as

$$E_{hc} = P_{hc}/(2f) = \frac{\sum_{i=1}^N E_{hc,i}}{N} \quad (45)$$

Notice that the calculated energy does not keep into account the eventual electric losses that occur in passing the harvested energy from the CD-DEG electrodes to the external energy storage.

A further parameter that is interesting to monitor is the percentage of the incoming wave power effectively converted into electrical energy, defined as:

$$\beta = P_{hc}/P_w, \quad (46)$$

where the power, P_w , carried by the undisturbed waves is given by [29]:

$$P_w = \frac{\rho_w g H^2 c_g w}{8} \quad (47)$$

where ρ_w is the water density, w is the flume width (namely, $w=0.4\text{m}$), and c_g is waves group velocity, which, for regular waves, is given by:

$$c_g = \frac{g}{4\pi f} \tanh(kh_w) \left(1 + \frac{2kh_w}{\sinh(2kh_w)} \right), \quad (48)$$

being h_w the water depth upstream of the device and the beach (namely, $h_w=0.7\text{m}$), and k the wave number, which is the solution of the following implicit equation:

$$\frac{gk}{4\pi^2 f^2} \tanh(kh_w) - 1 = 0. \quad (49)$$

6.3 Results

This section reports results of wave-flume tests data post-processing. The identified performance parameters are compared over voltage, wave height and wave frequency.

In Figure 37.a and Figure 37.b, time-series describing the CD-DEG dynamics are reported for two experiments featuring $f = 0.7\text{Hz}$, $H = 30\text{mm}$, $V_{in} = 4000\text{V}$ and $f = 0.9\text{Hz}$, $H = 45\text{mm}$, $V_{in} = 4300\text{V}$ respectively. In particular, in each figure the first plot is for the relative air pressure, p , within the chamber, second plot is for the tip elevation, h (obtained by video post-processing), and last plot is for the voltage on CD-DEG and C_a .

The plots show that: 1) as CD-DEG capacitance decreases, voltage between the electrodes of the DEG (and of C_a) effectively increases during electric activation phases; 2) electric activation has a perceivable effect on the WEC dynamics. Indeed, from tip height time-series, it emerges that oscillations in h have smaller amplitude when the membrane is active, i.e., electric activation effectively damps the water column motion.

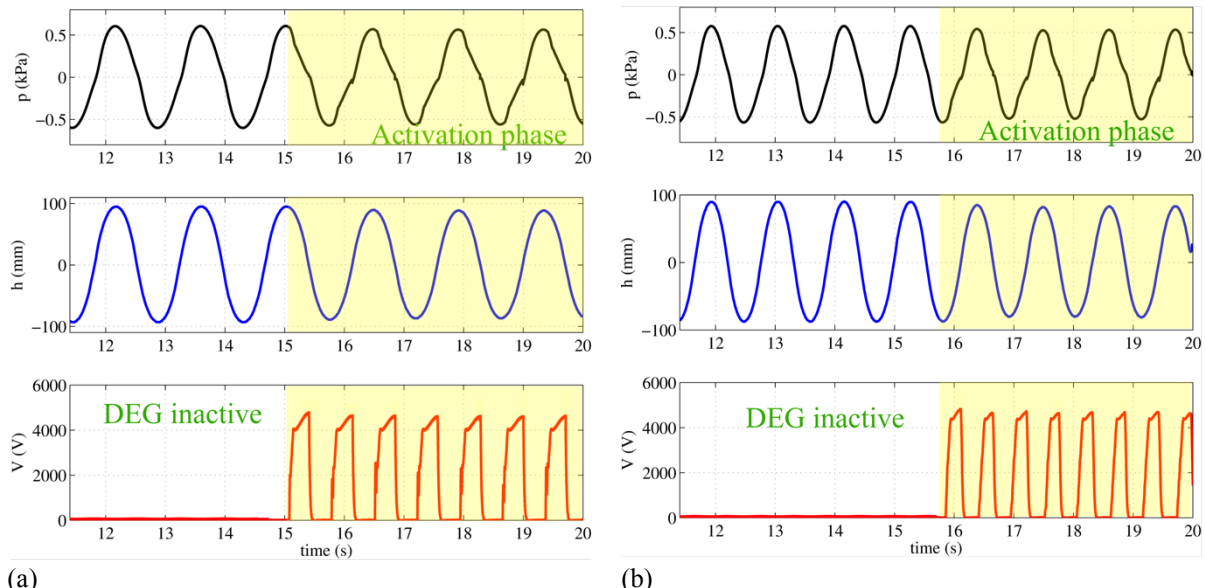


Figure 37 – Gauge pressure, tip height and CD-DEG voltage time-series for two experiments: (a) $f = 0.7\text{Hz}$, $H = 60\text{mm}$ $V_{in} = 4000\text{V}$; (b) $f = 0.9\text{Hz}$ $H = 90\text{mm}$ $V_{in} = 4300\text{V}$. Highlighted areas refer to phases in which the DEG is cyclically activated/deactivated.

Plots of Poly-OWC prototype performance for different sea states and different activation voltages are shown in Figure 38-39. From the graphs, it emerges that the system was able to convert a substantial amount of energy, reaching peaks of almost 0.9W that is not so common for small-scale tests.

Average power plots provided in Figures 38 show that the system bandwidth is upper-bounded to approximately 0.9Hz and peaks of power production are recorded near 0.7 Hz. This means that the system resonance has been successfully set into the desired range of wave frequencies that can be produced in the wave-flume.

A similar behaviour is observed for the energy in the plot of E_{hc} versus frequency (Figures 38-39). In particular, a maximum average energy per half wave period of 0.63J is observed for a wave frequency of 0.7Hz and wave height of 90 mm and an activation voltage of 4300 V. This value corresponds to an energy per unit volume of dielectric material (i.e. energy density) of 135J/kg. This happens for a corresponding maximum electric field in the dielectric of 40-60MV/m that is well below the maximum limiting values of 100-300 MV/m.

As shown in Figure 38, the power (and energy per cycle) is generally dependent on wave height and frequency. As expected, average power (and energy per half wave period) always increases with wave height. As it can be observed, a substantial amount of power is generated only for wave heights greater (or equal) than 30mm. This can be attributable to charge loss from the high voltage electrode that was left open

to air. The amount of this power losses becomes negligible with respect to generated output when the wave height increases. The fraction of the incoming wave energy that is converted into electricity (figure of merit β) is not always proportional to the wave height. In particular the maximum of β equal to 18.6% is observed for a wave height of 60mm and input voltage of 4300V. This can be attributable to the non linear behavior of the different sources of energy losses, i.e. electrical energy due to charge dispersion, viscous losses in the water and in the dielectric material.

As shown in Figure 39, power (and energy for half wave period) is generally dependent on the input voltage. Specifically, the power output increases with the input voltage, except for the case of wave height of 30mm at low frequency. This behaviour is attributable to measurements errors, due to which the amount of converted energy is too small to be effectively evaluated.

Maximum produced power is about 871mW that, projected to a full-scale device with $f_s=40$ corresponds to 352kW. This is a very interesting value, especially considering that the employed material for the DEG is only suboptimal. In fact, as already discussed in preceding sections, the highly dissipative acrylic elastomer (VHB-4905) was the only practical choice for small-scale tests because of its reduced stiffness. Specifically, much of the losses occurred in the reported tests are attributable to the viscosity of the acrylic elastomer especially at large strains (higher waves). A strong improvement is expected for larger scale systems for which the acrylic elastomer can be substituted by more performant materials such as rubbers (natural or synthetic) and silicones.

Other possible improvements that could be introduced are the following:

- Isolation of high voltage electrodes with an insulating layer to avoid dispersion of charges. This could be introduced at larger scales because the influence on the system dynamic response of a thin (yet thick enough to be effective) layer of insulation can become negligible only above certain scales.
- Reduction of water viscous losses by redesign of the inner shape of the collector. With large wave heights, a sloshing effect inside the OWC chamber was clearly observable. A proper re-design of this component could enhance the improvement of system performances.

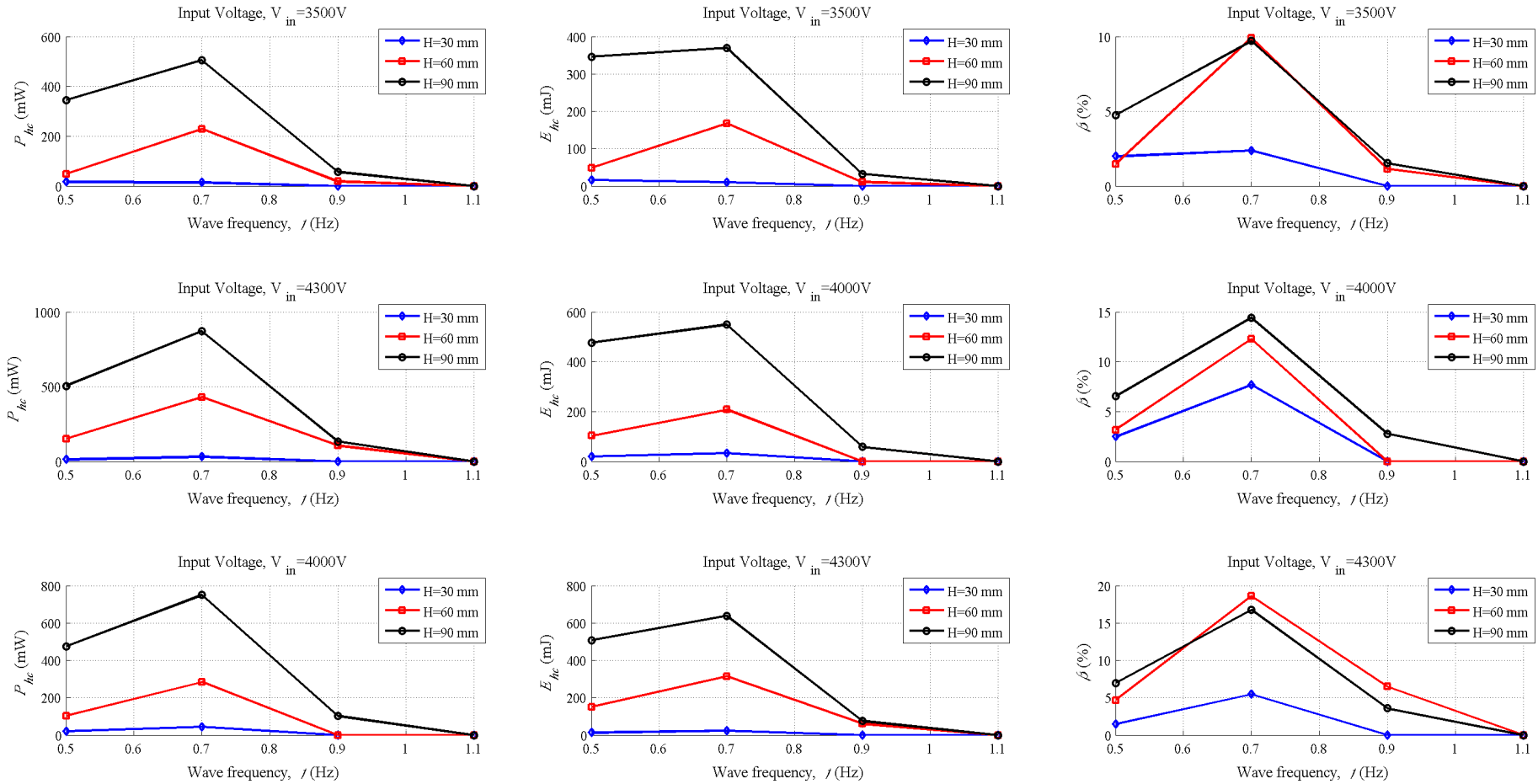


Figure 38 - Experimental assessment of the Poly-OWC prototype: average converted power (left); average converted energy per half wave period (center) and average rate of converted energy (right). All plots are provided against f for different wave height $H=30\text{mm}$ (blue-romoidal), $H=60\text{mm}$ (red-squared) and $H=90\text{mm}$ (black-circle). Three different input voltage are shown: $V_{in}=3500$ (top), $V_{in}=4000$ (middle) and $V_{in}=4300$ (bottom).

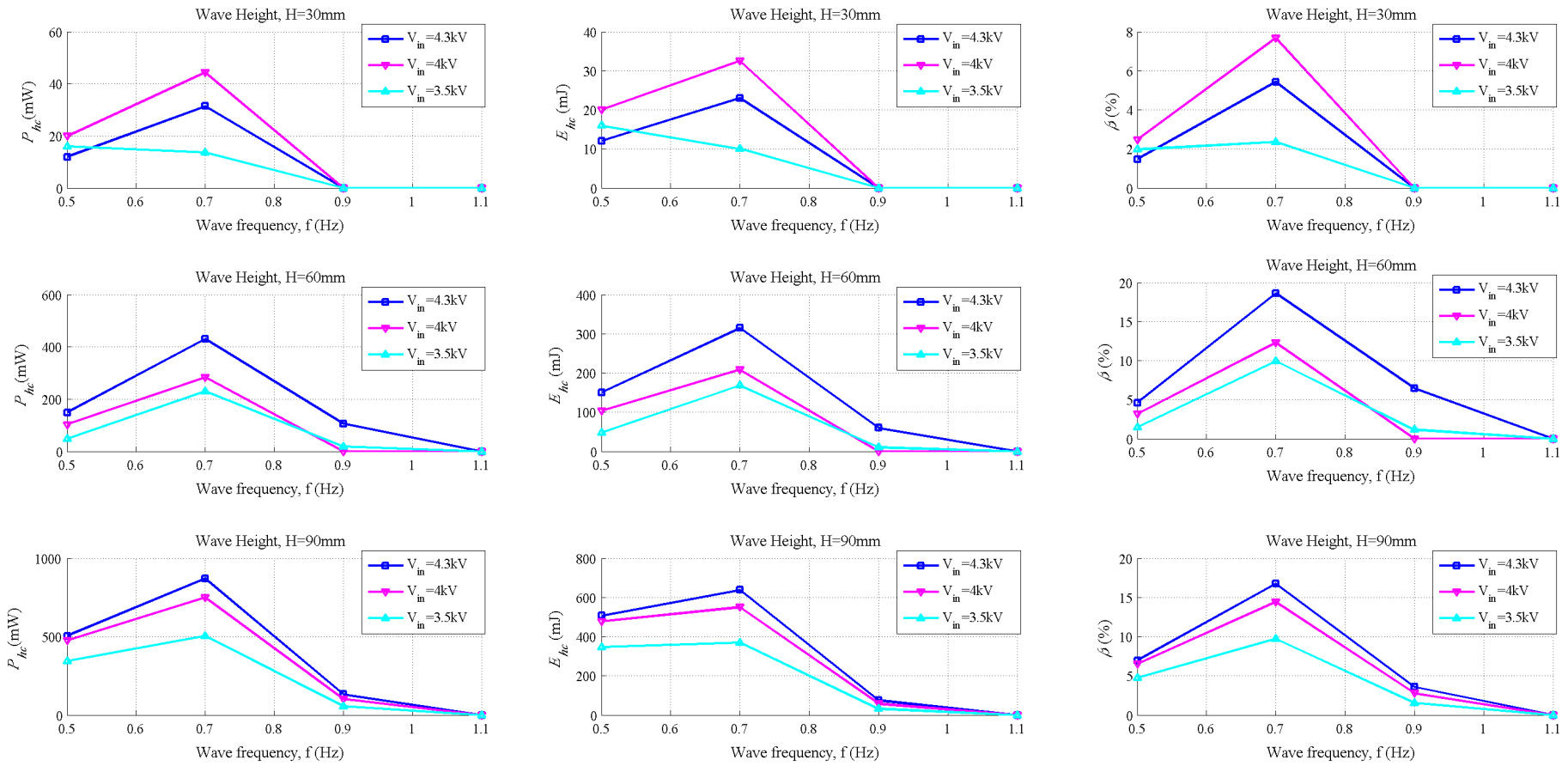


Figure 39 - Experimental assessment of the Poly-OWC prototype: average converted power (left); average converted energy per half wave period (center) and average rate of converted energy (right). All plots are provided against f for different wave height $H=30\text{mm}$ (top), $H=60\text{mm}$ (middle) and $H=90\text{mm}$ (bottom). Three different input voltage are shown: $V_{in}=3500$ (light-blue-upward-arrow), $V_{in}=4000$ (purple-downward-arrow) and $V_{in}=4300$ (blue-squared).

6.4 Model validation

In this section, experimental data collected on the second Poly-OWC prototype are used to validate electro-elastic and hydrodynamic models developed within PolyWEC project [1].

Models validation is provided following an incremental approach, i.e., electro-elastic DEG models are first validated against the deformation response of the active/inactive membrane using pressure data as input. Successively, a coupled elasto-hydrodynamic model for Poly-OWC is presented and validated against experimental data on pressure and membrane displacement.

6.4.1 CD-DEG electro-hyperelastic model validation

In this section, the CD-DEG analytical model presented in [22] and in sect. 5.4.1 is validated using air pressure time-series as input to the model and comparing tip height results with experimental data, similarly to section 5.4.1.

The following hyperelastic parameters are used: $a=0.92$ MPa, $I_m=137$ (see Figure 10.a).

Results from validation are shown in Figure 40. The time-series previously shown in Figure 37 are used as benchmark. In these time-series, some of the oscillations are without electric activation, while the remaining ones occur with the DEG fully-functional and electrically activated.

Pressure profiles (upper plots) are used as input data for the model and are fed into equation (24). Predicted tip elevation, h , is represented in magenta (dashed line) and plotted against experimental time-series (blue line) in the middle graphs.

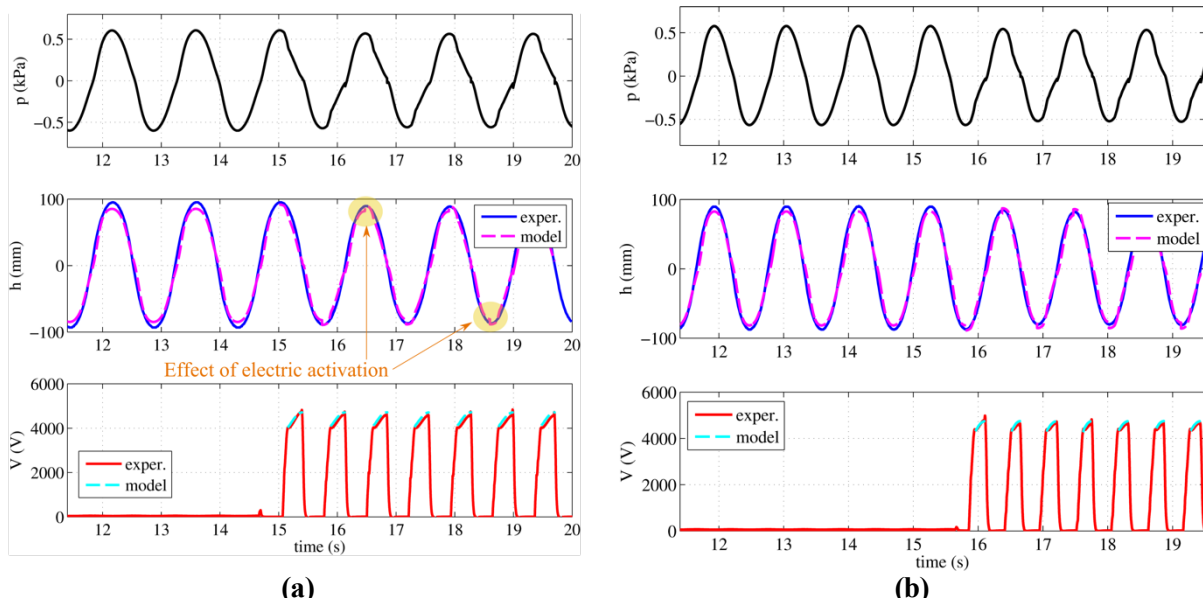


Figure 40 – CD-DEG model validation against experimental time-series previously shown in Figure 37. Solid lines are experimental data, while dashed lines are model-based predictions. The two pictures refer to the following test conditions: (a) $f = 0.7\text{Hz}$, $H = 30\text{mm}$ $V_{in} = 4000\text{V}$; (b) $f = 0.9\text{Hz}$ $H = 45\text{mm}$ $V_{in} = 4300\text{V}$.

Finally, theoretical predictions of the voltage time-series are presented, assuming that the total charge Q_0 on the parallel DEG + C_a is constant, and using equation (26) for the determination of CD-DEG capacitance, namely:

$$V = \frac{Q_0}{C_{DEG} + C_a}. \quad (50)$$

Here, Q_0 is calculated using the measured voltage and estimated capacitance (from measured tip height) at the end of the charging phase. Moreover, it is assumed that the charge Q_0 is supplied to the parallel of the DEG and C_a instantly, and this instantaneous charging is synchronized with the end of the experimental charging phase (when the switch that connects the DEG and the power supply opens). In the same way, the discharging of the DEG (and C_a) is modelled as instantaneous and is synchronized with the closure of switch

S_2 (Figure 36.a). The resulting predictions for the voltage time profiles are compared with experiments in the lower plots.

Figure 40 shows a very good agreement between experiments and models, thus demonstrating that 1) proposed CD-DEG electro-hyperelastic models are capable to capture the device response, 2) VHB-4905 fitted hyperelastic parameters are effective and quite reliable, 3) modest loss of charge (due to leakage current and dispersions through air) occurs during the experiments, indeed experimental values are in good agreement with theoretical predictions that are obtained under the assumption of overall charge (on CD-DEG plus C_a) remaining constant during each activation phase.

Despite the good agreement between experiments and model, some minor gap in the model can be identified. That is, according to the quasi-static model employed in this deliverable, the instant electric activation of the membrane is responsible for a sudden increase in the membrane tip displacement, i.e., as the membrane is activated, its configuration changes and the membrane finds a new equilibrium with the applied pressure at a moderately greater strain (see the peaks in the time profiles of Figure 40 in presence of electric activation). For the safe voltages employed in the present tests, this behavior is not detected in practice. Future developments will include viscoelasticity models integration and fitting of viscous constitutive parameters.

Finally, we propose a comparison of DEG capacitance and voltage values calculated in a few relevant instants during the conversion cycles. The values of capacitance used for comparison are: 1) mean DEG capacitance during the charging phase, \bar{C}_{in} ; 2) mean DEG capacitance during the discharging phase \bar{C}_{out} .

The relevant voltage values used for comparison are: 1) voltage at the end of the activation phase, \bar{V}_{in} ; 2) voltage at the beginning of the discharging phase \bar{V}_{out} .

Table 6 reports the comparison between model and experiments, in terms of the mentioned variables, and for both the sea states of Figure 40.

Table 6 – Comparison between experiments and model in terms of average CD-DEG capacitance and voltage during charging/discharging phases, and converted electrostatic energy.

Variables	(a) $f = 0.7\text{Hz}, H = 30\text{mm} V_{in} = 4000\text{V}$		(b) $f = 0.9\text{Hz} H = 45\text{mm} V_{in} = 4300\text{V}$	
	Experim.	Model	Experim.	Model
\bar{C}_{in} (nF)	36.2	34.0	27.7	28.6
\bar{C}_{out} (nF)	19.1	19.1	19.1	19.2
\bar{V}_{in} (kV)	4.02	4.08	4.38	4.33
\bar{V}_{out} (kV)	4.63	4.71	4.70	4.75

Table 6 shows a generally good agreement between theoretical and experimental values of capacitance and voltage with errors of less than 10% estimated in the instants of activation. Generally, better matching is found for more energetic waves since the produced energy for each half wave period is generally greater than the energy supplied during the activation phase.

6.4.2 Poly-OWC elasto-hydrodynamic model validation

In this section, a simplified model for the coupled hydrodynamics of the OWC collector and hyperelastic response of the membrane (in absence of electric activation) is validated against experimental data.

The aim is to verify the capability of the model to predict the resonant behavior of the coupled WEC-DE PTO system.

For this purpose, a rather simple model for the OWC collector hydrodynamics has been used, which does not employ Boundary Element Method (BEM) codes and radiation-diffraction parameters (frequency dependent radiation damping, added mass, etc.) as indicated by [2].

Given the peculiar design of the present OWC collector (with a long added mass duct at the water column inlet), the dependence of such hydrodynamic parameters on the wave frequency is expected to be small. That is, water column damping and added mass can be considered as independent of frequency, with the latter approximately coinciding to the displaced water mass within the OWC chamber plus the added mass of water within the duct. For this reason, the water column dynamics has been modeled using the approach

proposed by other authors (e.g., Boccotti et al. [30], Arena et al. [31], Czitrom et al. [32]) and employed in early studies on the Poly-OWC concept [17], [22].

We consider the chamber geometry with the dimensions defined in Figure 41.a. Since the slope of beach is very mild (water depth varies from 0.7m to 0.35m in 7.5m, compared to 0.6m length of the added mass duct), the added mass duct and OWC main chamber cross sections can be assumed as being constant.

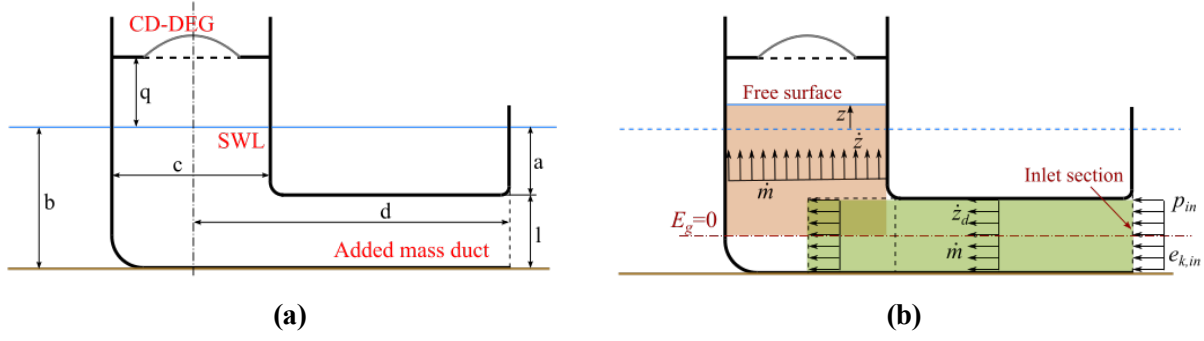


Figure 41 – Definition of geometrical quantities featuring the OWC prototype

The approach adopted here relies on generalized (non-steady-state) Bernoulli's equation and the following energy balance for the water volume confined within the collector:

$$\frac{d}{dt} (E_k + E_g) = \dot{W}_{ext} + \dot{m} \left(\frac{p_{in}}{\rho_w} + e_{k,in} + e_{g,in} \right) \quad (51)$$

where

- E_k and E_g are the kinetic energy and gravitational potential energy of the involved water domain;
- \dot{W}_{ext} is the mechanical work made on the system by external forces (namely, air pressure in the chamber and viscous friction);
- \dot{m} is the mass flow rate through the added mass duct, and it is positive when water goes into the chamber from the outside (rising free surface);
- The quantities into parentheses represent the energy carried inside/outside of the system by the inlet/outlet water flow. In particular, p_{in} is the absolute water pressure at the inlet section, $e_{k,in}$ is the transported water kinetic energy and $e_{g,in}$ the transported gravitational energy at the inlet section;
- ρ_w is the water density.

The water velocity within the added mass duct is denoted by \dot{z}_d and, due to mass conservation, the following equations hold for the mass flow rate (see also Figure 41.b):

$$\dot{m} = cw\dot{z} = lw\dot{z}_d \quad (52)$$

where w indicates the device width (perpendicular to the flume wave propagation direction), z is the water column free surface displacement and \dot{z} its time derivative (free surface velocity).

In the computation of the terms in equation (51), the water volume can be ideally split into two parts, as highlighted in Figure 41.b:

$$E_k = \frac{1}{2} \rho_w wdl \dot{z}_d^2 + \frac{1}{2} \rho_w wc \left(a + \frac{l}{2} + z \right) \dot{z}^2 \quad (53)$$

$$E_g = \frac{1}{2} \rho_w g cw (a + z)^2$$

where the potential gravitational energy is set to zero in correspondence of the added mass duct middle axis, as shown in Figure 41.b (i.e., the average gravitational potential energy associated to the water within the duct and $e_{g,in}$ are null).

$$\dot{W}_{ext} = -p_a c w \dot{z} - \frac{K_l}{2} \dot{m} |\dot{z}_d| \dot{z}_d^2 \quad (54)$$

where p_a is the absolute pressure in the air chamber and K_l is a coefficient which accounts for pressure losses within the duct and in the various flow passages duct-collector, open sea-duct (here, $K_l=9$ was used). Being the only dissipative term within the energy balance, such term implicitly accounts also for all of the other losses, e.g. viscous losses in the DE material and losses due to sloshing of free surface within the OWC chamber.

As for the last term in equation (52), it can be rewritten as follows:

$$\dot{m} \left(\frac{p_{in}}{\rho_w} + e_{k,in} + e_{g,in} \right) = \dot{m} \left(\frac{\rho_w g (a + l/2) + p_w + p_{atm}}{\rho_w} + \frac{\dot{z}_d^2}{2} \right) \quad (55)$$

where p_w is the wave induced excitation pressure, whose expression is detailed later in this section. In the light of equations (52)-(55), equation (51) reduces to the following differential equation in z :

$$\ddot{z} = \frac{p_w - p - \rho_w g z - K_l \rho_w (c/l)^2 |\dot{z}| \dot{z} + \rho_w / 2 ((c/l)^2 - 1) \dot{z}^2}{\rho_w (dc/l + a + l/2 + z)} \quad (56)$$

where $p = p_a - p_{atm}$ is the relative air pressure within the chamber. Here, the air is supposed to undergo an adiabatic transformation, i.e.

$$p_a V_a^\gamma = p_{atm} (cwq)^\gamma \quad (57)$$

where the adiabatic air coefficient γ is taken equal to 1.4, whereas the air volume, V_a , resulting from the free surface and membrane displacements, is given by

$$V_a = cwq + \Omega_a - cwz, \quad (58)$$

with the volume subtended by the DE shell, Ω_a , being given by equation (27).

As regards the wave excitation pressure at the inlet of the OWC, we assume that it is given by

$$p_w = \frac{C_d}{l} \int_{-b}^{-a} \rho_w \frac{\partial \varphi(z, t)}{\partial t} dz = C_d \frac{\rho_w g H \sinh(kl)}{2kl \cosh(kb)} \cos(\omega \tau) \quad (59)$$

where

- $\varphi(z, t)$ is the undisturbed wave potential that is function of time and water depth:
- $\varphi(z, t) = \frac{gH}{4\pi f} \frac{\cosh(k(z+b))}{\cosh(kb)} \sin(2\pi ft)$ (60)
- with the wave number, k , at water depth b computed according to equation (49).
- C_d is a diffraction coefficient that depends on the amount of absorbed energy. If the whole amount of incoming energy is reflected, then $C_d=2$ [31]. In the present simulations, a fraction C_l of the incoming wave power P_w (see equation (47)) is dissipated due to viscous losses (described in equation (54)). Therefore, the value of $C_d=2-C_l$ is calculated by means of an iterative procedure, in which the value of C_l is recomputed at any run until convergence to steady state, as proposed in [31].
- The undisturbed wave height is rigorously equal to H at a water depth of 0.7m (i.e., upstream of the sloped beach). The same wave height has been assumed here (at a depth of $b=0.35$ m) basing

on the well-known shoaling condition (see e.g. sect. 3.3 of [33]), according to which the wave period is invariant along the wave train and the following identity holds:

$$c_g H^2 = \text{constant} \quad (61)$$

- which, solving equations (48)-(49) at intermediate water depths between the extreme values, shows that there are no significant height variations for the cases in exam.

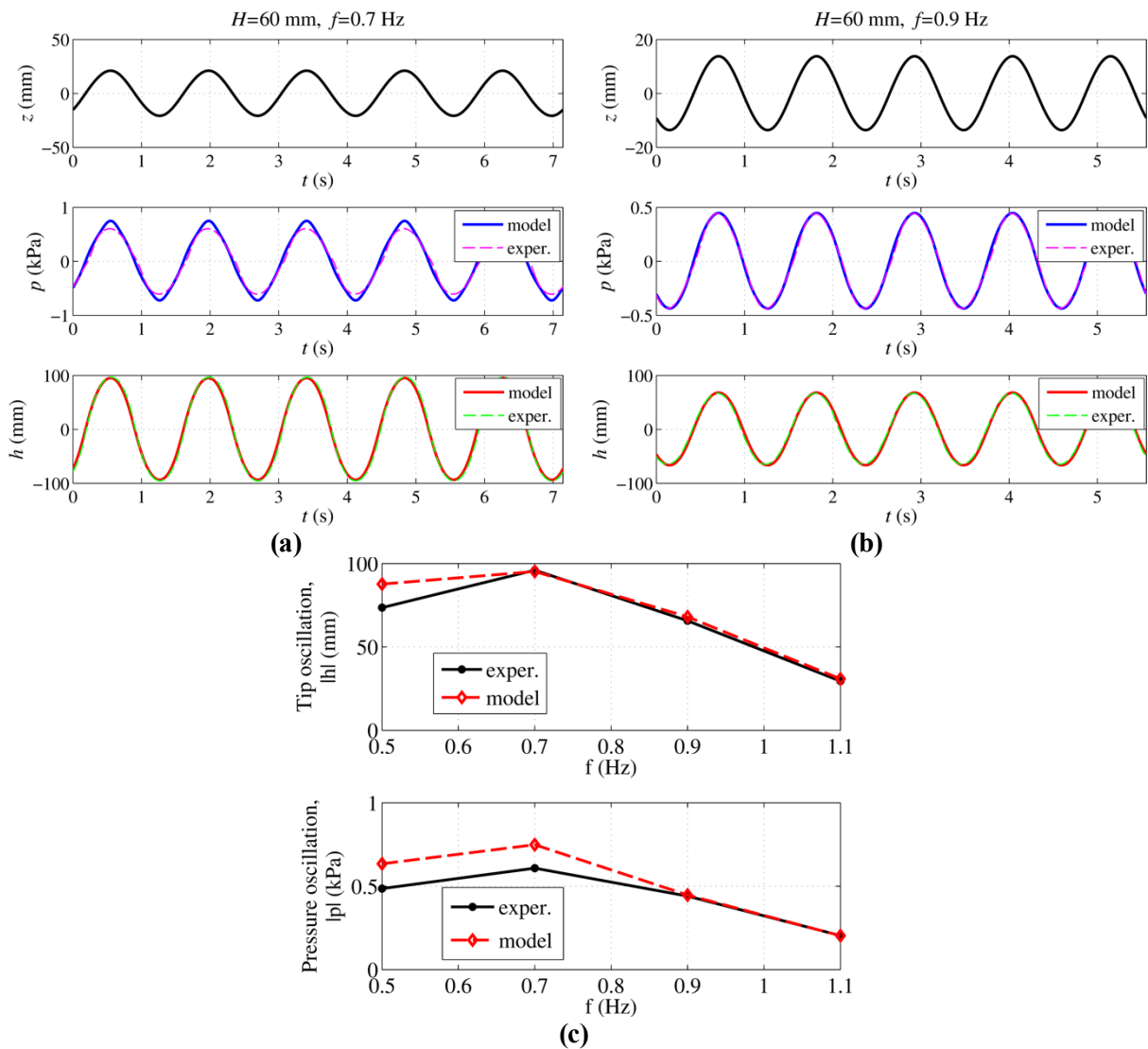


Figure 42 – (a) Time-series generated from the simulations on a Poly-OWC (in absence of CD-DEG electric activation) with $H=60\text{mm}$ and $f=0.7\text{Hz}$. (b) Amplitudes of oscillation of tip height, h , and relative pressure, p , for $H=60\text{mm}$ and different values of frequency: comparison between model and experiments.

It has to be observed that: 1) the present approach treats the OWC collector as bi-dimensional, which is a correct assumption as tests are accomplished in the wave-flume; 2) radiation phenomena are modeled roughly: added mass due to water motion in front of the duct inlet section is not kept into account, and wave excitation (equation (59)) is computed starting from the undisturbed wave potential, according to which radiation is modelled just by means of coefficient C_d .

Simulation results (based on equations (52)-(59)) and experimental results are compared in Figure 42. In particular, in Figure 42.a and Figure 42.b, steady-state time-series showing the model results for free surface displacement, z , relative pressure, p , and membrane tip elevation, h , are depicted with solid lines, for two

different sea conditions. Gauge pressure and tip elevation are also compared with experimental data (shown as dashed lines).

Water column displacement, z , was not measured during the experiments. Therefore, model validation can only be performed by the comparison of modelled pressure and tip height time-series.

Figure 42.c is a summarizing picture that, for a wave height of 60 mm and a set of four different excitation frequencies (0.5, 0.7, 0.9 and 1.1 Hz), shows the oscillation amplitudes of membrane tip and relative pressure obtained from the model and from experiments respectively.

Results show a rather good agreement between predictions and experiments. Most importantly, although the hydrodynamics is very simplified, the model is capable to predict the mechanical resonance of the system at a frequency of about 0.7 Hz.

In conclusion, models validation against experimental data provided good evidence of models reliability, showing that the CD-DEG electro-hyperelastic model is capable to predict the membrane pressure-deformation response (even in presence of electric activation), and it enables the implementation of complex multi-physics models (that also include the OWC hydrodynamics) that present good agreement with reality.

7 FLOWING MOORED OWC

In this section, we report results of experiments performed on a bottom-moored floating Tubular-Poly-OWC (T-Poly-OWC) based on the collector design proposed by the Spanish company Sendekia [34]. Experiments were carried out in February 2015.

The tested OWC collector is a 1:50 reproduction of the Sendekia concept, and it consists of an axisymmetric collector whose upper part is an hollow cylinder, with a bottom aperture (towards sea) with a peculiar patented shape, aimed at increasing the added mass of the water column to bring the device to resonance with typical sea waves. Such kind of collector can be employed in different arrangements, i.e., bottom-moored with tension legs (as in the present experiments), fixed to off-shore platforms or integrated in breakwaters.

Differently from the previous OWC concepts, whose hydrodynamics are essentially two-dimensional, this device exploits axial symmetry to capture/radiate waves from/to different spatial directions. Due to the intrinsic three-dimensional nature of this fluid-collector interaction, tests were carried out in the FloWave facility.

7.1 Experimental setup

The OWC collector has a lower buoyant element constituted by a hollow cylinder (with thin wall and inner diameter of 195 mm) and a convergent-divergent duct as lower aperture, whose shape has been proposed and optimized by the company Sendekia. On top of such buoyant chamber, a hollow polycarbonate cylinder (with the same inner and outer diameters of the lower collector) is located, having flanges on top to house the CD-DEG PTO. The device has been moored to the bottom of the wave tank and its draft has been set by means of four tension legs. A schematic of T-Poly-OWC concept is given in Figure 43.a, while Figure 43.b shows installation and operation of the experimental prototype.

Overall, the device has a draft of 150mm, the height of the emerged part (housing the air volume) is 300mm. In order to make the CD-DEG work in a configuration in which its capacitance variation is larger, the air chamber has been pressurized, i.e., the CD-DEG has been pre-inflated. In the equilibrium position, the gauge pressure, p , in the chamber, is about 0.35 kPa.

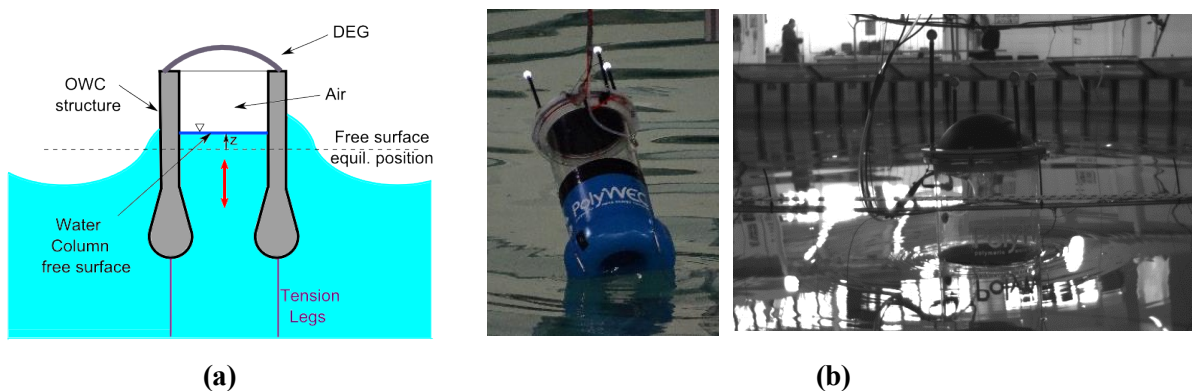


Figure 43 – (a) Schematic of T-Poly-OWC; (b) Pictures from FloWave experiments

A fully-functional CD-DEG prototype, with radius $e=97.5\text{mm}$, was mounted on the collector. The DEG was made of VHB 4905 elastomer with painted carbon grease electrodes made of MG-Chemicals 846 conductive grease. The CD-DEG has been set up superimposing 2 VHB layers, each with a thickness of 0.5mm (i.e., the unstretched membrane has a thickness $t_0 = 1\text{mm}$), with a pre-stretch $\lambda_p = 3.66$. According to Table 3, the corresponding full-scale dimensions for the pre-stretched CD-DEG are $e=4.9\text{m}$ and $t=0.19\text{m}$.

The same power electronics and sensing equipment described for the previous set of experiments have been employed (see section 6.1).

Membrane tip elevation, h , has been measured in post-processing via computer vision techniques presented in the following section. A high-speed camera with 100 fps speed has been employed to acquire video frames. Tip elevation data obtained from the acquired images have been properly corrected using six-DoF absolute positioning data obtained via optical tracking. That is, four reflecting

sensors have been positioned on top of the OWC collector; the six coordinates for the collector DoFs have been acquired at a speed of 120 fps.

As for the control electronics, as already discussed in section 6.1, the CD-DEG has been provided with an in-parallel capacitance, C_a , with the aim of increasing the maximum amount of energy convertible in a cycle, compatibly with the electric break-down limitation. A capacitance $C_a = 100\text{nF}$ was used in these experiments.

As in previous tests, the CD-DEG is controlled in a way that, during the electric activation phases, the DEG plus C_a form an isolated system (not exchanging charge with any external circuit). The parallel of the two capacitances is charged (to a target voltage, V_{in}) when the DEG capacitance is maximum (i.e., when the measured air pressure reaches a maximum), and it is discharged when the capacitance (and pressure) is minimum. Charging/discharging time is about 100 ms. The energy conversion cycle is depicted in Figure 44 (charging: OA'; constant charge on CD-DEG + C_a A'B'; discharging: B'O).

In these tests the membrane is pre-inflated; thus, it works with $h > 0$ during its whole operation, thereby performing one energy conversion cycle per wave period.

Electronics and control equipment are those described in section 5.1.

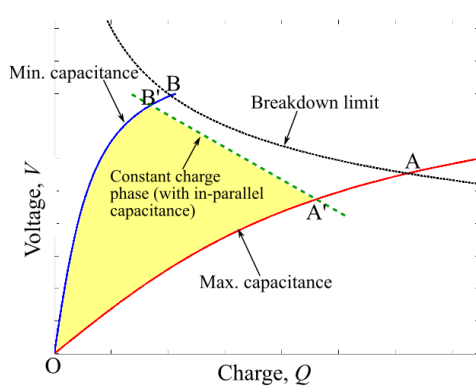


Figure 44 – Energy conversion cycle of the CD-DEG (OA'B'O) during a full-oscillation, compared with the maximal energy theoretical cycle (set by the material physical limitations).

7.2 Procedure and Data Processing

Experiments have been performed using a combination of wave parameters (frequency, f , and height, H). In this campaign, both regular (monochromatic) and irregular (panchromatic) waves were tested. As regards regular waves, results presented in this deliverable refer to the following parameters: $f = [0.29, 0.33, 0.36, 0.40, 0.45, 0.50, 0.60, 0.70, 0.80, 0.90, 1.0]\text{Hz}$, $H = [75, 100]\text{mm}$.

Irregular waves were generated using a multi-directional Joanswap spectrum [35] with the following peak frequencies and significant wave heights: $f_p = [0.45, 0.55]\text{Hz}$, $H_s = [100, 150]\text{mm}$.

The employed activation voltage was $V_{in} = 3500\text{V}$.

Each test was performed starting the FloWave from a fully flat condition. Data storage was started when the regime condition was reached. Each registered dataset consists of a few cycles without electric activation and a sequence of cycles with activation.

Pressure, p , and voltage, V , were acquired at 1kHz sampling frequency. Tip elevation, h , was obtained in post-processing from video data using computer vision techniques.

7.2.1 Identification of the CD-DEG tip height

During the test campaign, high frequency videos have been acquired to identify the time evolution of CD-DEG tip height. To this purpose, a high-speed camera with 100 fps speed has been employed.

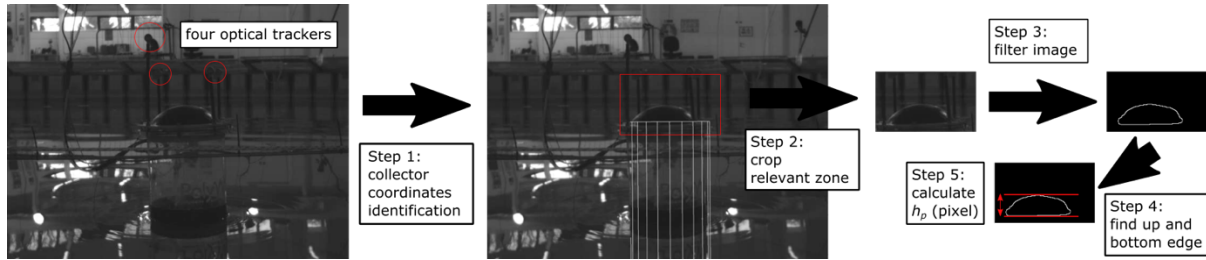


Figure 45 – The main steps for the tip identification procedure.

The identification procedure is divided in the following principal steps (see Figure 45):

1. The T-Poly-OWC collector is tracked by a commercial optical tracker, the OptiTrack® system. This system uses four reflecting sensors that have been positioned on top of the OWC collector in order to determine the six-DoF absolute position of the object. The OptiTrack system works at an acquisition speed of 120 fps.

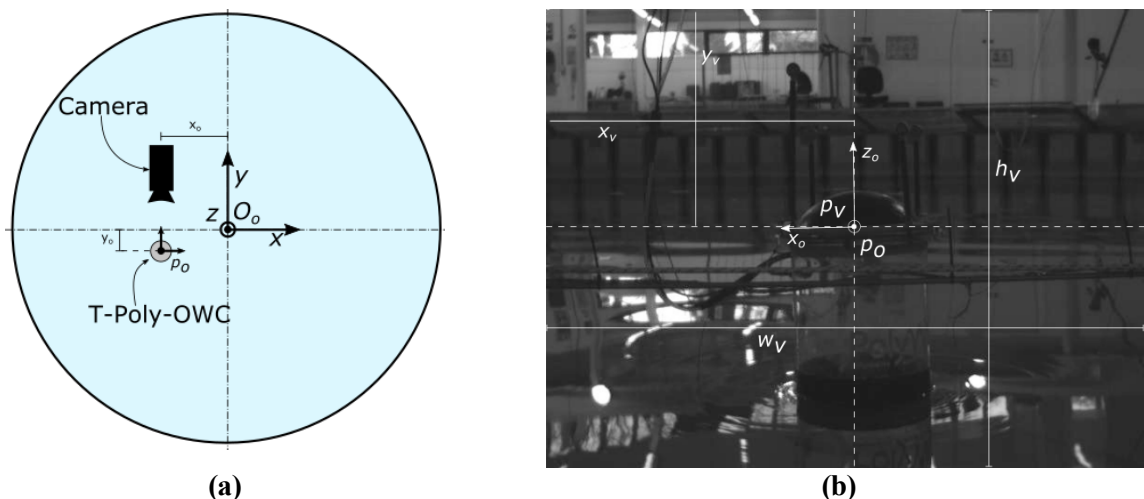


Figure 46 – (a) The position of the camera and T-Poly-OWC (p_{owc}) inside the circular FloWave tank, (b) The position of collector in the recording video.

In this phase the transformation function between the OptiTrack coordinate and the video coordinate is obtained and indicated with $T_{o \rightarrow v}$ (pixel/mm). Figure 46.a shows the position of T-Poly-OWC inside the FloWave, p_o , and Figure 46.b shows the position of the collector in the recording video. In this case, the video plane is parallel to (x, z) plane of the OptiTrack system; for this reason the transformation matrix uses only the x_o and z_o signal to get a collector position in pixel.

$$p_v(t) = T_{o \rightarrow v} p_o(t); T_{o \rightarrow v} = \begin{pmatrix} -s & 0 & 0 & \frac{w_v}{2} - x_o s \\ 0 & 0 & -s & \frac{h_v}{2} + z_o s \end{pmatrix}; p_v(t) = \begin{pmatrix} x_v \\ y_v \\ z_v \\ 1 \end{pmatrix}; p_o(t) = \begin{pmatrix} x_o \\ y_o \\ z_o \\ 1 \end{pmatrix}. \quad (62)$$

In equation (63): p_o (m) is the absolute position of the OWC; p_v (pixel) is the position of the collector inside the video; s is the scale factor of the video; (x_o, z_o) are the coordinates of the position of the collector when the collector is in the center of the video.

On the video a cylinder that overlaps on the buoy shape is drawn to check to correct time synchronization between video data and OptiTrack data, as well as the transformation matrix $T_{o \rightarrow v}$.

2. The image is cropped around the upper part of the cylinder around the p_v position.

3. The image is filtered to identify the contour of the membrane.

The procedure of filtering is composed by the following steps, and the image is indicated with I:

a. Calculation of the complement image with the Matlab[®] command:

`I = imcomplement(I);`

b. Application of a circular sector filter. This function highlights the chosen shape, in this case a circular sector indicated with (F).

`I = imopen(I,F);`

c. Conversion of the gray scale image into binary image, based on a threshold indicated with alpha, with alpha being chosen heuristically.

`I = im2bw(I, alpha);`

d. Application of an edge finder filter to the binary image. The method chosen is “Canny”, that finds edges by looking for local maxima of the gradient of I.

`I = edge(I, method);`

4. The upper and lower edges in the image are found, which makes it possible to calculate h_p (in pixel);

5. Based on h_p , the transformation $T_{v \rightarrow o}$ is used to calculate h (m).

7.2.2 Energy harvested estimate

In this application, electric activation dramatically affects the CD-DEG oscillation amplitude. That is, CD-DEG oscillation amplitude is significantly different (generally lower) when electric activation is present, as the latter contributes to damp the system. Therefore, a direct assessment of viscous loss, ζ (see Chapter 5), is not possible in this case since it was based on the assumption of a reduced influence of the electrical activation on the dynamic response. While in previous experiments mechanical viscous loss (in presence of electric activation) was assumed equal to that measured in the absence of electric activation, this hypothesis cannot be employed here, due to the significantly different oscillation amplitude. As for the remaining quantities, E_{hc} , ϕ and η were computed in a similar way as described in sections 5.2. In particular, electric energy harvested in a cycle, E_{hc} , is computed as in equation (43), assuming variable DEG capacitance during the charging/discharging phases. Notice that, in these tests, DEG capacitance can vary both during the charging and discharging phases (see also Figure 44).

As regards the other parameters, ϕ is defined in equation (37), and η defined in equation (38).

The voltage ratio, ϕ , here does not play the role of a figure of merit, due to the presence of the in-parallel capacitance. In fact, large energy amounts may be converted even if ϕ is rather small (e.g., if C_a was very large).

Mechanical work, E_m , positively done by the water surface on the PTO (air + CD-DEG) is computed as in equations (38)-(39) basing on those cycles in which the DEG is electrically activated.

Given the definition of mechanical-to-electrical energy efficiency, η , it comes that a fraction $1-\eta$ of the mechanical work provided by the water column is not converted into electricity as it is partially dissipated (by elastomer viscoelasticity and other effects) and partially returns to water during the membrane return phase. Nevertheless, from the available data it is not possible to deduce the ratio ζ of energy which is dissipated by material viscosity.

7.3 Results

This section reports results of wave-tank tests data post-processing. Performance parameters are calculated over a range of sea conditions. Regular waves are considered first, and the power matrix for the T-Poly-OWC prototype in monochromatic waves is obtained. Successively, operation in irregular waves is considered: a verification of the effectiveness of the operation and control of the CD-DEG in panchromatic sea conditions is carried out.

7.3.1 Regular waves tests

In Figure 47.a and Figure 47.b, time-series describing the CD-DEG dynamics are reported for two monochromatic experiments featuring $f = 0.8\text{Hz}$, $H = 100\text{mm}$, and $f = 0.4\text{Hz}$, $H = 75\text{mm}$ respectively. In both cases, activation voltage is $V_{in} = 3500\text{V}$. In both figures, the top plot is for relative air pressure, p , within the chamber, middle plot is for the tip elevation, h , and bottom plot is for the voltage on CD-DEG and C_a .

The following conclusions can be drawn:

- CD-DEG operation is quite effective, with the voltage on the DEG showing a net increase during activation phases. Nonetheless, it is clear (particularly from Figure 47.b) that electric activation is responsible for a further increase in tip height, and consequent initial decrease in voltage (blue insets in Figure 47.b). This happens because large electric field employed in these tests are responsible for large Maxwell stresses that provoke the CD-DEG to become more compliant when charged.
- Electric activation has a perceivable effect on T-Poly-OWC dynamics. Indeed, Figure 47.a shows that electric activation is responsible for a great reduction of the membrane oscillation amplitude (i.e., the WEC is over-damped by the PTO), while in different sea conditions (see, e.g., Figure 47.b) oscillation amplitude is marginally affected by electric activation. Future works may include an optimization of the control strategy, aimed at optimizing the PTO damping, eventually introducing a prediction of incoming waves.

Plots describing the T-Poly-OWC performance parameters in the range of tested regular waves are in Figure 48. In particular, Figure 48.a is for the mean electric energy harvested per cycle, Figure 48.b is for the mean voltage amplification ratio, Figure 48.c is for the mean electro-mechanical efficiency (i.e., the percentage of mechanical work made by the water column on the air during expansion which is turned into electricity), and Figure 48.d reports the electrical mean power output.

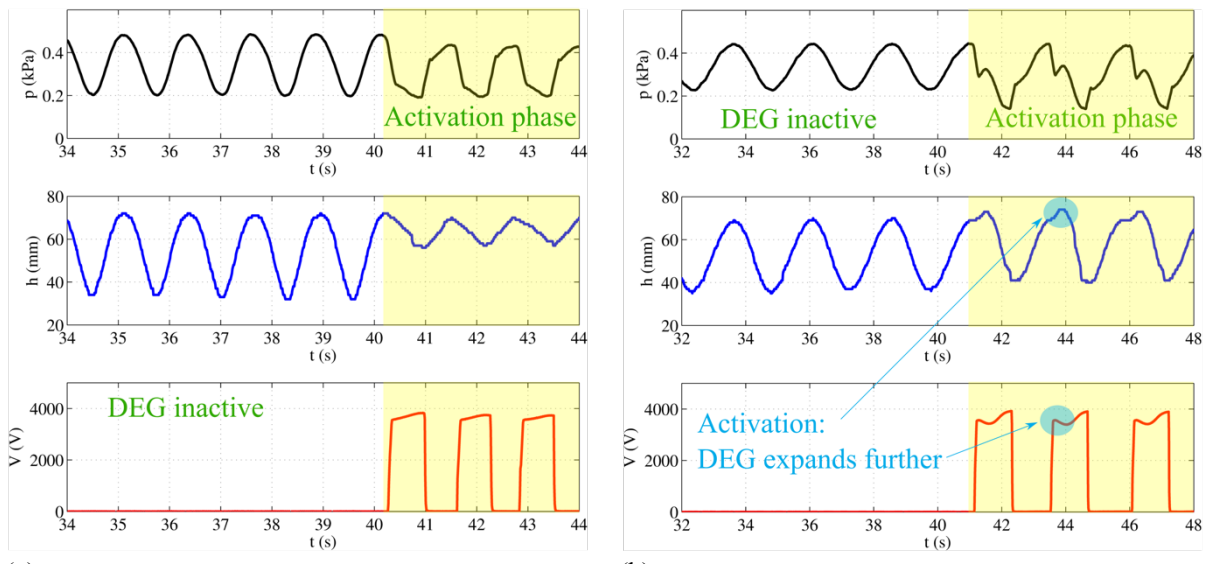


Figure 47 - Gauge pressure, tip height and CD-DEG voltage time-series for two monochromatic experiments: (a) $f = 0.8\text{Hz}$, $H = 100\text{mm}$ $V_{in} = 3500\text{V}$; (b) $f = 0.4\text{Hz}$ $H = 75\text{mm}$ $V_{in} = 3500\text{V}$. Highlighted areas refer to phases in which the DEG is cyclically charged/discharged.

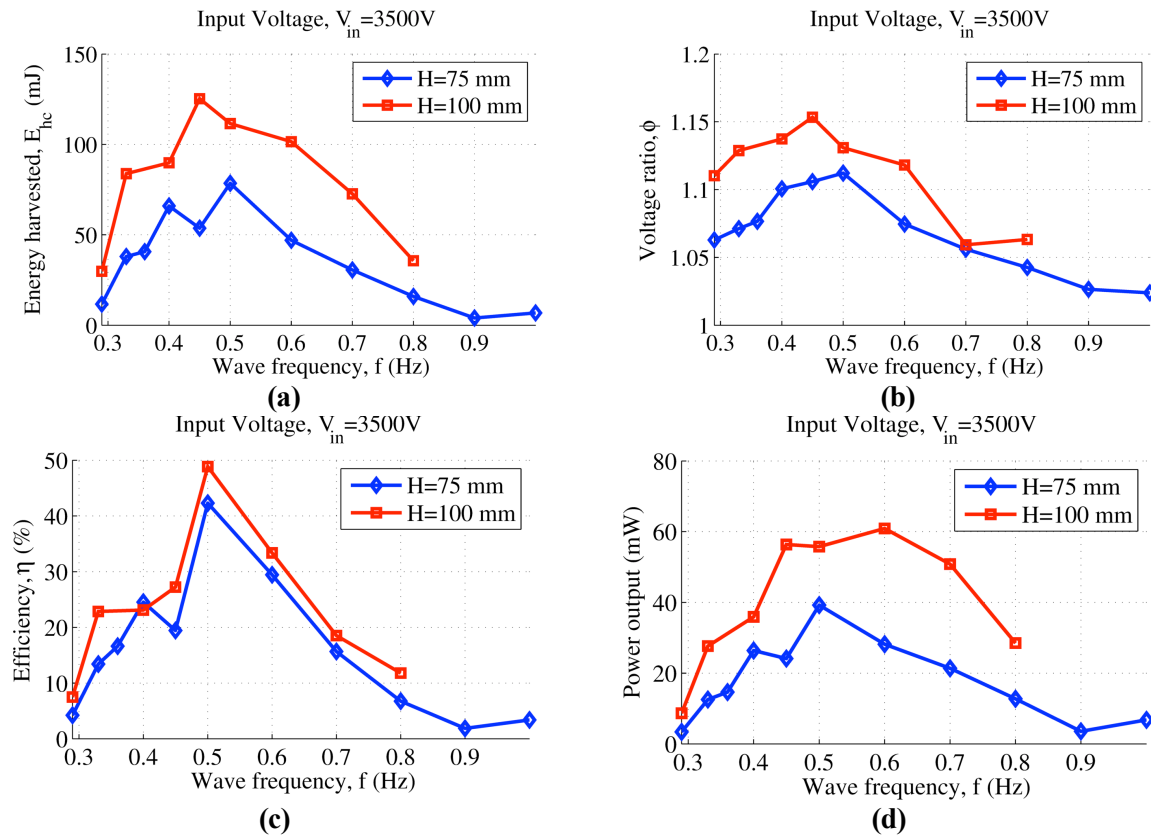


Figure 48 - Experimental assessment of the Poly-OWC prototype: energy harvested per cycle (a), voltage amplification ratio (b), conversion efficiency (from water column work to electrical) (c), and mean electrical power output (d) as function of water wave frequency, f , and height, H .

A monotonic trend of the measured variables with respect to f and H has not been obtained in this case. This is probably due to the collector displacements, which made the device behavior less repeatable than in the previous sets of tests and introduced relevant hydrodynamic dissipations.

Nonetheless, the following can be observed:

- Voltage ratio, ϕ , and harvested energy, E_{hc} , are generally larger when incoming waves are higher, as a consequence of the larger incoming mechanical energy.
- At high frequencies, performance (in terms of E_{hc} and η) tends to decrease. This is mainly due to dissipations and control. Viscous dissipations in the DE material rise with frequency: parameter η , which expresses the amount of work (made by the water piston) efficiently turned into electricity, predictably drops as the percentage amount of viscous dissipated energy rises. Moreover, the controller is such that the closure time of the switch controlling the DEG charging is the same at any frequency. That is, the percentage time (over a cycle) in which the switch is closed (and DEG is kept at constant potential) is larger at high frequencies, with a consequent reduction of the useful time interval for energy generation.
- The trends of performance parameters cannot be trivially explained in terms of resonance and natural frequency of the DEG. Indeed, if the purely oscillating mechanical behavior (without electric activation) of the T-Poly-OWC is observed, it is found that frequency-dependent peaks in the oscillation amplitudes of pressure and tip height are not present (see also section 7.4.2 and Figure 53).
- Conversion efficiencies (Figure 48.c) are rather higher than those of the previous tests. However, these efficiencies are not always representative of a larger capture factor of the device. In fact, tip height and pressure time-series reveal that electric activation is sometimes responsible for an “overdamping” of the WEC (see, e.g., Figure 47.a): although the water-column-to-electric energy

conversion efficiency is high, in those cases the overall wave-to-wire efficiency is poor. An improvement may be obtained by reducing hydrodynamic losses, setting the activation voltage, V_{in} , to an optimized value, or changing the control strategy of the DEG.

- As shown by Figure 48.d, the maximum power output is about 60mW (corresponding to 54kW for the full-scale equivalent system). This power output is small compared to that of previous experimental tests; this demonstrates that, although the conversion efficiency of the PTO is rather good, the WEC is overdamped due to hydrodynamic dissipations or excessive PTO damping.
- One thing that should be underlined is that in the case of the resonant Poly-OWC presented in section 6 the controller was able to generate power twice for each wave period, practically doubling the converted power. In the case of the T-Poly-OWC, this was not possible since deflation of the membrane was not allowed due to stability issues of the available Sendekia collector that was featuring not enough buoyancy. Nonetheless, a properly designed collector (with enough buoyancy to enable inward expansion of the CD-DEG) could make it possible to reach much larger value of harvested power (almost two times the ones that were measured here). Moreover, as for the other tested PolyOWC devices, a larger scale prototype could make it possible to employ less dissipative materials such as silicone elastomers or synthetic/natural rubbers.

7.3.2 Irregular waves tests

Figure 49 shows results for some tens of seconds of operation of the T-Poly-OWC in irregular waves, for two different sea states. Plots refer to phases during which the DEG is cyclically activated and deactivated. Differently from the smooth and regular response measured in monochromatic sea-states (see for instance in Figure 47), in this case the CD-DEG tip oscillation amplitude visibly varies from cycle to cycle. As a consequence, the PTO exhibits a differently efficient response in different cycles.

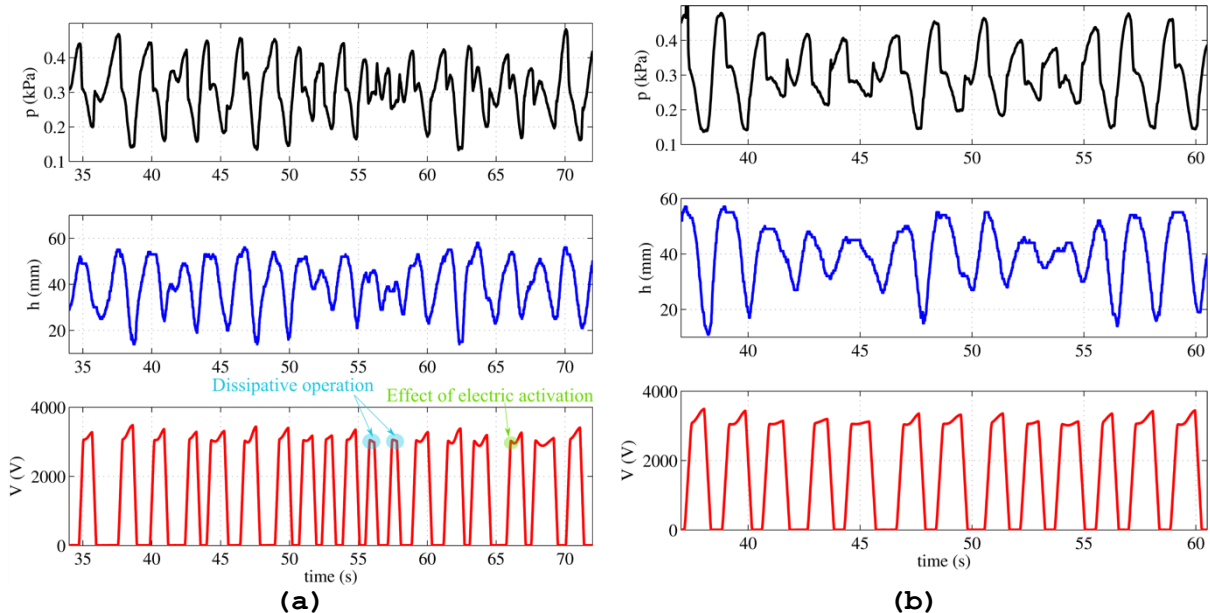


Figure 49 - Gauge pressure, tip height and CD-DEG voltage time-series for two polychromatic (Joanswap spectrum) experiments: (a) $f_p = 0.45\text{Hz}$, $H_s = 100\text{mm}$ $V_{in} = 3500\text{V}$; (b) $f_p = 0.55\text{Hz}$ $H_s = 100\text{mm}$ $V_{in} = 3500\text{V}$.

In general, the following can be stated:

- In most of the cycles, the CD-DEG voltage has an increasing trend during the activation phase, which means that it generates electrical energy. This demonstrates that the implemented control is, in average, rather effective.
- As already mentioned in section 7.3.1 and Figure 47.b, in some cycle, the DEG expands during charging due to the effect of electrostatic stresses: this results in an initial decreasing trend of the voltage, followed by a phase with the increasing voltage (see green inset in Figure 49.a).

Although, in these cases, the CD-DEG initially behaves as an actuator (thus consuming electrical energy), its overall electric energy balance during the cycle is positive (and operation is effective).

- In some cycles (particularly, when the tip elevation or local tip amplitude is small), the voltage decreases (or does not increase significantly) during the CD-DEG activation phase (see blue insets in Figure 49.a), i.e., the PTO is not generating energy (but it is dissipating the fed activation energy) during that cycle. The control strategy may be refined by preventing the CD-DEG activation when incoming waves are too small.

T-Poly-OWC has been tested in a restricted range of sea states, and the resulting power outputs are reported in Figure 50. Horizontal axis in the figure lists the tested sea states, identified by their peak frequency, f_p , and significant wave height, H_s . Sea States (SS) 1 to 4 are in order of increasing carried power. The lower black curve represents the mean power, calculated from the overall energy balance on the entire experiment length. The upper red curve shows instant peak power values, computed on the best sequence of three successive cycles.

Mean powers up to 20mW where measured, with peak powers of almost 40 mW (corresponding to a full scale power of 35-40kW).

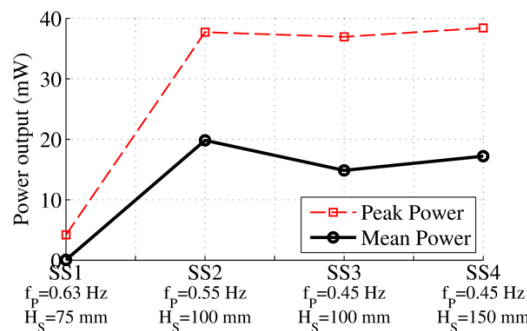


Figure 50 – Mean power output (computed on the whole experiment time) and peak power (computed on a sequence of three successive cycles) of the T-Poly-OWC prototype in irregular waves. Sea states on the X axis are in order of increasing carried wave power.

In conclusion, tests on T-Poly-OWC produced quite positive outcomes, especially because the effectiveness of control and conversion in irregular waves was proved. Nonetheless, it is expected that an improvement in the T-Poly-OWC performance would be achieved by: 1) keeping the collector fixed rather than bottom-moored, in order to reduce hydrodynamic dissipation and vortex-shedding due to large collector displacements; 2) testing at a larger scale than 1:50, in order to reduce the ratio between viscous and inertial/gravitational forces; 3) using more performing (namely, less dissipative) DE materials (like natural rubber or silicone elastomers) that, due to their intrinsic large stiffness, can be employed only on larger scale prototypes.

7.4 Model validation

In this section, we present a validation of T-Poly-OWC hydro-electro-hyperelastic models. Following the approach of the previous sections, validation of single submodels is provided. That is, CD-DEG electro-hyperelastic model is validated first, using pressure measurements as input to the model and checking tip elevation and voltage time-series against experimental results. Once the mechanical model of CD-DEG has been verified, a coupled hydro-elastic model is validated by comparing predicted pressure and tip height time-series (for a given combination of sea-states) with experiments.

7.4.1 CD-DEG electro-hyperelastic model validation

In this section, the CD-DEG model presented in [22] and resumed in section 5.4.1 is validated by using the measured air pressure time-series as input variable into the model and comparing tip height results with experimental data.

The following hyperelastic parameters are used: $a=0.65$ MPa, $I_m=120$ (unloading curve in Figure 10.a).

Results are in Figure 51. The time-series considered in these plots are those previously described in Figure 47.

Theoretical predictions (dashed lines in the plots) are obtained using the measured pressure time profile and activation voltage, and assuming that, in the active phase between charging and discharging, the overall charge on CD-DEG + C_a is constant. Equation (26) is used to estimate the DEG capacitance.

Comparisons of theoretical predictions and experimental data confirm that, although viscous losses have been neglected, the model is very accurate. The same conclusions of section 6.4.1 can then be drawn: hyperelastic parameters fitting is very effective; loss of charge (due to electrical conductivity of the material and charge dispersions through air) has a minor effect here (otherwise, theoretical predictions on voltage profiles would have been significantly different from those measured in the experiments).

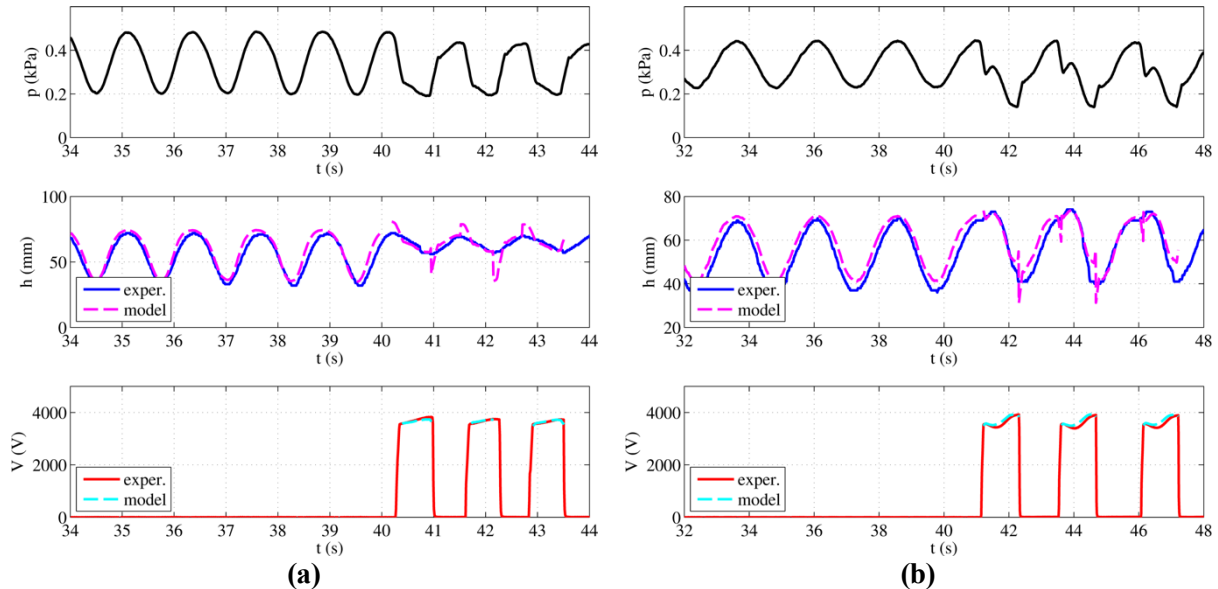


Figure 51 – CD-DEG model validation against experimental time-series previously shown in Figure 47. Solid lines are experimental data, while dashed lines are model-based predictions. The two pictures refer to the following test conditions: (a) $f = 0.8\text{Hz}$, $H = 100\text{mm}$ $V_{in} = 3500\text{V}$; (b) $f = 0.4\text{Hz}$ $H = 75\text{mm}$ $V_{in} = 3500\text{V}$.

Major differences can be seen in correspondence of charging/discharging instants. That is, the quasi-static model assumes instantaneous charging/discharging, which should result in a sudden variation of the tip height. Although this variation also occurs in the experiments (see, for instance, Figure 47.b), tip height instant variations due to activation/deactivation are smoother and smaller. This happens because phenomena occurring in a time comparable to that of electric switches closure (~ 100 ms) are smoothed by CD-DEG inertia and viscoelasticity.

As a further validation of the CD-DEG capacitance expression (26), experimental capacitance curves are reported in Figure 52 and compared to the theoretical expression. Such experimental curves were obtained through current measurements in inflation-deflation tests in which a high-frequency time-varying sinusoidal voltage was applied between the CD-DEG electrodes. The comparison shows a good agreement of the predicted capacitance with respect to measurements, even though the theoretical expressions provide a slight overestimate.

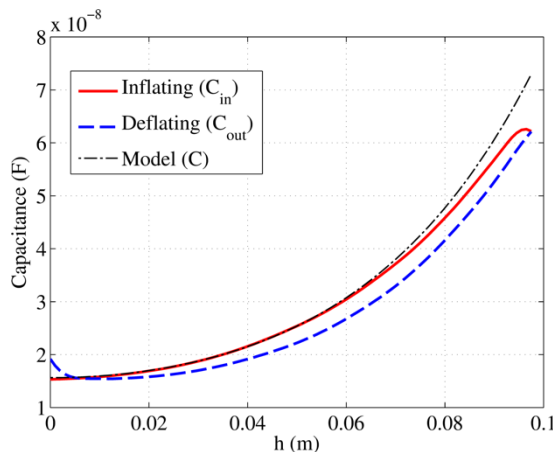


Figure 52 – Measured capacitance as a function of tip: inflating membrane (solid curve), deflating membrane (dashed), theoretical model (dash-dot line).

7.4.2 Poly-OWC elasto-hydrodynamic model validation

In this section, we present a validation of a hydrodynamic model for the small-scale Sendekia collector coupled with the mechanical model of the CD-DEG that has been verified in the previous section. The aim of the presented validations is to asses the validity of individual sub-models, identifying which of the two models is responsible for the greatest uncertainties. Following this approach, since the validation of the electro-mechanical model of the DEG has been described in section 7.4.1, here validation is performed on the OWC collector + mechanical membrane model only without accounting for electric activation. A validation of the hydrodynamic model alone is here not possible, as data have been registered only on functional T-Poly-OWC, with elastomeric PTO already mounted.

The OWC collector model used here is that described in PolyWEC D1.2 [1] and in [24], and it relies on potential flow theory assumption and BEM hydrodynamic data. Although the OWC collector is bottom moored and it is allowed to displace with respect to its reference equilibrium position, here it is assumed that the collector does not move and the only DoF is the relative displacement of the water column free surface within the OWC chamber. This hypothesis is motivated by the mooring type, i.e. tension legs, which, supposedly, keep the collector in place allowing very small amplitude collector displacements.

Using such approach, the equation of motion describing the free surface displacement, z , is:

$$M_\infty \ddot{z} + \int_0^t K(\tau - \xi) \dot{z}(\xi) d\xi + B_v \dot{z} + \rho_w g S \cdot z = -pS + F_e(\tau). \quad (63)$$

In equation (64): M_∞ is the water column added mass at infinite frequency; the radiation convolution integral accounts for frequency-dependent added mass and radiation damping; B_v is a linearized viscous damping; S is the OWC collector inner cross-section; F_e is the wave excitation force. Hydrodynamic parameters have been computed using WAMIT and are the same used in [24], scaled with the coefficients of Table 1. Details on the implementation of the model, including the approximation of the convolution integral and the mathematical form of $F_e(\tau)$ can be found in [1] and [24].

In Figure 53.a, simulation results (based on equation (63)) are reported showing the free surface displacement, z , relative pressure, p , and membrane tip elevation, h , time-series for a Poly-OWC with the dimensions of the prototype in exam in presence of incoming monochromatic waves with $H=100\text{mm}$ and $f=0.5\text{Hz}$.

As in section 6.4.2, validation has been addressed by comparing theoretical data with measured pressure and membrane tip elevation only.

Comparison of theoretical predictions with experiments are shown in Figure 53. In the pictures, a variety of regular waves with different frequencies and height H equal to 75mm (Figure 53.b) and 100mm (Figure 53.c) respectively are considered. The plots compare minima and maxima of the steady-state time-series of gauge pressure and tip height (notice that, being the membrane pre-inflated, oscillations are biased above the zero). Notice that, in the plots, each bullet corresponds to a different sea state and simulation/experiment.

Theoretical and experimental data present, in general, a satisfactory agreement, especially at low frequencies. At higher frequencies (0.7-0.8Hz) oscillations predicted by the model are larger than those measured in practice, i.e., the model foresees a resonant behavior in correspondence of such high frequencies, while the real behavior is rather frequency-independent. Possible reasons for this mismatch are:

- Viscous effects not accounted in the presented model;
- The 1 DoF model compares with a practical scenario in which oscillations of the collector actually occur even in different DoFs (even though these are limited by tension legs extensibility).

In order to properly validate the hydrodynamic model, in the future it will be considered to install the collector fixed to a rigid structure rather than moored to the bottom via tension legs.

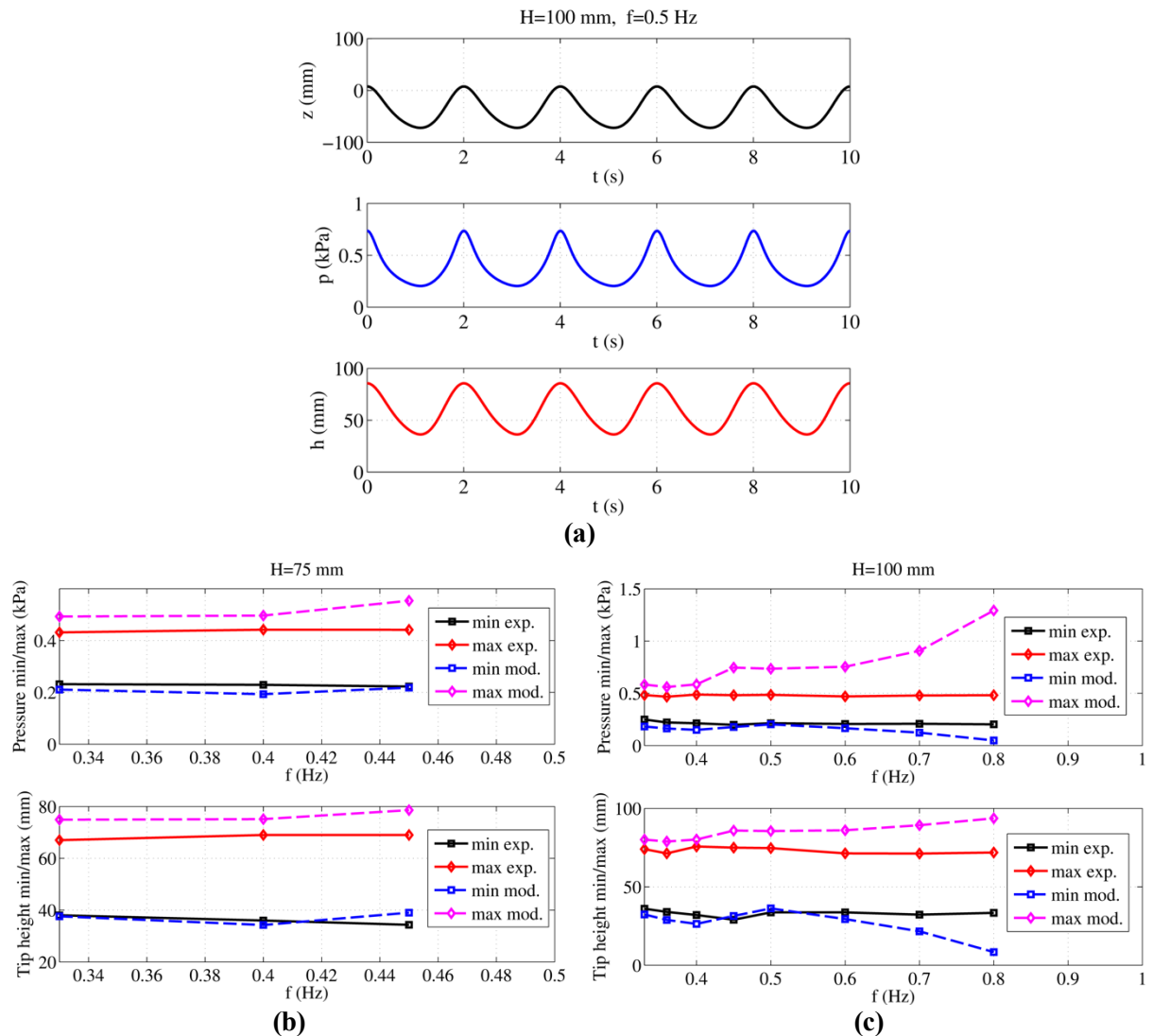


Figure 53 – (a) Time-series generated from the simulations on small-scale T-Poly-OWC (in absence of CD-DEG electric activation) with $H=100\text{mm}$ and $f=0.5\text{Hz}$. **(b)** Minima and maxima of pressure and tip height oscillation (experimental data vs model data) with incoming regular waves with $H=75\text{mm}$ and different wave frequencies. **(c)** As in (b) but with a wave with $H=100\text{mm}$.

8 CONCLUSIONS AND FUTURE WORKS

In this report, experimental results from first PolyWEC experimental campaigns are presented, elaborated, and discussed.

Reported results fulfill the following objectives:

- Scaling laws for PolyWEC devices have been deduced. A set of scaling rules for the dimensions of different types of DE PTOs has been identified, which allows to set up wave-tank tests in Froude similarity conditions.
- Experiments on three different prototypes of fully-functional Poly-OWC, with CD-DEG PTO, have been performed, showing the effectiveness of DEs as generators for WECs.
- Hydro-electro-hyperelastic models proposed within the project have been validated against experimental data, finding a good agreement.

Besides a first set of dry-run lab tests on a CD-DEG prototype, three sets of tank tests were presented, based on the following three devices:

- Fixed-structured OWC with non-optimal collector. This device was the first to be tested within PolyWEC: the aim was to demonstrate the capability of DEGs to convert wave energy; therefore, the attention was not focused on the optimization of the OWC collector and the overall system was found not to resonate with the incoming waves chosen for the experimental testing. The device was tested in a wave flume facility (at UEDIN), and it had a scale of approximately 1:50 with respect to a hypothetic full-scale Poly-OWC device.
- Fixed- structured OWC with added-mass duct. Basing on the previous experiment, the OWC collector was optimized by means of a horizontal submerged added-mass duct, aimed at increasing the water column inertia, thus bringing the WEC to resonance. As a result, the prototype was found to resonate with incoming regular waves with frequencies in the range of 0.5Hz and 0.7Hz. The device was tested in the same wave flume facility (at UEDIN), and it had a scale of approximately 1:40. Although the employed DE material was non-optimazized for DEG application, the device was able to produce a power output of approximately 900mW that corresponds to a full-scale power of 365kW.
- Tension-leg-moored Tubular Poly-OWC. This device was based on a floating axial-symmetric collector proposed by the company Sendekia. Such collector has a peculiar submerged aperture towards sea water that is aimed at increasing added mass. The device was tested in the FloWave facility in Edinburgh, in a scale of 1:50, both in regular and irregular waves.

All of the experimental data have been extensively reported and discussed in this deliverable, and performance parameters have been defined.

Results confirm the potential of DEs as PTOs for WECs and the effectiveness of the chosen control strategies.

Future works will be focused on:

- Testing of a larger-scale Poly-OWC prototype. This will be very important since: 1) direct measurement of larger power outputs will be easier and less affected by data post-processing uncertainties; 2) frequency-dependent behavior of the WEC and resonance will be more visible, as the ratio between inertial forces and viscous forces will be greater; 3) for the same reason, validation of hydrodynamic models will be more accurate. A target larger-scale device may be a T-Poly-OWC, with a scale of about 1:30 (power output in the range of 1W and 10W), to be tested in the FloWave facility. In order to improve the T-Poly-OWC performance with respect to the last set of tests, the device could be tested fixed to a platform rather than bottom-moored via tension legs.
- Testing of direct-contact PolyWECS. To date, wave tank tests have been performed on different versions of Poly-OWC. In the future, other concepts will be tested. Of particular interest will be the testing of direct-contact DE-based WECs (preliminary tests have already been carried out that confirmed their potentialities, see Figure 54). Indeed, these kind of WECs are particularly new, unconventional and promising (due to the very reduced number of moving parts); however, given

the highly non-linear nature of their fluid-structure interaction, they require intensive experimental work to be properly characterized.



Figure 54 – Preliminary mechanical tests on a concept of direct-contact PolyWEC.

9 REFERENCES

- [1] M. Fontana, R. Vertechy, G. Moretti, D. Forehand, and D. Ingram, “PolyWEC Deliverable D1.1 - Architectures and material-property specifications for first- and second- generation PolyWECS,” 2013.
- [2] G. Moretti, R. Vertechy, G. P. Rosati Papini, M. Fontana, D. Forehand, and M. Alves, “PolyWEC Deliverable D1.2 - Novel non-linear multi-physics continuum models,” 2015.
- [3] B. Teillant, M. Vicente, K. Monk, T. Simas, G. Moretti, M. Fontana, R. Vertechy, D. Forehand, C. Thomson, G. Harrison, and A. Raggi, “PolyWEC Deliverable D5.3 - Preliminary assessment and exploitation of PolyWECS,” 2015.
- [4] A. A. E. Price, “New Perspectives on Wave Energy Converter Control,” University of Edinburgh, 2009.
- [5] M. Fontana, R. Vertechy, A. Raggi, and A. Pitamorsi, “PolyWEC Deliverable D3.1 - Small-scale first generation PolyWEC unit devices,” 2014.
- [6] B. Holmes, *Tank Testing of Wave Energy Conversion Systems*. 2009.
- [7] K. Ruehl and D. Bull, “Wave Energy Development Roadmap: Design to commercialization,” in *2012 Oceans*, 2012.
- [8] T. McKay, B. O’Brien, E. Calius, and I. Anderson, “An integrated, self-priming dielectric elastomer generator,” *Appl. Phys. Lett.*, vol. 97, no. 6, 2010.
- [9] C. Keplinger, T. Li, R. Baumgartner, Z. Suo, and S. Bauer, “Harnessing snap-through instability in soft dielectrics to achieve giant voltage-triggered deformation,” *Soft Matter*, vol. 8, no. 2, p. 285, 2012.
- [10] G. Moretti, M. Fontana, and R. Vertechy, “Parallelogram-shaped dielectric elastomer generators: Analytical model and experimental validation,” *J. Intell. Mater. Syst. Struct.*, vol. 26, no. 6, pp. 740–751, Dec. 2014.
- [11] G. A. Holzapfel, *Nonlinear solid mechanics*. Chichester, UK: Wiley, 2000.
- [12] G. Moretti, M. Fontana, and R. Vertechy, “Modeling of a Heaving Buoy Wave Energy Converter With Stacked,” in *ASME 2014 Conference on Smart Materials, Adaptive Structures and Intelligent Systems (SMASIS2014)*, 2014.
- [13] G. Moretti, M. Fontana, and R. Vertechy, “Modeling and control of lozenge-shaped dielectric elastomer generators,” in *ASME 2013 Conference on Smart Materials, Adaptive Structures and Intelligent Systems*, 2013, pp. 1–10.
- [14] G. Berselli, R. Vertechy, G. Vassura, and V. Parenti-Castelli, “Optimal Synthesis of Conically Shaped Dielectric Elastomer Linear Actuators: Design Methodology and Experimental Validation,” *IEEEASME Trans. Mechatronics*, vol. 16, no. 1, pp. 67–79, 2011.
- [15] G. Moretti, M. Fontana, and R. Vertechy, “Model-based design and optimization of a dielectric elastomer power take-off for oscillating wave surge energy converters,” *Meccanica*, 2015.
- [16] G. Moretti, D. Forehand, R. Vertechy, M. Fontana, and D. Ingram, “Modeling of an Oscillating Wave Surge Converter With Dielectric Elastomer Power Take-Off,” in *Proceedings of the ASME 2014 33rd International Conference on Ocean, Offshore and Arctic Engineering OMAE*, 2014, p. V09AT09A034.
- [17] R. Vertechy, G. P. Rosati Papini, and M. Fontana, “Reduced Model and Application of Inflating Circular Diaphragm Dielectric Elastomer Generators for Wave Energy Harvesting,” *J. Vib. Acoust.*, vol. 137, no. 1, 2014.
- [18] J. Zhu, S. Cai, and Z. Suo, “Resonant behavior of a membrane of a dielectric elastomer,” *Int. J. Solids Struct.*, vol. 47, no. 24, pp. 3254–3262, 2010.
- [19] A. F. O. Falcão and J. C. C. Henriques, “Model-prototype similarity of oscillating-water-column wave energy converters,” *Int. J. Mar. Energy*, vol. 6, no. September 2015, pp. 18–34, 2015.
- [20] D. Rockwell and E. Naudascher, “Review—Self-Sustaining Oscillations of Flow Past Cavities,” *J. Fluids Eng.*, vol. 100, no. 2, p. 152, Jun. 1978.
- [21] M. Righi, R. Vertechy, and M. Fontana, “Experimental Characterization of a Circular Diaphragm Dielectric Elastomer Generator,” in *Proceedings of the ASME 2014 Conference on Smart Materials, Adaptive Structures and Intelligent Systems. SMASIS14*, 2014.
- [22] G. Pietro Rosati Papini, R. Vertechy, and M. Fontana, “Dynamic model of dielectric elastomer

- diaphragm generators,” in *ASME 2013 Conference on Smart Materials, Adaptive Structures and Intelligent Systems*, 2013, pp. 1–9.
- [23] R. Vertechy and M. Fontana, “Electromechanical characterization of a new synthetic rubber membrane for dielectric elastomer transducers,” in *SPIE Smart Structures and Materials+ Nondestructive Evaluation and Health Monitoring*, 2015.
- [24] G. Moretti, G. Pietro Rosati Papini, M. Alves, M. Grases, R. Vertechy, and M. Fontana, “Analysis And Design Of An Oscillating Water Column Wave Energy Converter With Dielectric Elastomer Power Take-Off,” in *Proceedings of the ASME 2015 34th International Conference on Ocean, Offshore and Arctic Engineering OMAE*, 2015.
- [25] D. Ingram, R. Wallace, A. Robinson, and I. Bryden, “The design and commissioning of the first, circular, combined current and wave test basin.” *Flow3D.Com*, 2014.
- [26] I. G. Morrison and C. A. Greated, “Oscillating Water Column Modelling,” *Coastal Engineering Proceedings*, vol. 1, no. 23. 1992.
- [27] R. Pelrine, R. Kornbluh, J. Eckerle, P. Jeuck, S. Oh, Q. Pei, and S. Stanford, “Dielectric elastomers: Generator mode fundamentals and applications,” *Proc. SPIE 4329, Smart Struct. Mater.*, vol. 42, pp. 148–156, 2001.
- [28] J. Huang, S. Shian, Z. Suo, and D. R. Clarke, “Maximizing the Energy Density of Dielectric Elastomer Generators Using Equi-Biaxial Loading,” *Adv. Funct. Mater.*, vol. 23, no. 40, pp. 5056–5061, Oct. 2013.
- [29] M. E. McCormick, *Ocean Wave Energy Conversion*. New york: Wiley, 1981.
- [30] P. Boccotti, P. Filianoti, V. Fiamma, and F. Arena, “Caisson breakwaters embodying an OWC with a small opening-Part II: A small-scale field experiment,” *Ocean Eng.*, vol. 34, no. 5–6, pp. 820–841, 2007.
- [31] F. Arena, A. Romolo, G. Malara, and A. Ascanelli, “On Design and Building of a U-OWC Wave Energy Converter in the Mediterranean Sea: A Case Study,” in *ASME 2013 32nd International Conference on Ocean, Offshore and Arctic Engineering*, 2013, p. V008T09A102.
- [32] S. P. R. Czitrom, R. Godoy, E. Prado, P. Pérez, and R. Peralta-Fabi, “Hydrodynamics of an oscillating water column seawater pump,” *Ocean Eng.*, vol. 27, no. 11, pp. 1181–1198, Nov. 2000.
- [33] M. E. McCormick, *Ocean engineering wave mechanics*. 1973.
- [34] “SDK Wave Turbine,” in *Infrastructure Access Report - MARINET*, 2013.
- [35] D. Carter, “Estimation of wave spectra from wave height and period,” 1982.